The Surface of Mars: Morphology and Process

by

Oded Aharonson

Submitted to the Department of Earth, Atmospheric and Planetary Sciences
in partial fulfillment of the requirements for the degrees of

Doctor of Philosophy

and

Master of Science

at the

MASSACHUSETTS INSTITUTE OF TECHNOLOGY

June 2002

Author .....
Department of Earth, Atmospheric and Planetary Sciences
May 3, 2002

Certified by .....
Maria T. Zuber
Professor
Thesis Supervisor

Accepted by .....
Ronald G. Prinn
Head, Department of Earth, Atmospheric and Planetary Sciences

The Surface of Mars: Morphology and Process

by

Oded Aharonson

Submitted to the Department of Earth, Atmospheric and Planetary Sciences
on May 3, 2002, in partial fulfillment of the
requirements for the degrees of
Doctor of Philosophy
and
Master of Science

Abstract

The goal of this work is a quantitative description of the morphology of the surface of Mars, in order to constrain the nature of processes acting during the ancient past through today. Emphasis is placed on linking geometric properties to physical mechanisms. Surface smoothness on Mars is distinctive in the vast northern hemisphere plains. Amazonis Planitia is remarkable in its smoothness, exhibiting an rms variation in topography of < 2 m over a 100-km baseline, that is most comparable to planetary surfaces that are depositional in origin. The region of concentrated hematite mineralization in Sinus Meridiani is also relatively smooth, but neither region forms a closed basin. Mars' slope distribution is longer tailed than those of Earth and Venus, indicating a lower efficiency of planation processes relative to relief-building tectonics and volcanics. The shallower long-wavelength portion of the lowlands' topographic power spectrum relative to the highlands' can be accounted for by a simple model of sedimentation such as might be expected at an ocean's floor, but the addition of another process such as cratering is necessary to explain the spectral slope in short wavelengths. Large drainage systems on Mars have geomorphic characteristics that are inconsistent with prolonged erosion by surface runoff. We find the topography has not evolved to an expected equilibrium terrain form, even in areas where runoff incision has been previously interpreted. We demonstrate that features known as slope streaks form exclusively in regions of low thermal inertia, steep slopes, and incredibly, only where daily peak temperatures exceed 275 K during the martian year. The results suggest that at least small amounts of water may be currently present and undergo phase transitions. We detect subtle changes of the polar surface height during the course of seasonal cycles. Using altimetric crossover residuals, we show that while zonally averaged data captures the global behavior of CO_2 exchange, there is a strong dependence of the pattern on longitude. Decomposition of the signal into harmonics in time shows the amplitudes are correlated with the polar cap deposits.

Thesis Supervisor: Maria T. Zuber
Title: Professor

Acknowledgments

The work presented here is the culmination of several years of research I carried out at MIT. However, it could only exist due to the efforts a number of other people made along the way.

Most directly, I wish to thank my collaborators. Brad Hager, Jim Head, Samar Khatiwala, Greg Neumann, Dan Rothman, Norbert Schorghofer, Dave Smith, Kelin Whipple and Maria Zuber have all provided important ideas to the papers included here. Their contributions are reflected both in the substance and style of this work.

Moreover, any accomplishments were only possible thanks to invaluable support received from a few people. Steve Squyres introduced me to planetary science while I was at Cornell. He is responsible for igniting my passion for solar-system exploration. Jack Wisdom instilled academic principles in my work that I shall not forget. Dan Rothman's optimism and encouragement was valuable and unique because he demonstrated to me how these qualities can be attained without compromise of rigor. I thank Dave Smith for his ever cheerful leadership and confidence in me. The superior standards and degree of interaction with which MOLA team members operated are models to be imitated, and have allowed this investigation to flourish.

Maria Zuber, who respected me as a colleague from day one at MIT, steered my progress with impeccable advice. She opened the door to a community of leaders in the field, and invited me to earn a reputation. I thank her for presenting me with wonderful problems, and providing essential intellectual input for, and criticism of their solutions. Maria was, and I hope shall remain, my mentor, both in the scientific and broader sense. I aspire to some day guide others with the wisdom and care with which my advisors guided me.

My training would have been hopelessly deficient without the daily interactions with my many friends at MIT. But perhaps even more valuable, these friends and their families created an atmosphere in which progress was measured not only in print, but also in smiles.

Words could never describe the extent of support my parents Raphael and Drorith provided. Their often exaggerated view of my capabilities gave me with the audacity to attempt what I would otherwise only dream about. I must work twice as hard to be even half as good as they treat me. Through their strong will, my siblings Karin and Yony reminded me that the ocean becomes only as wide as we allow it to, and that our growth and maturing turn to aging only if we allow them to. I deeply thank my late father-in-law Richard, mother-in-law Linda, and their children Doug and Kim, for adopting me into their warm family years before I married Donna.

No person in the world could better share my joys of success and burdens of adversity than my wife Donna. For her loving words and impassioned opinions I am forever indebted, as they are the backbone of my daily existence.

Despite (or perhaps in response to) my best efforts to engage in absurd pursuits, the people I mentioned tirelessly supported my decisions. Over the years, their efforts meant that obstacles magically disappeared from my path. All that was left for me was to stay true to course, and try not to stumble.

To the memory of my grandfathers–
Jacob (Yony) Blattner (1922-1978) and Yehuda Aharonson (1920-2002),
who have made education a family love.

Contents

1 Introduction: Quantitative Surface Morphology **15**

2 Regional Slope Characteristics **23**

2.1 Introduction 24

2.2 Local and Regional Slopes 24

2.3 Regional Roughness 27

2.4 Stochastic Inversion 31

3 Global Statistics and Surface Roughness **35**

3.1 Introduction 36

3.2 Data Collection and Accuracy 36

3.3 Global Hypsometry 37

3.4 Long-Baseline Tilts 39

3.5 RMS and Median Slope 42

3.6 Interquartile Scale 46

3.7 Horizontal Decorrelation Length 48

3.8 Power Spectral Analysis 50

3.9 Landing Site Selection 55

3.10 Conclusions 55

3.11 Appendix A: Power Spectrum Evolution 57

3.12 Appendix B: Summary of stochastic parameters 59

4 Drainage basins and channel incision **63**

4.1 Introduction 64
4.2 Method 65
4.3 Terrestrial Analog 66
4.4 Stream Profiles on Mars 67
4.5 Basin Concavity 73
4.6 Summary 74
4.7 Appendix A: A Search for Lithologic Beds 76

5 Evidence for a Phase-Transition of Water on Mars **81**
5.1 Introduction 82
5.2 Geographic distribution 83
5.3 Formation Times 90
5.4 Water phase transitions 91
5.5 Summary 95

6 Time-Dependent Topography and Seasonal Cycles **97**
6.1 Introduction 98
6.2 Data Quality 100
6.3 Time-Dependent Topography 102
6.4 Comparison with Thermal Crocus Date 108
6.5 Comparison with Global Circulation Models 113
6.6 Summary 116

List of Figures

1-1 Mars surface topography 18

1-2 Vertical roughness and scale 21

2-1 Selected 10-km slopes across northern hemisphere 25

2-2 Topography and slopes across Olympus Mons 26

2-3 Topography and slopes across Valles Marineris 28

2-4 Amazonis Planitia surface roughness 30

2-5 Comparison of planetary surface topography 32

2-6 Populations of roughness parameters 34

3-1 Global hypsometry 38

3-2 Global slope histogram 40

3-3 Pole-to-pole topography 42

3-4 Long-baseline tilts 45

3-5 Median slope surface roughness 46

3-6 Sinus Meridiani 47

3-7 Interquartile scale 50

3-8 Decorrelation length 51

3-9 Power spectrum evolution 52

3-10 Noisy diffusion model 54

3-11 Landing site surface roughness 56

3-12 Qualitative evolution under noisy diffusion 60

4-1 Watershed calculation 66

4-2 Topography of Fifty Mile Creek, Utah 68
4-3 Topography of Bown's Canyon, Utah 69
4-4 Topography of Ma'adim Vallis, Mars 71
4-5 Topography of Al-Qahira Vallis, Mars 72
4-6 Slope-area relations 75
4-7 Al-Qahira channel beds 77
4-8 Valles Marineris channel beds 78

5-1 Slope streaks examples 83
5-2 Null sample and streak population 84
5-3 Thermal inertia 85
5-4 RMS slope map 86
5-5 Slope streaks topographic profiles 87
5-6 Cumulative histograms 88
5-7 Combined mask and maximum surface temperature 89
5-8 Azimuthal correlations 90
5-9 Temporal correlations 92
5-10 Water phase diagram 94

6-1 Crossover Residuals 102
6-2 Longitude averaged accumulation 104
6-3 North pole crossover residuals 106
6-4 South pole crossover residuals 107
6-5 North pole temporal harmonic fits 109
6-6 South pole temporal harmonic fits 110
6-7 Equatorial region temporal harmonic fits 111
6-8 GCM predictions of CO_2 variations 115
6-9 Atmospheric conditions from TES 117

List of Tables

2.1 Data sets used for planetary surface comparison 31

5.1 Sensitivity to parameter thresholds 86

Chapter 1

Introduction: Quantitative Surface Morphology

During recent years, the promise of quantitative description of planetary surfaces has began to bear fruit. Data of unprecedented richness have been collected by multiple spacecraft. Advances are attributable to a number factors, but chiefly to technological leaps in payload instrumentation and ground-based computing. Armed with these rapidly improving tools, we have left the surface of the Earth, and have begun a systematic exploration of the bodies of the solar system.

The goal of this work is a quantitative description of the morphology of the surface of Mars, in order to constrain the nature of processes that have acted from the ancient past through today. The data were collected by the Mars Global Surveyor [*Albee et al.*, 2001] (MGS) spacecraft, and most of the analysis will be of the topographic measurements obtained by the Mars Orbiter Laser Altimeter (MOLA) instrument [*Smith et al.*, 2001b; *Zuber et al.*, 1992]. MOLA measured the topography of Mars by firing infrared (1064 nm) laser pulses toward the surface at a rate of 10 Hz and measuring the round-trip time of flight. By reconstructing the position of the MGS spacecraft with respect to Mars' center of mass using the X-band transponder from the MGS Radio Science experiment [*Tyler et al.*, 2001, 1992], it is possible to obtain measurements of planetary radii. In order to study

slope-dependent processes it is desirable to determine surface elevations with respect to the gravitational potential. Data were thus converted to geopotential topography [*Smith et al.*, 1999b] by subtracting the areoid from each radius measurement.

Mars Global Surveyor was a reflight of most of the instrumentation included initially on the ill-fated Mars Observer spacecraft, that was lost three days before its arrival at Mars in August, 1993. MGS successfully inserted into orbit about Mars on September 11, 1997. The spacecraft used a more reliable but less capable launch vehicle than Mars Observer, which did not permit the spacecraft to inject directly into the desired 400-km, near-circular, near-polar mapping orbit. The MGS capture orbit was elliptical with a northern hemisphere periapsis and a period of 45 hours. A period of aerobraking was planned to reduce the MGS orbit apoapsis to attain the mapping orbit.

MOLA collected its first pass over the northern hemisphere of Mars during an instrument check out period shortly after orbit insertion. MGS then entered its aerobraking period, when no data collection was possible because the instruments were out of view of the surface during periapsis drag passes. Damage to a solar panel damper arm during its initial deployment caused a hiatus in aerobraking to allow development of plans for aerobraking at lower dynamic pressures. During the hiatus, between October 14 and November 6, 1997, MOLA collected 17 topographic profiles across the northern hemisphere at spacecraft altitudes less than the maximum instrument range of 687 km. These observations are the focus of Chapter 2. The instrument collected an additional 188 northern hemisphere profiles during the science phasing orbits from March to September 1998, during which time aerobraking was halted to enable the spacecraft to achieve the desired 2:00 PM equator-crossing time for the mapping orbit. MOLA began continuous mapping of Mars in the MGS circular mapping orbit on February 28, 1999, and continued collecting range observations through the end of June, 2001. During this time the instrument collected over 671,000,000 measurements of the elevation of the surface and of atmospheric reflections on Mars.

MOLA is mounted on the MGS nadir deck and ranged to Mars at approximately vertical

incidence. In the global mapping orbit, MOLA observations consisted of ~160 m diameter footprints spaced ~300 m apart along the spacecraft ground track. The instrument has a ranging precision of 37.5 cm and individual measurements have an absolute radial accuracy (determined by spacecraft orbit reconstruction) of ~1 m [*Neumann et al.*, 2001; *Smith et al.*, 2001b]. The global topographic grid has a spatial resolution of ~1 km.

The MOLA gridded map of elevation is shown in Figure 1-1 [*Smith et al.*, 1999b], labeled with the names of prominent features on the surface. The most striking feature of the global topography field is the hemispheric dichotomy between the smooth, young, northern lowlands, and the rough, ancient, southern highlands. The elevation difference between the northern and southern hemispheres is ~5 km. A definitive explanation of both the elevation and morphological differences in terms of an evolutionary history remains a primary challenge and source of debate for Mars researchers [e.g. *McGill and Dimitriou*, 1990; *Wilhelms and Squyres*, 1984].

The prominent rise centered on the equator between longitudes 220°E-300°E is the Tharsis province, consisting of large volcanos and extensive flood volcanism. A gigantic tectonic rift named Valles Marineris extends eastward from highest point of Tharsis, and terminates in Chryse Planitia, a vast fluvial drainage basin. Impact craters are most abundant in the southern hemisphere; the largest impact basin is Hellas, centered at 45°S 65°E. An older basement surface appears to underlie the younger northern plains, as recorded in the crust by subdued crater topography in the Utopia basin, as well as smaller "stealth craters" that are indistinct in photographs [*Frey et al.*, 2000; *Zuber*, 2001].

Elevated polar ice caps represent large volatile reservoirs, exchanging with the Martian atmosphere and regulating the climate. Active dune field deposits (e.g. Olympia Planitia, 78°N 180°E) add complexity of the surface and its interaction with the atmosphere.

A rich set of known and unknown processes are responsible for these and many other surface features on Mars. While photo-geology has traditionally been the tool of choice in characterizing and interpreting surface morphology on the planet, the prospect of using high-resolution and high-accuracy topographic data for more quantitative investigations

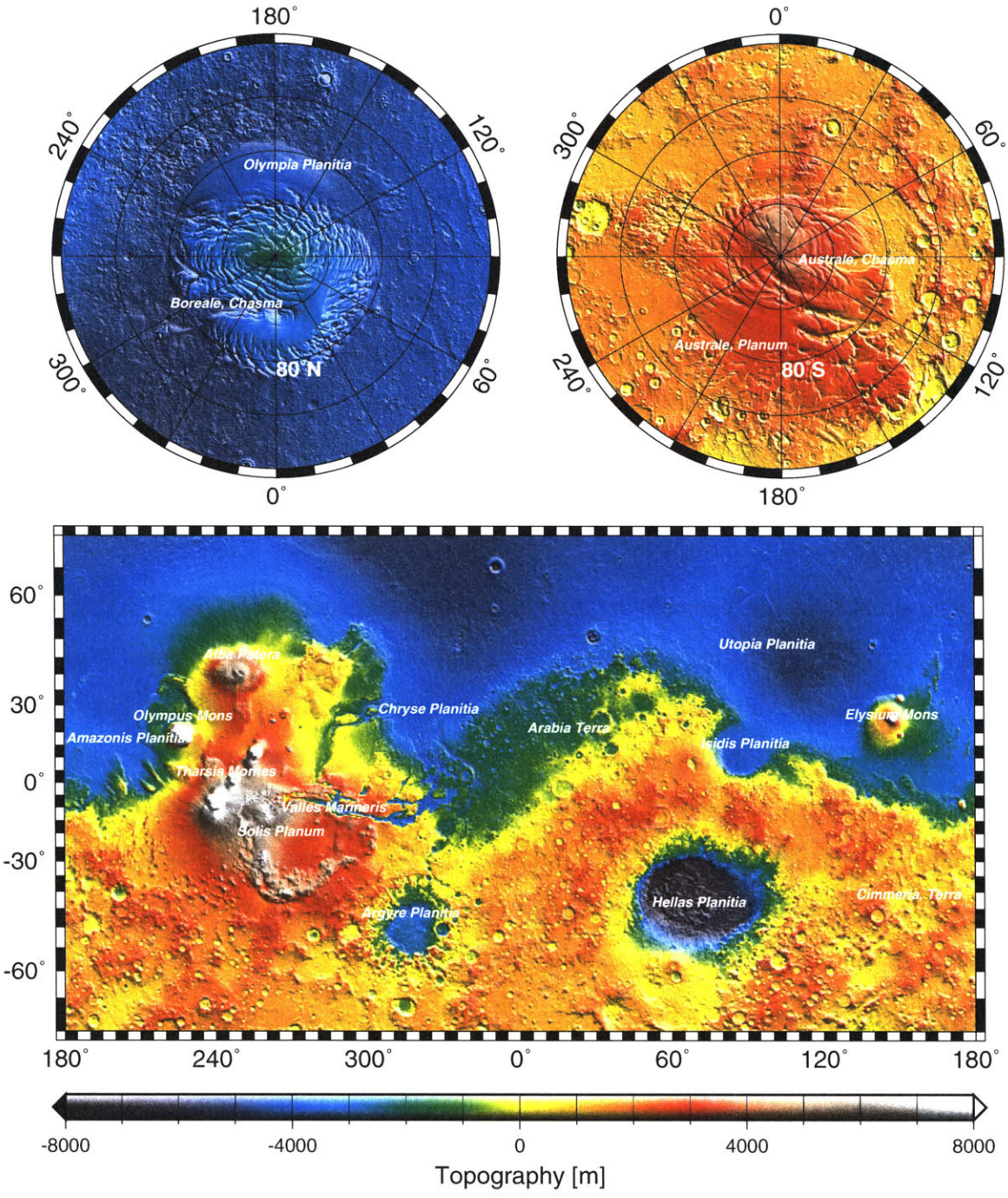

Figure 1-1: Mars surface topography

motivates this work. Hampered, but not dissuaded, by the difficulty of *in situ* field study on Mars, we develop and apply techniques that probe the surface properties on the global scale in new ways, with the goal of providing findings that constrain past and present processes that have shaped the surface. In the course of our analysis we propose ideas that can be tested with future observations.

The results are organized in six chapters. This chapter offers an introduction and motivation to the problem. Chapter 2 utilized initial observations from the Mars Global Surveyor capture and aerobraking iiatus orbits [*Albee et al.*, 2001] that provided the first accurate high resolution topographic observations of the northern hemisphere of Mars. This study focuses on regional and local observations of surface structure, including a comparative analysis of Amazonis Planitia, the smoothest large-scale surface yet measured in the solar system, as well as the first precise measurements of slopes in areas of past mass wasting events. Chapter 3 offers the first global perspective of the roughness and scale-dependent topographic properties of Mars, defining and computing relevant parameters. The characterization includes length scales ranging from the MOLA footprint spacing (10^2 m) to hemispheric surface units (10^3 km). The statistical nature of the global dichotomy and other correlations with local geologic units are described, and the effect of smoothing of the surface by sedimentation in a hypothetical northern-lowlands ocean is considered, and tested against the observed power spectral shape. Chapter 4 is devoted to the morphological characteristics associated with fluvial erosion of channels and drainage basins. This work addresses a basic question in the history of Mars: the extent to which surface evolution was influenced by fluvial erosion. We find that drainage systems that have previously been interpreted as sculpted by runoff erosion appear largely unevolved in a fluvial sense, which eases strict requirements of a persistent warm and wet early climate on the planet. In chapter 5, exciting correlations between the physical properties of the surface and features known as slope-streaks are used to argue that a water phase-transition may be responsible for triggering their formation. This work has implications for the distribution and stability of liquid water on present-day Mars. Finally, in chapter 6, temporal changes in the mean

surface height are extracted from the MOLA topographic data set, and used to constrain the cycle of CO_2 during the Martian year. The exchange of carbon dioxide with the atmosphere is characterized both in space and in time, and compared with a general circulation model simulation of the seasonal cycle of CO_2 on Mars. We show that while most characteristics of the pattern of condensed CO_2 are consistent with the paradigm of an insolation-driven global seasonal cycle, there are also some aspects of the observed deposition and sublimation that must result from more complex atmospheric dynamics. These observations will provide constraints for future modeling of both global-scale and meso-scale dynamics of the Martian atmosphere.

While global-scale characterization of the topography of Mars is of significant importance in quantifying the processes that have shaped the surface, there is also an operational impetus to understand the nature of Mars topography, namely targeting of future landed spacecraft. In this regard, orbitally-derived surface characteristics are especially useful when evaluated in the context of synergetic data types. For example, rare ground-truth on Mars is available from the Pathfinder lander. The payload cameras provided a three dimensional view of the landing site reconstructed in great detail down to centimeter resolution [*Kirk et al.*, 1999; *Smith et al.*, 1997]. Orbital images can be used for morphometric analysis down to $\sim$10 m. In order to compare these observations, we consider the vertical roughness in the RMS sense, defined by the 1-dimensional structure function ν of baseline l,

$$\nu(l) = \left\langle |h(x+l) - h(x)|^2 \right\rangle_x^{1/2} . \tag{1.1}$$

If ν is approximated with a power-law, then the exponent is often referred to as the Hurst exponent. In Figure 1-2 vertical roughness measurements as a function of length-scale from MOLA data [*Aharonson et al.*, 2001, and Chapter 3] are compared with those computed from stereo topography derived from Viking orbiter images, Mars Orbiter Camera (MOC) images [*Kirk et al.*, 2001], and from the Images for Mars Pathfinder (IMP) [*Kirk et al.*, 1999] (The stereo analyses were obtained from R. Kirk, *personal communication,* 2001). The gray box plotted indicates in the vertical direction the range of slopes derived from

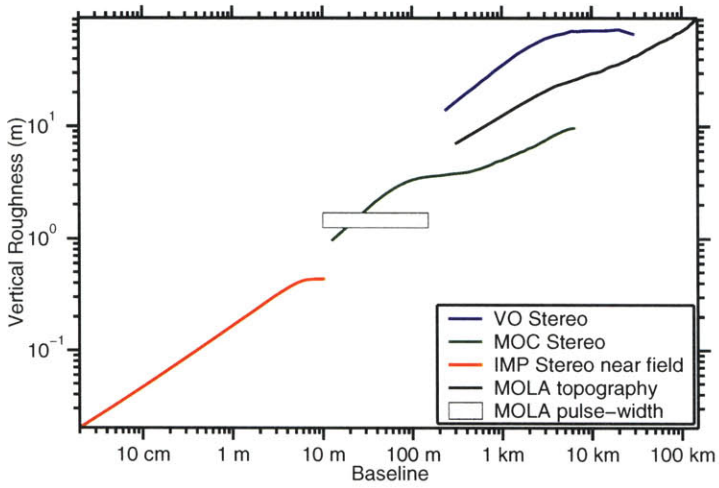

Figure 1-2: Vertical roughness computed from a variety of data. Shown are measurements derived from MOLA elevations (black curve), Viking orbiter images (blue), MOC (green), and IMP near-field (red). Gray box indicates MOLA pulse-width and range of likely contributing scales.

MOLA pulse width measurements [*Garvin et al.*, 1999], and in the horizontal direction the range of baselines that are likely to contribute to the pulse spread. Slopes computed from MOLA elevations lie between the Viking and MOC estimates, and are consistent with an extrapolation of the IMP high resolution estimates. The pulse width roughness measurements are seen to be in agreement with the MOLA, MOC and IMP roughness trend, all extrapolated to approximately 20-m baseline. This result, if it can be generalized, will provide a valuable quantitative calibration to existing global pulse width measurements, enhancing their interpretation and utility for future landing site characterization.

Chapter 2

Regional Slope Characteristics

Originally published in:
Aharonson, O., M. T. Zuber, G. A. Neumann, D. E. Smith, and J. W. Head, Mars: Northern hemisphere slopes and slope distributions, *Geophys. Res. Lett.*, *25*, 4413–4416, 1998

Abstract

We investigate slope distributions in the northern hemisphere of Mars from topographic profiles collected by the Mars Orbiter Laser Altimeter. Analysis of the region from about 12°S to 82°N, over diverse geologic units, indicates that the range of regional-scale slopes is small, generally $< 3°$. Surface smoothness is most distinctive in the vast northern hemisphere plains, where slopes are typically $< 1°$. Amazonis Planitia is particularly remarkable in its smoothness, exhibiting an rms variation in topography of < 2 m over a 100-km baseline. This relative smoothness is still present when compared with other sampled areas of the Martian northern hemisphere and with volcanically resurfaced terrains elsewhere in the solar system. Surfaces of large areal extent that are most comparable to Amazonis in terms of rms elevation variation over hundred km spatial areas are depositional in origin and include terrestrial oceanic abyssal plains and certain sedimentary basins. Tectonic, impact and volcanic processes all create more significant relief, in some areas exceeding the angle of repose. Slopes across the Valles Marineris canyon system show that the upper portion of the walls are significantly and consistently steeper than the lower walls, characteristic of extensive mass wasting. The observed long-runout avalanche style is consistent with a high-energy collapsed flow. In the neighboring Noctis Labyrinthus canyons the duality between the upper and lower walls is reduced, and indicates a lower energy modificational history and/or greater cohesion of wall rock.

2.1 Introduction

Slopes and their statistical distribution are useful descriptors of planetary surfaces in that they can be pertinent to the mechanisms of formation of physiographic features, and are indicative of the style and duration of subsequent modificational processes. As a step towards quantifying the nature of surface processes of Mars, we analyze slope distributions derived from topographic profiles of the northern hemisphere from the Mars Orbiter Laser Altimeter (MOLA) [*Zuber et al.*, 1992], an instrument on the Mars Global Surveyor (MGS) spacecraft. The data were collected during orbital periapses 3 and 20 through 36 during the MGS capture orbit and aerobraking hiatus periods during September-November, 1997 [*Albee et al.*, 1998]. During that time the MOLA instrument collected 18 near-polar inclination (92°) passes in the approximate latitude range 82° N and 12° S. The data have a 300-400-m resolution along track, a 1200-km separation across track, a range resolution of 37.5 cm, a range precision of 1-10 m for surface slopes of up to 30°, and an absolute accuracy of 30 m with respect to Mars' center of mass [*Smith et al.*, 1998a]. These data currently constitute the highest quality measurements of Mars topography and permit quantification of slopes from local to hemispheric scale.

In this analysis surface slopes from MOLA observations were obtained over a ~ 600 m baseline from a 3-point Lagrange slope formula applied along track, and on longer baselines (> 10 km) from fitting a line to a set of points along a track.

2.2 Local and Regional Slopes

Figure 2-1 shows mean slopes on a 10-km baseline calculated by line fitting for selected passes. A number of deductions can be made upon closer examination of slopes over various baselines.

Subtle though notable long wavelength slopes are displayed in association with the massive volcano-tectonic Tharsis rise. Tharsis-related volcanic units rise gently (Figure 1, pass 24) for 2500 km at $0.08°$, with a root mean square (rms) deviation from a flat sloping

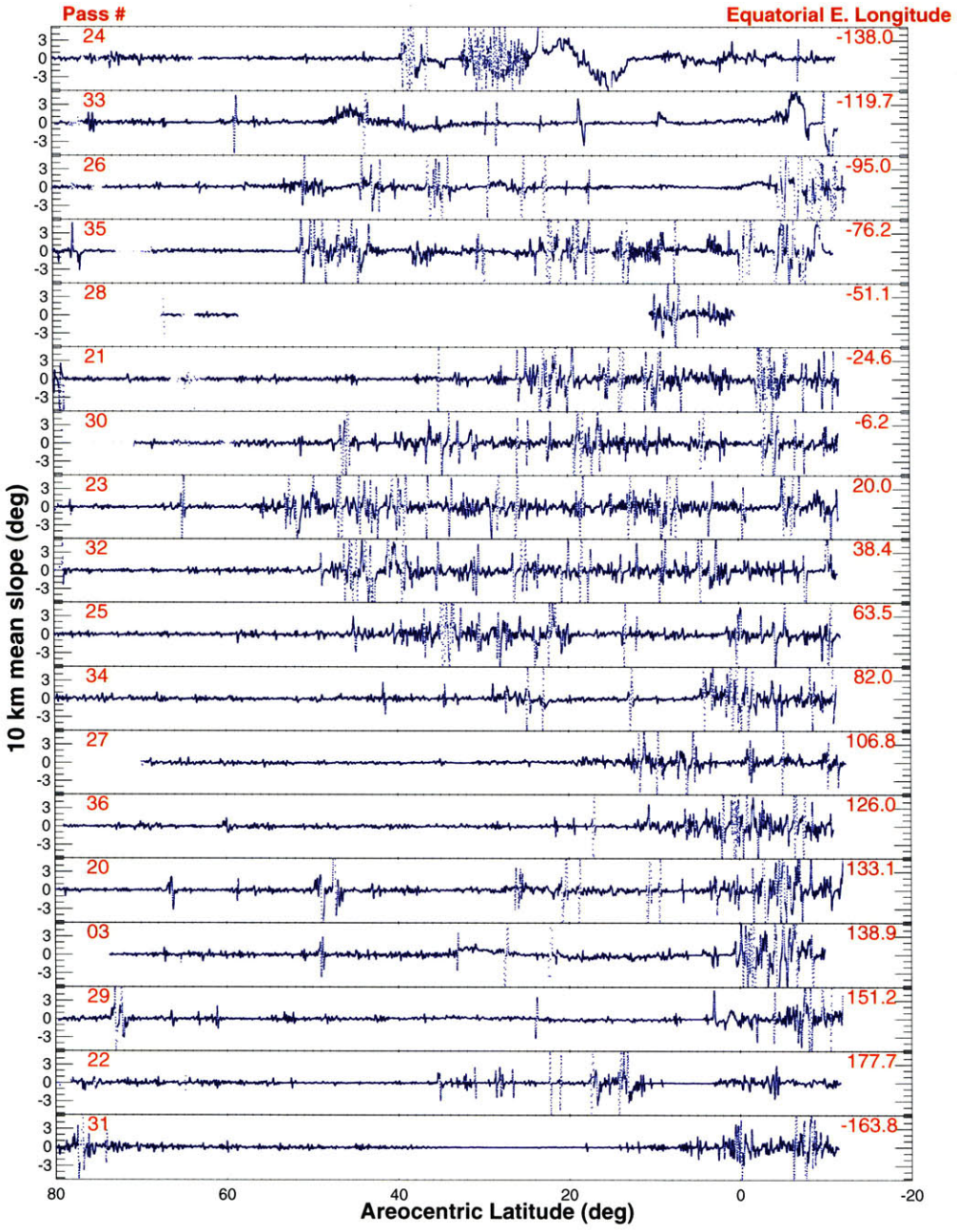

Figure 2-1: 10-km mean slopes across Mars' northern hemisphere

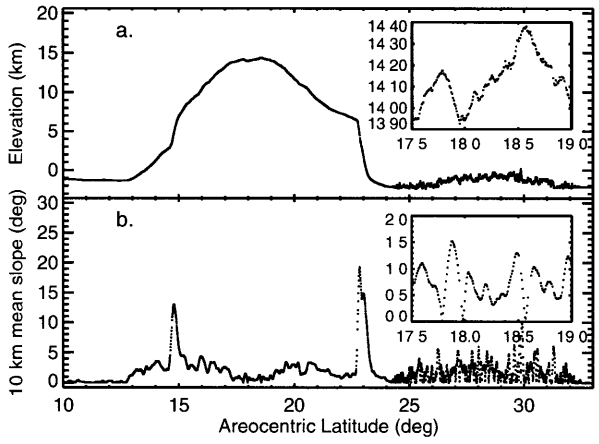

Figure 2-2: Topography (a) and slopes (b) across the Olympus Mons shield (Pass 24; longitude $-138°$ E). A portion of the profile running west of the volcano's summit is shown in the insert.

surface of only 61 m. Olympus Mons, the largest known volcano in the solar system, displays comparable flank slopes ($\sim 2.5 - 5°$) to Hawaiian shields (Figure 2-2). Abrupt changes in slope are apparent in the marginal scarp of Olympus Mons, at the headwalls of the aureole deposits, where the slope is $\sim 19°$, but can approach $30°$ if calculated over the shortest baselines observed.

The hemispheric dichotomy boundary region, which separates the low, volcanically resurfaced northern hemisphere from the older, heavily cratered and topographically higher southern hemisphere [*Carr and Clow*, 1981] rises upwards toward the south from about -4 km to 2 km over $\sim$ 400 km distance, giving less than a $1°$ mean slope. However, in some passes in the eastern hemisphere of Mars, the boundary is observed to have slopes on short baselines exceeding $20°$ [see also *Frey et al.*, 1998] Topographic roughness along the boundary on 10-km baselines is comparable to that in the southern highlands, though slopes along the boundary region have been influenced significantly by tectonic and erosional processes in addition to impact, which dominates in the south.

A set of features that display complexly varying local slopes are the canyon systems. Figure 2-3 shows the topography and associated slopes across the largest of these systems,

Valles Marineris (VM). Here local (600-m) slopes range from essentially flat over the valley floors, to typically less than 5° at the lower canyon walls, to 28° at the upper walls. Such a distribution indicates extensive mass wasting related to the slumping and erosion of material from the upper walls, which leaves behind a scarp that can expose bedrock. When slopes are observed as function of height above the valley floor, the lower 20% of the wall never exceeds $\sim$ 18° while the upper 30% of the wall almost never drops below $\sim$ 20°. Downslope material transport can occur by rotational listric faulting, mass wasting of individual fragments, talus formation, and landslides. The distance over which transported material is distributed across the valley floor is indicative of the energy of the transport process and the competence of canyon wall material. Across VM talus slopes extend to tens of km across the valley floor [*Lucchitta et al.*, 1992], which implies high energy and/or low effective friction of the mass movement [*McEwen*, 1989]. In contrast, the correlation between elevation and slope angle is much weaker in Noctis Labyrinthus, which marks the summit region of the Tharsis rise and forms the western-most component of the VM canyon system. Figure 2-3 shows that the Noctis chasmata are steeper on the lower extent of the canyon walls and have apparently undergone less mass wasting than in central VM. A chasm on Elysium rise (lat= 22.25° N; lon= 141.5° E) [*Smith et al.*, 1998b] shows a correlation between slope and wall elevation that is distinctive from but more comparable to the Noctis chasmata than to central VM chasmata. These observations provide an initial indication of the variability of erosional intensity or near surface cohesion that can be quantified with future observations.

2.3 Regional Roughness

The topographic distribution function is typically long-tailed due to cratering, faulting, and other localized processes. We therefore quantify the regional roughness using the interquartile scale (IQS) variation of topography in a window of width 100-km along track. In this characterization we measure the width of a histogram of only the most significant 50% of

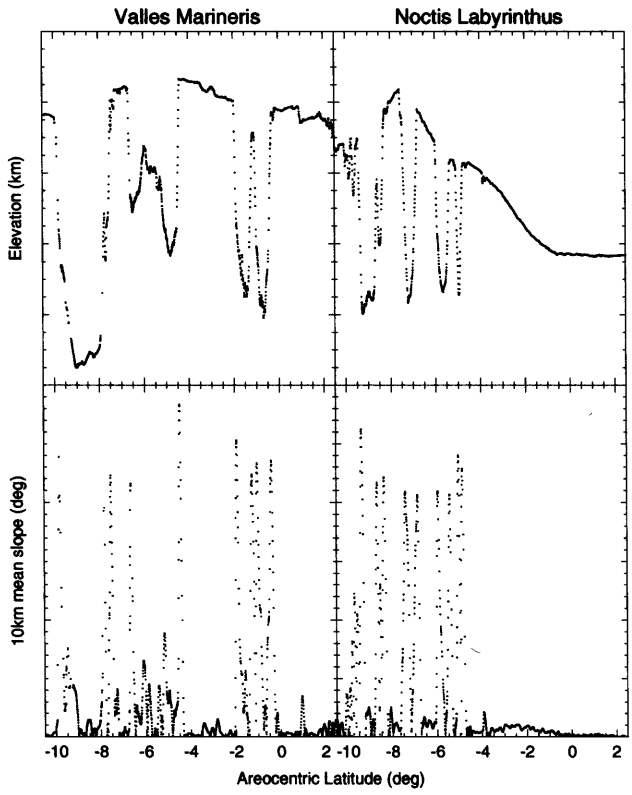

Figure 2-3: Topography and slopes across central Valles Marineris (Pass 35; longitude $-77°$ E) and Noctis Labyrinthus (Pass 26; longitude $-95°$ E).

the elevations, scaled to unity in the case of a normal distribution. Before normalization, this estimator R_q is defined [*Neumann and Forsyth*, 1995] as

$$R_q = \frac{N}{2N-1}(Q_3 - Q_1) \tag{2.1}$$

where Q_i is the elevation of the i^{th} quartile point and N is the number of points. To normalize, R_q is divided by 0.673, the IQS of a normal distribution. The parameter R_q is a robust estimator in the sense that it is not sensitive to outliers in as much as half of the population (or as little as a quarter). We apply this calculation to all range returns that fall within a 100-km window sliding along the points on each profile. Hence the number of points included in the window varies. It is possible to detrend the points in a given window

to remove the regional slope before calculating the IQS, but doing so proved to change none of the following characteristics that emerge distinctly from the analysis.

The northern hemisphere is surprisingly flat with typical inter-quartile scale of a few tens of meters, ranging over thousands of kilometers [*Zuber et al.*, 1998b]. The Olympus Mons aureole deposits are the roughest surfaces observed, with IQS exceeding 2 km. The most unusual region is Amazonis Planitia, an area to the northwest of Olympus Mons of Amazonian age and elevation of approximately -4.1 km relative to the average equatorial geoid. This surface displays an rms variation in topography of only a few meters (still above the instrument's range resolution), extending over hundreds of kilometers, and correlating well with previously mapped geology (Figure 2-4). The smoothest part of the surface corresponds to member 3 of the Arcadia Formation, which is interpreted to consist largely of lava flows and small volcanoes [*Scott and Tanaka*, 1986]). Member 3 also forms smooth plains west of the Olympus Mons aureoles and displays occasional flow fronts at Viking resolution. This area has an anomalously low thermal inertia (between 2 and 3 $\times 10^{-3}$ cal cm^{-2} $s^{-1/2}$ K^{-1} [*Christensen and Moore*, 1992]) with very low variability over tens of km scale, anomalously low radar backscatter cross-section at a variety of wavelengths [*Jakosky and Muhlemann*, 1981], and has been interpreted to be accumulations of fine-grained dust [*Christensen*, 1986]. The regional flatness and low surface roughness detected by MOLA is consistent with this interpretation but does not uniquely explain the genesis of this region.

An initial step towards identifying the mechanism of formation of Amazonis Planitia is to compare its topographic properties to other smooth regions with potentially analogous origins. Shown in Figure 2-5 are profiles of elevation collected by various altimeters over smooth surfaces from a variety of solar system bodies, summarized in Table 2.1. At the top is MOLA Pass 31 over Amazonis Planitia, where the anomalously smooth region is observed to extend over 600 km, approximately centered in the plot (vertical point-to-point accuracy $\delta z \sim 0.4$ m, horizontal resolution $\delta x \sim 0.3$ km). Below is a Clementine profile of the Moon's Oceanus Procellarum ($\delta z \sim 40$ m, $\delta x \sim 2$ km for 1 Hz data and ~ 0.2 km for 8 Hz data) [*Smith et al.*, 1997], Magellan radar altimetry over Niobe Planitia ($\delta z \sim 4$

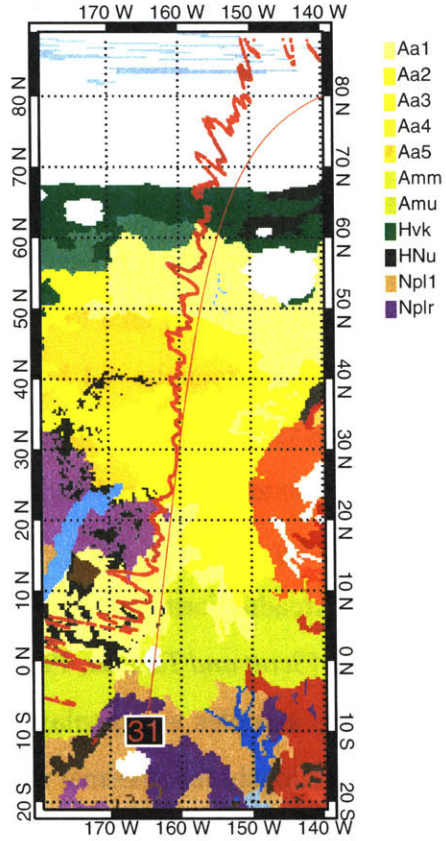

Figure 2-4: Logarithm of Inter-quartile scale of topography indicative of surface roughness on MOLA Pass 31 shown over the USGS geologic map. The geologic unit AA3 corresponds to the smooth plains of Amazonis and is strongly correlated with very low roughness areas.

m, $\delta x \sim 10$ km) [*Ford and Pettengill*, 1992], Shuttle Laser Altimeter data collected over the Sahara desert ($\delta z \sim 1.5$ m, $\delta x \sim 0.7$ km) [*Garvin et al.*, 1997], and shiptracks of Seabeam 2200 bathymetry over the south Atlantic abyssal plains ($\delta z \sim 2$ m, $\delta x \sim 0.1$ km) [*Neumann et al.*, 1996]. The last two profiles were extracted from the GTOPO data set (highly variable $\delta z \sim 20$ m, $\delta x \sim 0.1$ km) [*Gesch and Larson*, 1996], first over the Great Plains in the U.S., and second over the Indo-Gangedic Plains across over the Tibetan Plateau, down across the Tarim Basin and continuing northwards. Oceanus Procellarum consists of lava flows that have been broadly tilted by subsidence and locally steepened by tectonic deformation (wrinkle ridges); their small-scale roughness is dominated by impact

Planet	Region	Source	δx (km)	δz (m)	Data Reference
Mars	Amazonis Planitia	MOLA	0.3	0.4	*Smith et al.* [2001b]
Moon	Oceanus Procellarum	Clementine	0.2[a]	40	*Smith et al.* [1997]
Venus	Niobe Planitia	Magellan	10.0	4	*Ford and Pettengill* [1992]
Earth	Sahara desert	SLA	0.7	1.5	*Garvin et al.* [1997]
Earth	South Atlantic	Seabeam 2200	0.1	2	*Neumann et al.* [1996]
Earth	Great Plains, US	GTOPO DEM	0.1	20[b]	*Gesch and Larson* [1996]
Earth	Tibetan Plateau and basins	GTOPO DEM	0.1	20[b]	*Gesch and Larson* [1996]

[a]Resolution is ~1.6 km for 1-Hz data and ~0.2 km for 8-Hz data.
[b]Highly variable

Table 2.1: Summary of data sets used in the planetary surface comparison of Figure 2-5 and their approximate horizontal resolution δx and vertical accuracy δz.

regolith formation processes. Niobe Planitia on Venus consists of vast lava plains similarly tilted and steepened but not influenced by regolith formation. Comparison of these surfaces reveals that of these lowest, smoothest regions observed in the solar system, Amazonis Planitia closely resembles in its smoothness only the heavily sedimented surfaces on the Earth, *i.e.* oceanic abyssal plains and basins filled by fluvial deposition processes. It is noteworthy that volcanically resurfaced terrain is markedly rougher on the Moon, on Venus, and on Mars, than the peculiar Amazonis deposits. Saharan sand sheets are rougher by a factor of about three. Other regions in the Martian northern hemisphere that exhibit evidence of dust deposition are rougher than Amazonis as well.

2.4 Stochastic Inversion

Statistical analysis of the topography provides further quantification of macroscale roughness properties. The topographic profiles can be decomposed into three components [*Goff and Jordan*, 1988]: a "deterministic" component, *i.e.*, a regional slope, a quasi-stochastic component with power-law spectral behavior, and erratic components. The latter consists of outliers, representing, for example, small craters, false returns, and instrument noise, with no point-to-point correlation. The stochastic component has a fractal-like roughness,

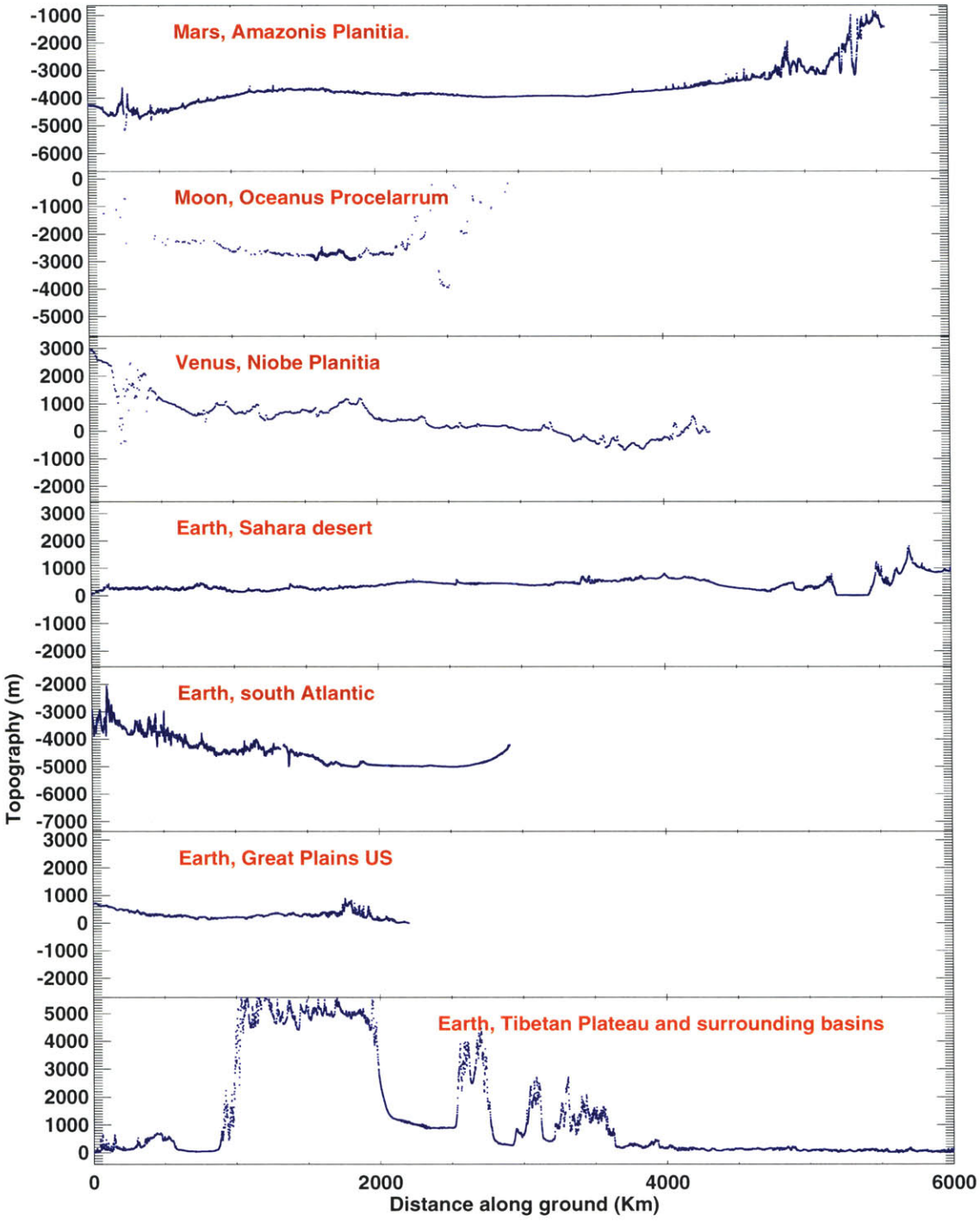

Figure 2-5: Comparison of planetary surface topography. See text for description.

characterized by a point-to-point correlation length scale l and an rms roughness h. Inversion schemes to determine these parameters [*Goff and Jordan*, 1988; *Neumann and Forsyth*, 1995] require estimation of either the autocorrelation function or the local slope distribution, as well as instrument parameters. The model adopted here from *Neumann and Forsyth* [1995] has a fractal dimension 2.5 and an associated covariance function for a spatial lag u at position x:

$$c(x, x+u) = h^2 e^{-r} + S_n^2 \delta(r) \tag{2.2}$$

where S_n is the rms noise and

$$r = \sqrt{2}\frac{u}{l}. \tag{2.3}$$

We have performed an inversion that resolves distinct populations in $h - l$ space (Figure 2-6). The model that best fits the MOLA stochastic component includes about 50 cm of rms noise due to instrument and pulsewidth jitter. The model roughness h, on a 60 km (1°) baseline, varies from a minimum of 1.5 m over the Amazonis basin and a region to the southeast, to nearly 10 km in the Olympus Mons area. In the estimation procedure the correlation scale is initially assumed to be 10 km. The resulting estimates vary from about 2 km to several hundred km. Taken together, these scales resolve 3 arrays of surface type: 1) plains with about 25-m rms roughness and 8-km correlation scale length; 2) highlands with $>$ 50-m roughness and $>$ 10-km scale; and 3) a low, smooth region with about 2-m roughness, and with a 20-km scale.

The statistical properties of the smoothest surface type resemble most closely certain terrestrial depositional environments including oceanic abyssal plains and sedimentary basins. Given previously hypothesized scenarios for Mars' geological past [*Carr and Clow*, 1981], the evidence so far may be consistent with an origin for Amazonis in which extensive aeolian deposition follows a volcanic resurfacing event. Also possible is a modificational history in which water provides a sedimentary environment capable of smoothing meter scale topography.

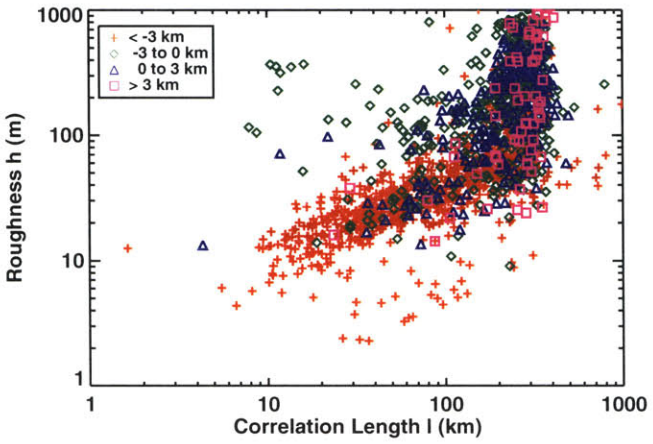

Figure 2-6: Inversion in $h - l$ space. Evident is a positive correlation between elevation and roughness.

Acknowledgments

We acknowledge helpful discussions with Kelin Whipple and Tom Jordan. This study was supported by the Mars Global Surveyor Project.

Chapter 3

Global Statistics and Surface Roughness

Originally published in:
Aharonson, O., M. T. Zuber, and D. H. Rothman, Statistics of Mars' topography from MOLA: Slopes, correlations and physical models, *J. Geophys. Res.*, *106*, 23,723–23,735, 2001

Abstract

Data obtained recently by the Mars Orbiter Laser Altimeter (MOLA) were used to study the statistical properties of the topography and slopes on Mars. We find that the hemispheric dichotomy, manifested as an elevation difference, can be described by long baseline tilts but in places is expressed as steeper slopes. The bimodal hypsometry of elevations on Mars becomes unimodal when referenced to the center of figure, contrary to the Earth, for which the bimodality is retained. However, ruling out a model in which the elevation difference is expressed in a narrow equatorial topographic step cannot be done by the hypsometry alone. Mars' slope distribution is longer tailed than those of Earth and Venus, indicating a lower efficiency of planation processes relative to relief-building tectonics and volcanics. We define and compute global maps of statistical estimators, including the interquartile scale, RMS and median slope, and characteristic decorrelation length of the surface. A correspondence between these parameters and geologic units on Mars is inferred. Surface smoothness is distinctive in the vast northern hemisphere plains, where slopes are typically $<0.5°$. The region of probable hematite mineralization in Sinus Meridiani is smooth, with median slopes lower than $0.4°$, but does not form a closed basin. The shallower long-wavelength portion of the lowlands' topographic power spectrum relative to the highlands' can be accounted for by a simple model of sedimentation such as might be expected at an ocean's floor. The addition of another process such as cratering is necessary to explain the spectral slope in short wavelengths. Among their application, these MOLA-derived roughness measurements can help characterize sites for landing missions.

3.1 Introduction

As descriptors of planetary surfaces, slopes and slope distributions are pertinent to the mechanisms of formation of physiographic features and are indicative of the style and duration of subsequent modificational processes [e.g., *Scheiddeger*, 1991]. As a step toward quantifying the nature of surface processes of Mars, we analyze elevation and slope statistics derived from profiles collected by the Mars Orbiter Laser Altimeter (MOLA) [*Zuber et al.*, 1992], an instrument on the Mars Global Surveyor (MGS) spacecraft. Since the origin of some large- and small-scale surface features remains in debate, the task of interpreting statistical models for geophysical information is ambiguous. Nonetheless, such statistical estimation can be useful, especially in a comparative sense and when additional observation types are included in the interpretation. For example, the topography of the Earth's seafloor has been characterized in detail by several studies [*Fox and Hayes*, 1985; *Goff and Jordan*, 1988; *Neumann and Forsyth*, 1995; *Smith and Jordan*, 1988] in terms of models describing its statistical properties and power spectrum, and several processes have been modeled with these tools, including seafloor spreading, sedimentation, and seamount distribution. The statistics of continental topography has been studied in landscapes such as eroding environments and river networks [e.g., *Rodríguez-Iturbe and Rinaldo*, 1997; *Scheiddeger*, 1991]. The stereographically derived topographic field of Mars that predated MGS [*Esposito et al.*, 1992; *Wu*, 1991] permitted only coarse study owing to its low precision and resolution. With the newly obtained information, an accurate statistical characterization is finally possible. Results based on initial data collected in the northern hemisphere were reported on by *Aharonson et al.* [1998] and more globally by *Aharonson et al.* [1999], *Kreslavsky and Head* [1999] and *Kreslavsky and Head* [2000].

3.2 Data Collection and Accuracy

The data set on which the following analysis is based was collected during the aerobreaking hiatus, science-phasing, and ongoing mapping orbits of Mars Global Surveyor [*Albee et al.*,

1998, 2001]. The data provide coverage of the surface of Mars at 300- to 400-m spacing along track as dictated from the spacecraft orbital velocity and the laser pulse repetition frequency of 10 Hz. The MOLA instrument has a range resolution of 37.5 cm, a range precision of 1-10 m for surface slopes of up to 30°, and an absolute accuracy of $\sim$1 m with respect to Mars' center of mass [*Neumann et al.*, 2001; *Zuber et al.*, 1992]. These data currently constitute the highest-quality measurements of Mars topography and permit quantification of slopes from local to hemispheric scale [*Smith et al.*, 1999b, 2001b]. The accuracy of point-to-point slopes along track is $<0.1°$. Resolving steep slopes is limited by the instrument's detection of reflected power, but this is rarely encountered, and only at slopes $> 45°$. In the following sections, various statistical estimators will be defined and applied to the data set. A global view of elevations and slopes is presented first, followed by regional slope and power spectral characteristics.

3.3 Global Hypsometry

The most striking global feature of the surface of Mars is the crustal dichotomy. The northern hemisphere is topographically lower, morphologically smoother, and geologically younger than the south [*Carr*, 1981; *Mutch et al.*, 1976]. A frequency diagram of elevations, or hypsogram (Figure 3-1a), shows this dichotomy clearly, as was previously observed [e.g., *Smith and Zuber*, 1996; *Smith et al.*, 1999b]. The strong bimodal distribution shows that the lowlands peak is $\sim$5.5 km lower than the highlands and is narrower, indicating the flatness of the north. The distribution's lowest portion, the peak between -7 km and -6 km, is the floor of the Hellas impact basin in the south. *Sharpton and Head* [1985] and *Sharpton and Head* [1986] compared the topography and slopes of Earth and Venus. Using the same bin widths, the hypsometry of Mars has a larger overall range of elevations than Earth (and Venus) and is bimodal, appearing similar to Earth, as shown in Figure 3-1c [*NGDC*, 1988]. However, as shown by *Smith et al.* [1999b] and by the solid black curves, by removing the spherical harmonic degree 1 terms, effectively referencing the topography

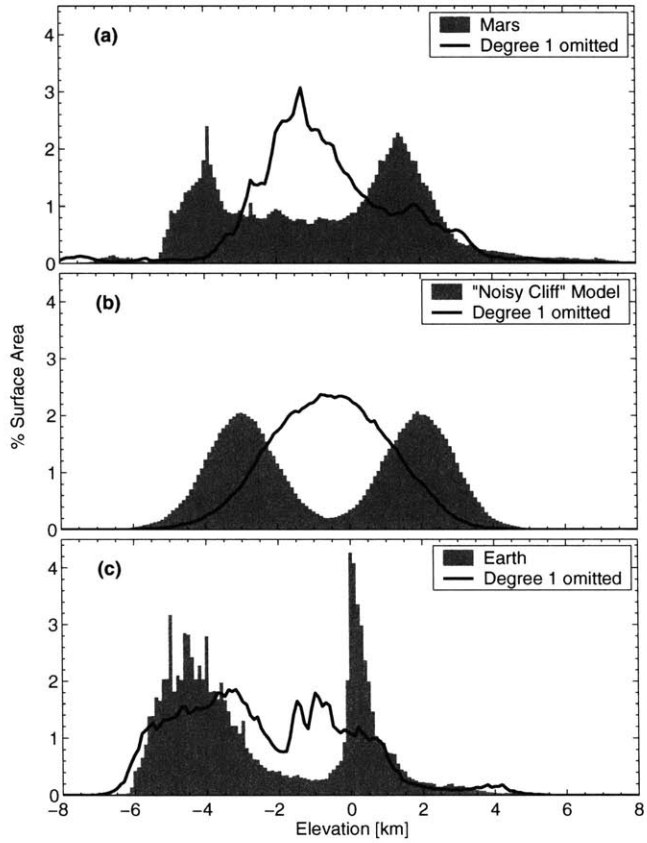

Figure 3-1: Hypsometry of surface topography from gridded elevation models. Bin width is 100 m. To compute an area weighted histogram, an equal-area projection of the data was used. The gray filled area is the elevation histogram with respect to the geoid, and the black curve is the distribution with the degree 1 terms removed. The distributions shown are for (a) Mars, (b) a synthetic "noisy cliff model," and (c) Earth.

to the geometric center of figure (COF) instead of the center of mass (COM), the distribution of topography of Mars becomes unimodal (as for Venus), whereas Earth maintains its bimodality.

It is instructive to consider a theoretical planet whose topography consists of an equatorial scarp of height 6 km with 1 km of normally distributed noise superimposed. Figure 3-1b shows the corresponding distributions of this "noisy cliff" model. Referencing to the COF also collapses the two sharp peaks of this model into one, but depending on the

amount of noise, shoulders can remain in the histogram. We therefore conclude that the elevation histogram of Mars is consistent with the dichotomy having a global effect, but an equatorial scarp is not ruled out by the hypsometry alone. Additional analysis is required to isolate contributions to the hemispheric elevation difference, for example, by crustal thickness variations, as done by *Zuber et al.* [2000].

It is also possible to compare regional slopes on Mars to results for Earth and Venus [*Sharpton and Head*, 1985]. Figure 3-2 shows an equal area histogram of 100-km slopes binned in 0.01° bins. Similar to Venus, the distribution for Mars peaks near 0.05° but is longer tailed. In fact, on Venus, regional slopes rarely exceed 0.3°. The steeper slopes on Mars are presumably related to the lower efficiency of planation processes (which on Earth are often driven by the hydrosphere and atmosphere). However, the expected value of the absolute slope varies greatly by region and will be discussed in later sections.

3.4 Long-Baseline Tilts

Several studies have demonstrated that Mars' topography is characterized by a hemispherical-scale tilt. For example, *Smith et al.* [1999b] and *Zuber et al.* [2000] observed that in a longitude band near the Mars prime meridian, the pole-to-pole topography can be described to first order by a pole-to-pole slope of ~0.036° downhill to the north. In addition *Phillips et al.* [2001], consider planetary-scale slopes due to Tharsis. To quantify long-baseline slopes on Mars, we globally compute slopes on 1000-km baselines by fitting planes of that dimension to locally projected gridded fields. The MOLA-derived topographic field has an absolute accuracy of ~1 m with respect to Mars' center of mass. Even allowing for errors in the height of the geoid of ~5 m [*Lemoine et al.*, 2001], 1000-km surface slopes have precision of better than $\sim 2^\circ \times 10^{-5}$. Figure 3-4 shows the magnitude (color-coded) and direction (arrows) of these regional slopes. It is clear that the majority of the northern hemisphere slopes downward to the north. The lowlands have a typical tilt of 0.02-0.1° with values increasing to 0.4° near the dichotomy boundary in longitudes

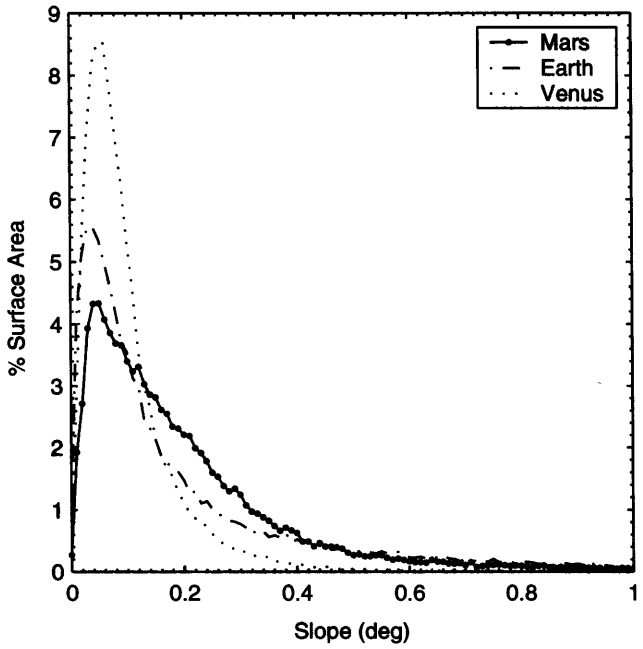

Figure 3-2: A histogram of regional slopes for Mars (solid curve), Earth (dashed), and Venus (dotted). Baselines for slope calculations were 100 km, and bin width is 0.01°, similar to *Sharpton and Head* [1985]. Note the relative abundance of steeper slopes in the range 0.18-0.42° on Mars.

50-210°E and the large volcanos. The basin floor of Hellas (44.3°S, 66.2°E) has an overall easterly tilt, although locally it has some northerly slopes. However, the basin's topography has been significantly altered since its formation [*Tanaka and Leonard*, 1995; *Wichman and Schultz*, 1989], so it is difficult to ascertain its primordial shape. The floor of the Utopia basin (47.6°N, 82.7°E) shows no discernible non-radial tilts by this method and attempts to reproduce the northerly tilt result of *McGill* [2001] where unsuccessful. Naturally, the north polar cap is tilted approximately south, while the south cap is tilted north, giving a quasi-parabolic shape which is consistent with both ablation [*Zwally et al.*, 2000] and glacial flow [*Zuber et al.*, 1998a, c] models, and hence cannot distinguish between them.

Arabia Terra (~30°N, 30°E) is broadly tilted by 0.05°-1.5° to the north-west, a direction to which many of the channels in the region closely adhere. This correspondence is also true in the area of Chryse (27°N, 324°E), although the slopes are ~0.05° steeper. The

correlation between channel direction and gradient azimuth as a function of scale of the local slope is an exciting research direction presently being pursued in greater detail. It is notable here that channels are often oriented in a direction consistent with long-baseline slopes.

Regional trends were also used in an analysis by *Mouginis-Mark et al.* [1982], where slope azimuths were compared to flow directions of Tharsis lava flows, which were taken as paleo-slope indicators. They found almost no deformation associated with loading since the flow emplacement. The more precise slopes computed here are similar to the ones they used and therefore confirm their conclusion that during the current epoch of preserved volcanic activity the lithospheric thickness must be large (perhaps >150 km). This scenario is consistent with the thick elastic lithosphere determined from gravity and topography inversions of *Zuber et al.* [2000].

The orientation of the long-baseline slopes in the southern hemisphere is complicated by large impact and volcanic constructs such as Hellas, Argyre, and Tharsis (Figures 3-3b and 3-3d, Figure 3-4). At regions distant from these features, for example, near longitudes 0° and 170°-180°E (Figures 3-3a and 3-3c, Figure 3-4) slopes appear to be biased toward the north. Still other longitude bands (e.g., $\sim$130°E, 200°-210°E) have random distribution of slope azimuths. The computed slopes indicate that a substantial fraction of the planet is tilted roughly northward, although important departures from that exist, for instance, near Tharsis and Hellas. This supports the long-held view that the majority of the surface of Mars drains north [*Banerdt and Vidal*, 2001], and that the lowlands are a natural sink for not only volatiles but also sedimentary, aeolian and volcanic materials [*Smith et al.*, 2001b]. Although a description of long-baseline slopes is provided by the method presented, the question of possible global tilts remains open and attractive to further investigation using the highly precise MOLA data set.

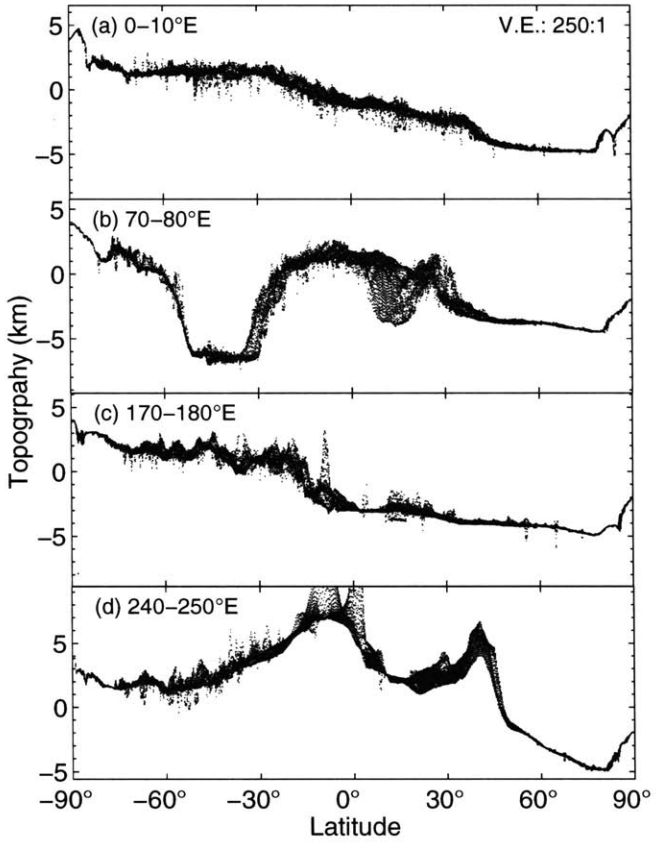

Figure 3-3: Pole-to-pole topographic profiles stacked in selected 10° longitude intervals.

3.5 RMS and Median Slope

Short-wavelength slopes are relevant to regional-scale processes on Mars. In order to investigate short-baseline slopes, MOLA tracks were numerically differentiated by a three-point Lagrange formula,

$$\frac{dy}{dx} = y_0 \frac{2x - x_1 - x_2}{x_{01}x_{02}} + y_1 \frac{2x - x_0 - x_2}{x_{10}x_{12}} + y_2 \frac{2x - x_0 - x_1}{x_{20}x_{21}}, \tag{3.1}$$

for three consecutive points at $\{(x_i, y_i)\}$ with $i = \{0, 1, 2\}$ and $x_{ij} = x_i - x_j$. For equally spaced points this is equivalent to a centered difference scheme. Formally, the result should be viewed as a lower limit on the absolute slope since the measurement is

restricted to the ground-track direction, which may not follow the gradient direction. If the topography field is isotropic, the average properties that follow can easily be corrected for this by dividing by the average value of $|\cos(\theta)|$, that is, $2/\pi$.

It is customary to express surface roughness in terms of the root mean squares (RMS) of slopes θ_r, because radar reflection scatter is largely affected by this parameter. However, a typical slope distribution need not, and in fact rarely does, resemble a Gaussian, which is the distribution for which RMS is the appropriate measure. Point-to-point MOLA slopes can be anomalously large (e.g. owing to small craters or faults) and contribute to a long-tailed distribution. The L2 RMS slope estimate is sometimes dominated by these high slopes and is therefore not always representative of the typical nature of the surface [*Kreslavsky and Head*, 1999; *Neumann and Forsyth*, 1995].

Nonetheless, empirical study shows a surprising agreement between some RMS slope estimates derived from radar observations and from MOLA [*Aharonson et al.*, 1999]. Hence RMS slopes are reported here, but with a cautionary note, especially when these values are high.

RMS slopes were computed in a 35-km running window. The approximately hemispheric crustal dichotomy is manifested, with the southern hemisphere having typical RMS slopes in the range 3°-10° and the northern hemisphere in the range 0.2°-0.8° [*Head et al.*, 1999]. Exceptions to low slopes in the north include the Olympus Mons (18.4°N, 226.9°E) basal escarpment, canyon walls, sparse craters, and the edges of the ice cap deposits, while in the south low slopes are evident in the relatively flat portions of the ice cap deposits.

Radar observations of Mars [*Christensen*, 1986; *Christensen and Moore*, 1992; *Harmon et al.*, 1999] yield values for θ_r in the range 0.25°-10°, very similar to the overall range obtained here. The Tharsis Montes and Olympus Mons areas exhibit relatively high θ_r of $\sim$10° in radar, and the MOLA data agree well. The Amazonian region west of Tharsis (16°N, 201°E) has large θ_r in radar but appears remarkably smooth in MOLA data. This indicates that although this region appears very smooth at MOLA scale, it may be rougher at a smaller scale. Chryse Planitia (27°N, 324°E), whose radar appearance played a role

in site selection for Viking Lander 1, has θ_r of 4°-6° in radar and similarly in MOLA in the southern portion with values decreasing to ~1° in intercrater plains to the north. Syrtis Major at 10°N, 70°E has been observed to have some of the lowest effective θ_r in radar of ~1° down to 0°.25 and shows a slightly larger RMS slope by MOLA. This is an example of a surface that is probably smoother on a scale smaller than MOLA sampling than the point-to-point slopes would imply. Finally, the north polar region has a uniform radar response of θ_r ~2°, in fair agreement with MOLA.

In characterizing typical surface gradients, median absolute slopes were found to be most robust in that adjacent or crossing tracks show similar values. While RMS slopes suffer when distributions are long tailed owing to the averaging of squares of slopes, median absolute slopes are largely unaffected by the height of the distribution's tail [*Kreslavsky and Head*, 1999]. Figure 3-5 shows maps of median slopes in the same format as before.

A comparison with RMS slopes indicates that the median slope values are generally smaller, consistent with the remarks stated previously that a small amount of steep slopes can dominate the RMS measure. It is observed that median slopes contrast surfaces distinctly, so that, for example, the dune-covered Olympia Planitia (82°N, 166°E) appears slightly rougher than the north polar cap margins. Impact basins floor and rim characteristics emerge prominently. The large craters have a common morphology in which the floors are generally smoother than the rims and associated ejecta blankets. An interesting boundary in roughness occurs at the northern margin of the Tharsis province, approximately concentric with Alba Patera (40.5°N, 250.1°E) but ~1200 km north of its center. Median slope values drop from >0.25° on the volcano flank side to <0.15° on the lowlands side. The roughness increases again to the north, forming a crescent-shape region smoother than its surroundings, perhaps related to a volcanic episode.

Another area of particular geological interest in Sinus Meridiani. Recently, probable hematite mineralization has been identified there [*Christensen et al.*, 2000] by the Thermal Emission Spectrometer (TES), an instrument also on board MGS. In Figure 3-6 topography and median slope maps for this region are shown, as well as the mapped distribution

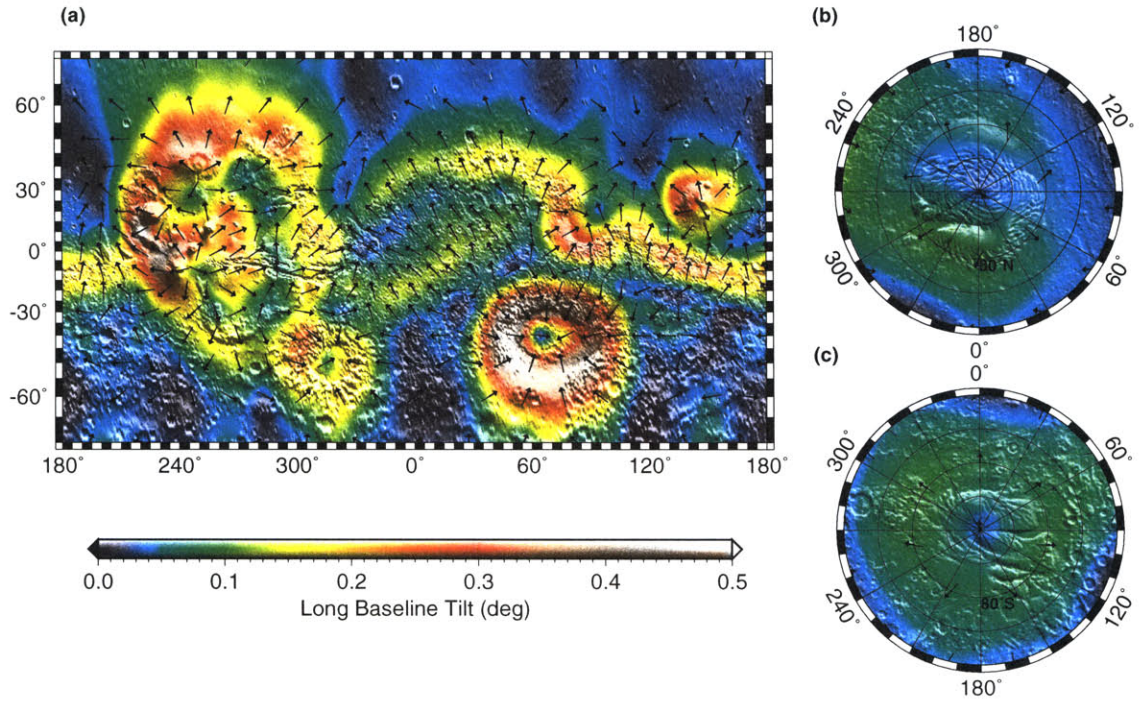

Figure 3-4: Long-baseline (1000 km) tilts. Azimuths are indicated by arrows, and magnitude by color. The fields are in (a) Mercator and (b and c) stereographic projections over the poles. A northeasterly illuminated shaded relief model of the topography is superimposed in monochrome. Note the northerly tilt of much of the northern hemisphere.

of hematite from *Christensen et al.* [2001]. The presence of hematite closely correlates with a smoother region of median slopes $<0.4°$. However, the region appears to have a southwesterly slope and is not a closed depression. *Christensen et al.* [2000] examined two classes of hematite formation mechanisms: one that requires significant amounts of near surface water, and one that does not. The unusual smoothness, if a result of subaqueous sedimentation, favors the first explanation over the latter.

In summary, the measured median slopes are bounded at the lowest values by Amazonis Planitia and some polar cap deposits (further discussion of this will follow). At the highest variation of slope, in order of increasing median, are the Hellas rim, Argyre rim, dichotomy boundary (especially east of 30°E), Olympus Mons aureole, and canyon walls of Valles Marineris, which are in excess of 20°.

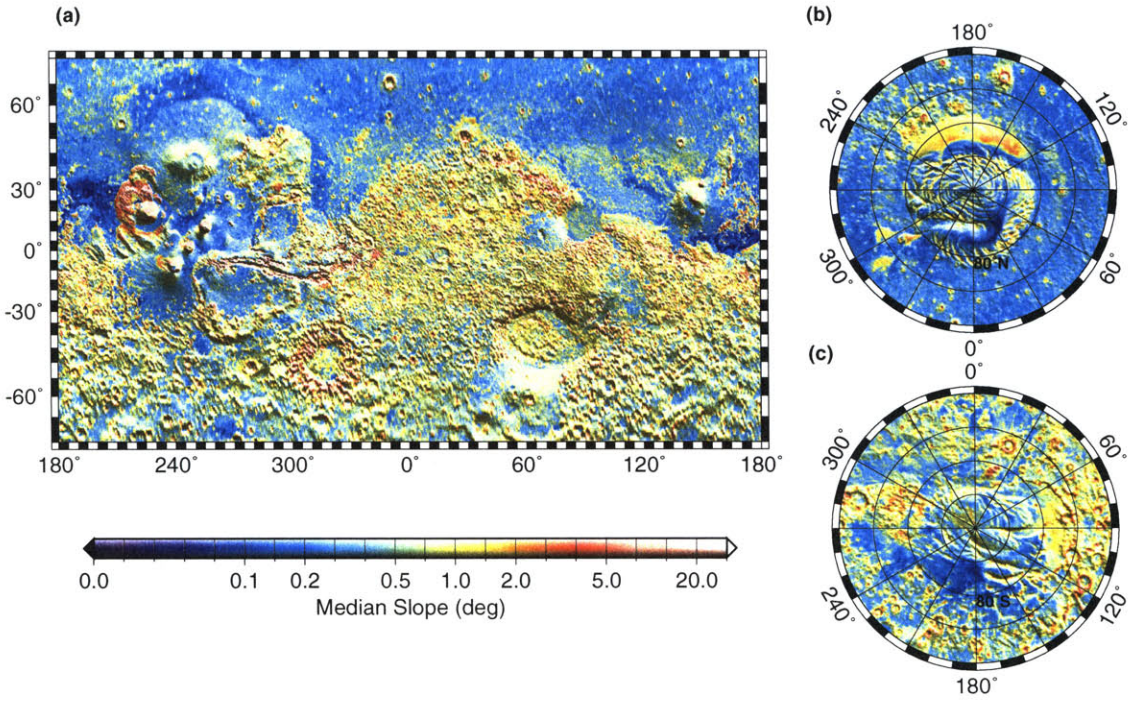

Figure 3-5: Median slopes in 35-km windows. Format is the same as in Figure 3-4. The color scale is nonlinear in order to maintain much of the dynamic range. The tick marks are spaced linearly between labels.

3.6 Interquartile Scale

It is often useful to consider roughness in terms of typical relative elevation deviations rather than slope. One way to achieve this to employ the interquartile scale (IQS). In this characterization we measure the width of a histogram of the 50% most significant elevations, scaled to unity for a normal distribution. Before normalization, this estimator R_q is defined [*Neumann and Forsyth*, 1995] as

$$R_q = \frac{N}{2N-1}(Q_3 - Q_1), \tag{3.2}$$

where Q_i is the elevation of the ith quartile point and N is the number of points. To normalize, R_q is divided by 0.673, the IQS of a normal distribution. The parameter R_q is a robust estimator in the sense that it is not sensitive to outliers in as much as half of the popula-

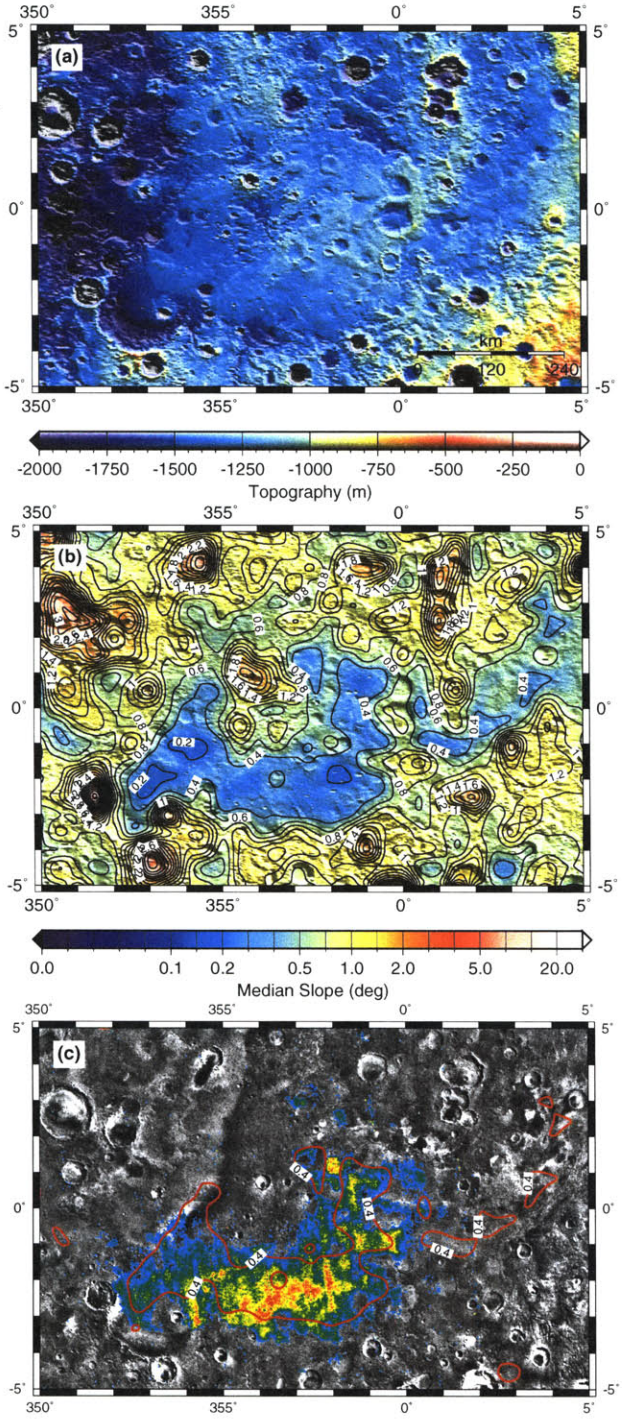

Figure 3-6: The Sinus Meridiani region. Shown are (a) topography, (b) median slopes, and (c) Hematite distribution from *Christensen et al.* [2001] plotted over an image mosaic of the region, with the 0.4° median absolute slope contour also indicated.

tion. This calculation is applied to all range returns that fall within a window sliding along each profile. Although choice of window size can affect the numerical values measured, the qualitative results below remain true (as is the case for the other estimators presented). In its rank 1 statistical nature, IQS is comparable to median slope except that it operates directly on elevations rather than elevation difference (slope). To avoid a regional slope bias, a mean trending surface is removed prior to the calculation. The results, computed in 35-km windows, are plotted in Figure 3-7. One advantage of IQS measurements is that they can be directly compared to vertical roughness as determined from MOLA pulse width measurements [*Garvin and Frawley*, 2000]. The pulse width is sensitive to roughness on smaller scales, up to the laser spot size of $\sim$100 m on the ground. Comparison with the vertical roughness reported by *Smith et al.* [2001b] shows good relative agreement, with the absolute values systematically greater for the larger-scale IQS.

Some observational examples of the IQS measurements over various geological provinces are presented below. Many qualitative observations also appear in the median slopes characterizations.

The northern hemisphere is flat, with a typical interquartile scale of a few tens of meters ranging over thousands of kilometers [*Aharonson et al.*, 1998]. The Olympus Mons aureole deposits are among the roughest surfaces observed, with a typical IQS of hundreds of meters. Compared with the surrounding terrain and the rest of the southern hemisphere, where typical IQS is $>$30 m, the southwest portion of the Hellas impact basin rim appears smoother, with an IQS decreasing to $\sim$10-30 m and extending essentially to the pole. This smoothness has been suggested to be a result of interaction with surface ice [*Kargel and Strom*, 1992; *Squyres and Carr*, 1986], perhaps related to the polar cap.

3.7 Horizontal Decorrelation Length

Thus far, the vertical component of the topography has been characterized by various statistical estimators. One way to define a characteristic horizontal length scale is by es-

timating the distance over which the topography first decorrelates with itself. This distance is obtained by computing the autocovariance function Γ of a sample population $Y = \{y_1, ..., y_N\}$ as a function of the lag L and measuring its width at half maximum. The autocovariance function is estimated by

$$\Gamma(L\Delta) = \frac{1}{N}\sum_{k=1}^{N-L}(y_k - \bar{y})(y_{k+L} - \bar{y}), \tag{3.3}$$

where Δ is the sampling interval, N is the number of samples in the window, and $\bar{y}$ is the mean of Y. The length l, given by

$$\Gamma(l) = \frac{1}{2}\Gamma(0), \tag{3.4}$$

measures the width of the central peak in the autocovariance function. Hence, in the ensuing discussion, l as defined in (3.4) will be referred to as a decorrelation length. Other definitions are possible. The conventional definition for the correlation length can be used to estimate l' with

$$l' = \sqrt{\frac{\sum_{k=1}^{N} x_k^2\,\Gamma(x_k)}{\sum_{k=1}^{N}\Gamma(x_k)}}. \tag{3.5}$$

Here we measure l, rather than l', because l does not depend on the behavior of Γ at large lags. The value of l still depends on window size, but its relative variations over the Martian surface do not. In the following analysis, 35-km windows were employed, as before.

Figure 3-8 shows a map view of the decorrelation length. Several interesting trends emerge. First, a global equator-to-pole increase in decorrelation length is visible from ~1000 m at the equator to ~1800 m near both poles. *Kreslavsky and Head* [2000] observed a similar latitudinal trend in their roughness estimator and suggest that it is related to seasonal deposition/sublimation cycles or alternatively to terrain-softening effects (also seen in changes in crater morphology by *Garvin et al.* [2000]). In the northern hemisphere there is an additional drop in l to ~500 m at several locations (Utopia Planitia, Isidis, northern Chryse Planitia) and a unique drop to ~250 m at Amazonis Planitia. By interpolating

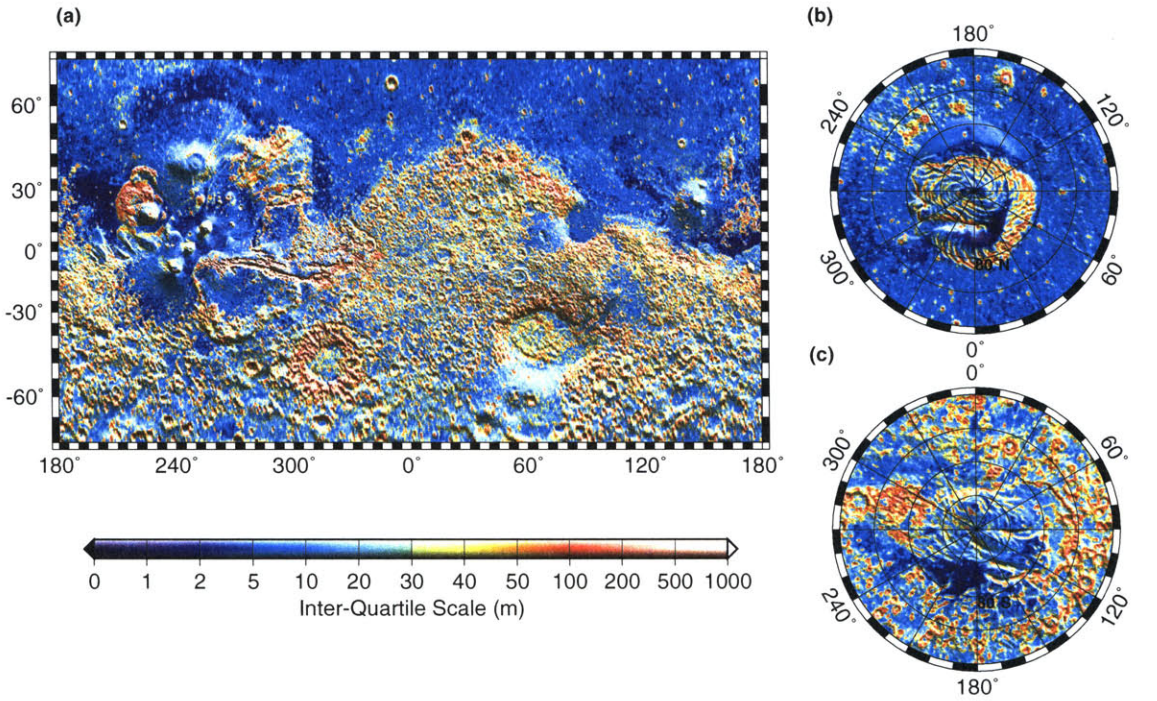

Figure 3-7: Interquartile scale (IQS) in 35-km windows. Format is the same as in Figure 3-4. Note the smoothness of Amazonis Planitia (16°N, 201°E).

the autocovariance function, even shorter values for l are observed distinctly at the polar dune fields, especially in Olympia Planitia (82°N, 166°E). Values of l that are smaller than the sampling distance (~300 m) should be regarded with caution, because they rely on an extrapolation beyond the shortest wavelength observed.

3.8 Power Spectral Analysis

One of the most intriguing hypotheses that has arisen on the basis of data from MGS is the possibility of an ancient liquid water ocean residing in the northern lowlands [*Head et al.*, 1998, 1999]. The relative smoothness of the lowlands, it has been suggested, resulted from sedimentation processes that are expected on an ocean floor. In this section one test of this hypothesis is considered.

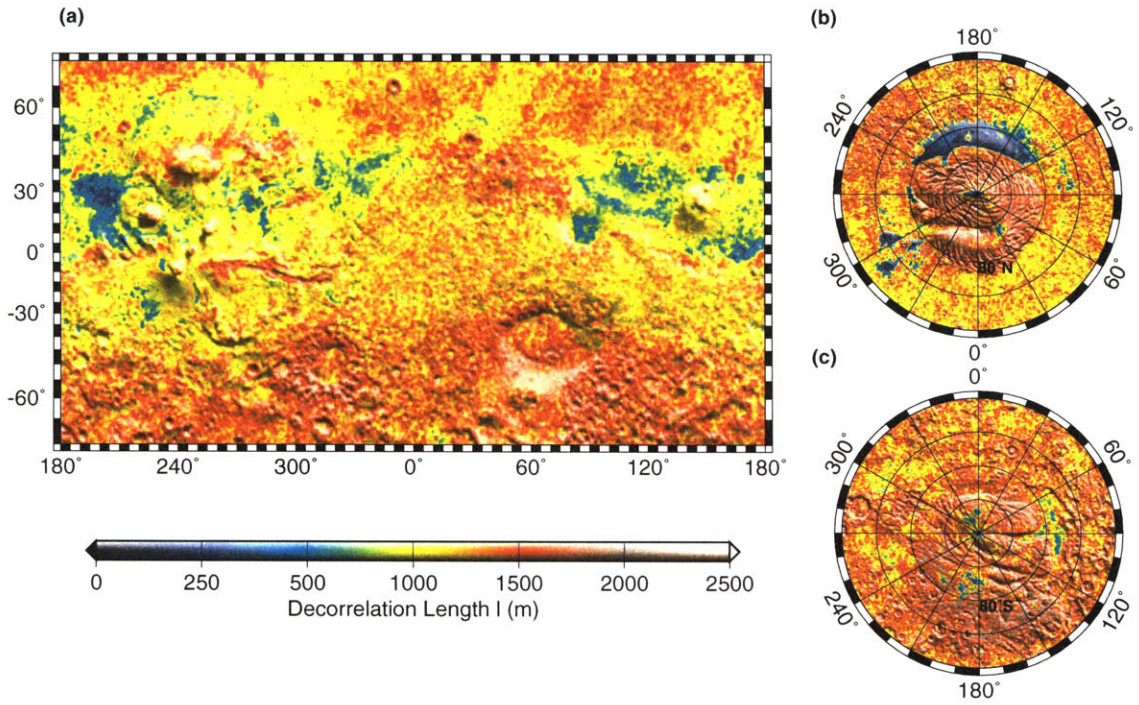

Figure 3-8: Decorrelation length l in 35-km windows. Format is the same as in Figure 3-4. Olympia Planitia (82°N, 166°E) dune fields have distinctly low decorrelation length. A latitudinal trend shifted slightly northward is seen, with typical values increasing poleward by ~50%.

Two areally large regions on Mars have been selected to represent the heavily cratered terrain in the south (region A) and the smooth terrain in the north (region B). Region A is bounded by latitudes 60°S and 30°S and by longitudes 150°E and 210°E. This is the most ancient, heavily cratered crust on Mars, where strong magnetic anomalies have been observed. Region B surrounds the planet in longitude and is bounded by latitudes 60°N-75°N.

The large number of MOLA profiles allows a highly accurate estimation of the power spectrum. In Figure 3-9 the means of one-dimensional spectra along MOLA profiles in these regions are plotted. If the spectrum is roughly divided in two, a short-wavelength portion ($0.7<\lambda<7$ km) and a long-wavelength portion ($20<\lambda<200$ km), then it is seen that although the magnitude of the power in short wavelengths is smaller in region B than

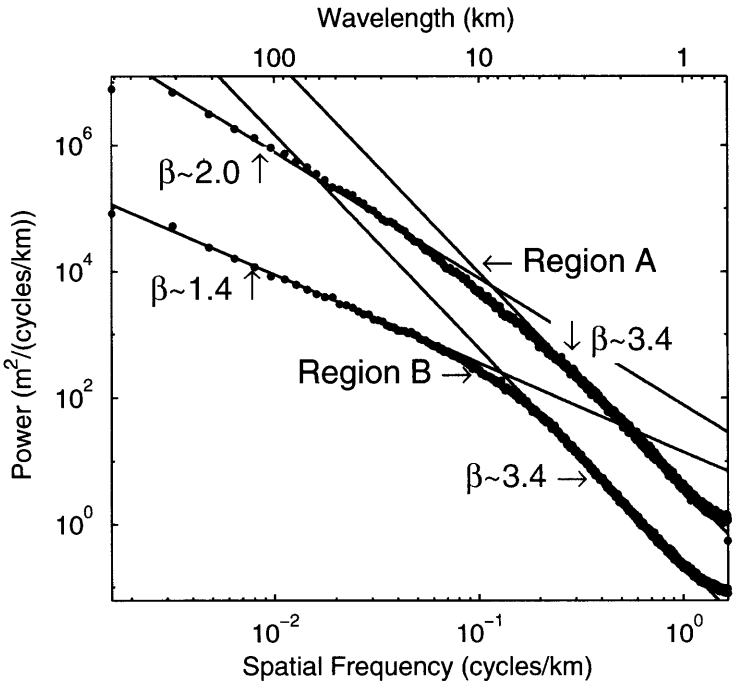

Figure 3-9: Average power spectrum of the topography of an area in the heavily cratered southern terrain (region A) and of an area in the northern lowlands (region B). Note the logarithmic scale, so that slopes indicate power law exponents. In the short wavelengths the effective exponents for the two regions are similar, while in the long wavelengths the exponent of region B is lower than that of region A.

in region A, the slope is almost unchanged. However, the slope of the long-wavelength portion is substantially reduced in region B relative to A.

There is a large body of work on descriptions of scaling relationships in terms of geomorphological models (reviewed by *Dodds and Rothman* [2000]). One simple model for the complex process of sedimentation consists of a diffusion process forced with random noise [*Edwards and Wilkinson*, 1982]. Figure 3-10 illustrates a surface evolving under these conditions. The cartoon shows falling particles being deposited on the surface giving rise to the noise term, with downslope movement of material giving rise to the diffusive term. With this model it is possible to consider if the spectral content of the lowlands appears simply as a diffusively smoothed version of an initially heavily cratered southern terrain.

Regardless of the details, it is expected that any reasonable model would predict that short wavelengths evolve fastest and long wavelengths equilibrate last. For the case of a diffusive model, simple dimensional analysis with a diffusion constant ν, the timescale τ_k for decay of modes of wave number k will be inversely proportional to νk^2. In the steady state limit the spectrum should decay as k^{-2} [*Edwards and Wilkinson*, 1982; *Nattermann and Tang*, 1992].

In a frame comoving with the average height of the surface, the continuum limit of the above model is described by the Edwards-Wilkinson equation [*Edwards and Wilkinson*, 1982], solved in Appendix A with the explicit inclusion of initial conditions. The evolution in time of an average initial spectrum $S(\mathbf{k}, 0)$, given by equation (3.17), is

$$S(\mathbf{k}, t) = e^{-2\nu k^2 t} S(\mathbf{k}, 0) + \frac{(2\pi)^2 \eta_0^2}{2\nu k^2} \left(1 - e^{-2\nu k^2 t}\right), \tag{3.6}$$

where the term on the left-hand side is the time-dependent power spectrum, ν is the diffusion constant, η_0 is the amplitude of the noise, k is magnitude of the 2-D wave vector $\mathbf{k}$, and t is time. Note that as intuition suggested, noisy diffusion affects short-wavelength features (large k in the exponential term) first and that long-wavelength features (small k) are affected last. Furthermore, in the steady state limit the power law exponent predicted in two dimensions is $\beta_r = 2$ (where $S(k) \propto k^{-\beta_r}$). One-dimensional transects taken from this 2-D field will theoretically have an exponent $\beta = 1$ [*Neumann and Forsyth*, 1995; *Voss*, 1991], but in practice the exponent can be greater ($\sim$1.2) owing to finite domain size effects.

The power law exponent in the spectral range of wavelengths 20-200 km shown in Figure 3-9 region B is consistent with evolution of the surface by the above model of sedimentation. In the decade of wavelengths from 0.7 to 7 km the data cannot be explained by noisy diffusion alone, nor in fact by most reasonable models, because they predict fast short-wavelength mode relaxation and slow relaxation in the long wavelengths. A satisfactory explanation of the spectral evolution requires an additional process to steepen the

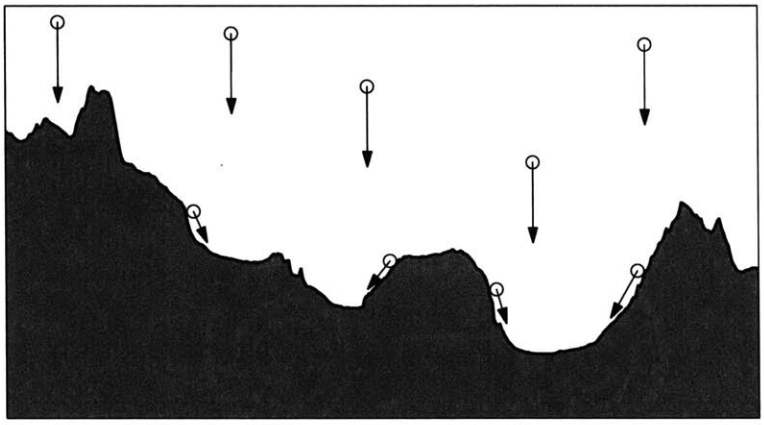

Figure 3-10: Cartoon showing the growth of a surface under a model of noisy diffusion.

slope of the short wavelengths. Such a process could, for example, be cratering. With an appropriate size frequency distribution it can account for the observed power law exponent $\beta \sim 3.4$ for the high-frequency content of both regions. Since large impactors, and therefore large cratering events, are rare, the shallowing of the long-wavelength portion of the spectrum from a slope of ~ 2.1 to ~ 1.4 can be accounted for by a smoothing, diffusion-like process that acts on a faster timescale than the large craters (though still slower than the short-wavelength diffusion).

We therefore conclude that under the assumption of a noisy diffusion model for sedimentation, the lowlands appear as a partially smoothed version of the south in a limited wavelength range. The spectral character can be explained by a diffusive process at long wavelengths, followed by, or concurrent with, cratering at short wavelengths. The possibility that the spectrum of the lowlands was smoothed completely (effectively resetting the surface topography) and then evolved further to its present shape is not excluded by this analysis.

3.9 Landing Site Selection

Of primary importance for the selection of sites for upcoming Mars landers is the threat posed to the safety of the spacecraft on touchdown, the vehicle's likely tilt, and possibly the maneuverability at the site. Such considerations were employed, for example, in the site selection for Viking Lander 2 using radar cross-section data. Although the topographic wavelengths most relevant are smaller than the resolution of MOLA data, the dependence of vertical roughness on scale is typically monotonic. Therefore MOLA data are a powerful discriminator among surfaces in a comparative sense, which can be further calibrated with ground truth.

In Figure 3-11 we demonstrate the use of MOLA to help characterize past landing sites. Figure 3-11a shows median slope roughness for the area that was accessible to the Mars Polar Lander (MPL). The expected current position of the spacecraft is also indicated. At MOLA sampling, smooth plains are prevalent in an area south of 75°S between longitudes 140°E and 180°E, but higher slopes are observed in localized inliers. As shown in Figure 3-11b median slopes of the smooth plains in Chryse Planitia have typical values between 0.15° and 0.3° (as expected, lower than the RMS slope values). The relative smoothness at this scale is consistent with the surface being a depositional in origin. Viking Lander 1 and Pathfinder landed in this area and provide ground truth for radar [*Harmon*, 1997] and MOLA-derived roughness at small scales. The Pathfinder landing site, situated at the mouth of Ares Vallis, is characterized by deposited debris of channelized flows. *Golombek et al.* [1997] find measured slopes there are consistent with an RMS of ~5°.

3.10 Conclusions

The results discussed here represent a snapshot of an ongoing data analysis effort which is progressing in terms of both data volume and coverage, as well as in theory and technique. Thus far, we have demonstrated the advantages of robust estimators over traditional ones and have used them to characterize the Martian surface globally. The global asymmetry

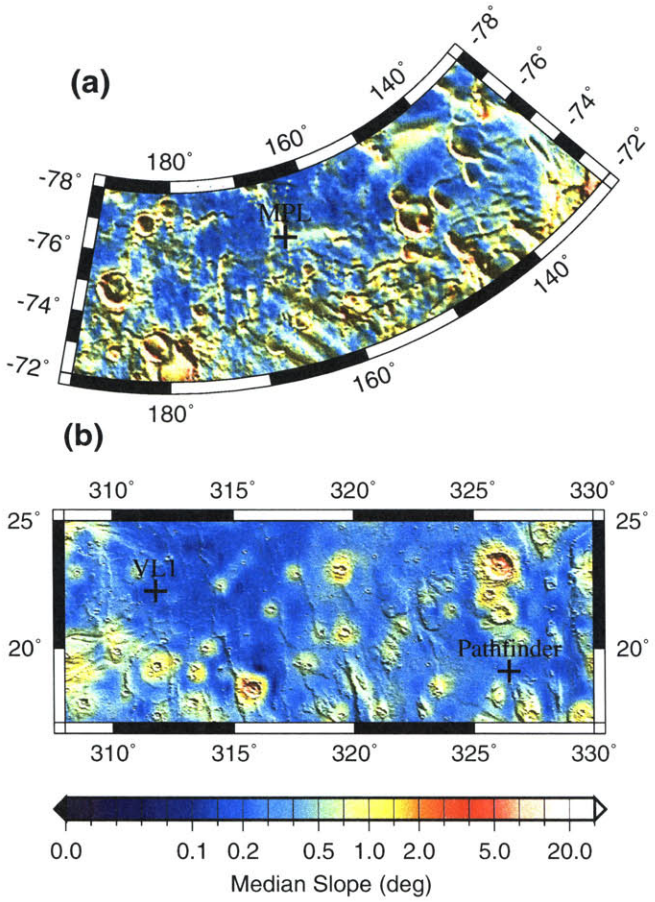

Figure 3-11: Median slope roughness maps of (a) area accessible to the Mars Polar Lander and (b) Viking Lander 1 and Pathfinder sites in Chryse Planitia.

in the crust of Mars manifests itself in the bimodality of the hypsometry, but the elevation distribution function becomes unimodal when referenced to the planetary COF, similar to Venus but not Earth. Outflow channels often follow the direction of long-baseline slopes in the topography. These tilts are mostly facing north in the northern hemisphere and in some parts of the south. It was found that at MOLA sampling baselines the northern hemisphere is smoother than the south and that the vast region of Amazonis Planitia is unusually smooth. Of the measured terrestrial planets' topography, Amazonis is most analogous to heavily sedimented fluvial basins on Earth such as the ocean floor. Although this observation represents a piece of circumstantial evidence rather than proof of geologic origin, and

despite its very early emergence from MOLA data, it has potentially tantalizing ramifications and has so far withstood the tests of repeated measurements and global coverage.

Statistics of topography show that a part of Hellas's rim has undergone intensified erosion, consistent with a hypothesis of smoothing by an ancient glacier or much larger south polar cap. We have further shown how the decorrelation length can be used as a discriminator among geologic surfaces and measured a very short correlation length over the dunes of Olympia Planitia.

A description of the topography in terms of its power spectrum demonstrates the difference between the lowlands and highlands. Modification of the long-wavelength portions of the north's spectrum relative to the south's can be accounted for by a simple depositional model (i.e. noisy diffusion) such as might be expected at an ocean's floor. However, the short-wavelength spectrum cannot by simultaneously matched, and its explanation requires an additional process such as cratering.

MOLA slopes and statistical properties of topography are also being used to characterize potential landing sites for future Mars landers.

3.11 Appendix A: Power Spectrum Evolution

The effect of many physical processes on the height of a two-dimensional interface $h(\mathbf{x}, t)$ as a function of position and time can be modeled with the noisy diffusion equation, which can be derived from the continuum limit of a lattice model of sedimentation [*Edwards and Wilkinson*, 1982]:

$$\frac{\partial}{\partial t} h(\mathbf{x}, t) = \nu \nabla^2 h(\mathbf{x}, t) + \eta(\mathbf{x}, t), \tag{3.7}$$

where ν is a diffusion constant and $\eta(\mathbf{x}, t)$ is a noisy forcing term that is uncorrelated in the ensemble average:

$$\langle \eta(\mathbf{x}', t')\, \eta(\mathbf{x}, t) \rangle = \eta_0^2\, \delta^2(\mathbf{x} - \mathbf{x}')\, \delta(t - t'). \tag{3.8}$$

As have others in the past [e.g., *Barabási and Stanley*, 1995; *Edwards and Wilkinson*, 1982; *Nattermann and Tang*, 1992], we seek a spectral domain time-dependent solution to equation (3.7). Here we explicitly include a prescribed initial condition so that we may examine the evolution of one surface from another (B. Newman, personal communication, 2000).

Rearranging the Edwards-Wilkinson equation (3.7), and correlating it with itself gives

$$\left(\frac{\partial}{\partial t} - \nu\nabla^2\right)\left(\frac{\partial}{\partial t'} - \nu\nabla'^2\right)\langle h(\mathbf{x},t)h(\mathbf{x}',t')\rangle = \langle \eta(\mathbf{x}',t')\,\eta(\mathbf{x},t)\rangle\,. \tag{3.9}$$

Assuming that the field h is stationary in space, the correlation function ρ depends only on $\mathbf{x}-\mathbf{x}'$, and we define

$$\rho(\mathbf{x}-\mathbf{x}',t,t') = \langle h(\mathbf{x},t)h(\mathbf{x}',t')\rangle\,. \tag{3.10}$$

Furthermore, $\nabla^2\rho = \nabla'^2\rho$, we can replace $\mathbf{x}-\mathbf{x}'$ with $\mathbf{x}$ and substitute (3.8) and (3.10) into (3.9), to obtain

$$\left(\frac{\partial}{\partial t} - \nu\nabla^2\right)\left(\frac{\partial}{\partial t'} - \nu\nabla^2\right)\rho(\mathbf{x},t,t') = \eta_0^2\,\delta^2(\mathbf{x})\,\delta(t-t'). \tag{3.11}$$

Multiplication by $e^{-\imath\mathbf{k}\cdot\mathbf{x}}$, and integration over all $\mathbf{x}$, yields

$$\left(\frac{\partial}{\partial t} - \nu k^2\right)\left(\frac{\partial}{\partial t'} - \nu k^2\right)S(\mathbf{k},t,t') = (2\pi)^2\eta_0^2\delta(t-t'), \tag{3.12}$$

where $k = |\mathbf{k}|$, and S is defined as

$$S(\mathbf{k},t,t') = \frac{1}{(2\pi)^2}\int \rho(\mathbf{x},t,t')e^{-\imath\mathbf{k}\cdot\mathbf{x}}d\mathbf{x}, \tag{3.13}$$

assuming that ρ decays with $|\mathbf{x}| \to \infty$ sufficiently fast that the integral converges, i.e., that the Fourier transform of the correlation function exists. When $t = t'$, we identify $S(\mathbf{k},t,t) \equiv S(\mathbf{k},t)$ as the power spectrum, in accordance with the Wiener-Khinchine theorem [e.g., *Gardiner*, 1985].

Rearrangement (using an integrating factor) of the left-hand side of (3.12) yields

$$e^{\nu k^2(t+t')}\frac{\partial}{\partial t'}\frac{\partial}{\partial t}e^{\nu k^2(t+t')}S(\mathbf{k},t,t') = (2\pi)^2\eta_0^2\delta(t-t'). \tag{3.14}$$

Multiplying by $e^{-\nu k^2(t+t')}$, integrating from 0 to t and 0 to t', and finally taking the particular case $t = t'$ gives, after some algebra (allowing for both $t < t'$ and $t > t'$),

$$S(\mathbf{k},t) = e^{-\nu k^2 t}S(\mathbf{k},t,0) + e^{-\nu k^2 t}S(\mathbf{k},0,t) - e^{-2\nu k^2 t}S(\mathbf{k},0,0) + \frac{(2\pi)^2\eta_0^2}{2\nu k^2}\left(1 - e^{-2\nu k^2 t}\right). \tag{3.15}$$

By assuming that the initial field and the stochastic forcing are uncorrelated, so that, for example, $\langle \eta(\mathbf{x},t)h(\mathbf{x}',0)\rangle = 0$, we can multiply (3.7) by $h(\mathbf{x}',0)$ and repeat the above steps to find

$$S(\mathbf{k},t,0) = S(\mathbf{k},0,t) = e^{-\nu k^2 t}S(\mathbf{k},0,0). \tag{3.16}$$

Taking $S(\mathbf{k},0) \equiv S(\mathbf{k},0,0)$ as the spectrum of the initial field, and substituting (3.16) into (3.15), the time-dependent power spectrum is

$$S(\mathbf{k},t) = e^{-2\nu k^2 t}S(\mathbf{k},0) + \frac{(2\pi)^2\eta_0^2}{2\nu k^2}\left(1 - e^{-2\nu k^2 t}\right). \tag{3.17}$$

The qualitative behavior of the evolution under noisy diffusion is shown in Figure 3-12.

3.12 Appendix B: Summary of stochastic parameters

A number of interrelated parameters have been proposed to study the statistical nature of a surface. We briefly review their definitions and relationships [e.g., *Turcotte*, 1997].

For a topographic field z, sampled at locations x_i, with $i = 1, .., n$, the RMS height is simply define as

$$\sigma^2 = \left\langle [z(x_i) - \bar{z}]^2 \right\rangle \tag{3.18}$$

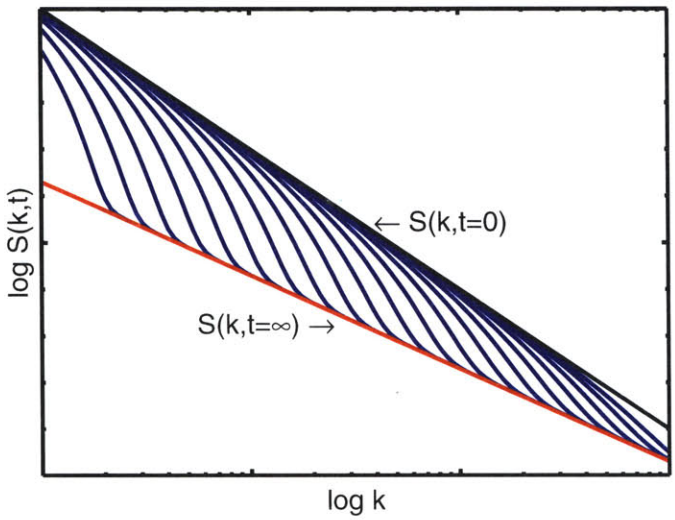

Figure 3-12: Qualitative evolution under noisy diffusion.

where the angle brackets $\langle ... \rangle$ denote the ensemble average, and $\bar{z} = \langle z(x_i) \rangle$ The variogram, also known as Allan deviation, RMS deviation, or structure function, is

$$\nu^2(\Delta x) = \left\langle [z(x_i) - z(x_i + \Delta x)]^2 \right\rangle \tag{3.19}$$

where Δx is called the "lag". A linear trend or a constant mean is often removed from the signal prior to processing. In that case,

$$\sigma = \nu(0). \tag{3.20}$$

A closely related parameter is obtained by considering the fluctuations of slopes instead of height differences, giving the RMS slope s_{rms}. For a signal sampled at regular intervals, this is simply,

$$s_{\text{rms}}(\Delta x) = \frac{\nu(\Delta x)}{\Delta x} \tag{3.21}$$

If the structure function is a power-law of form $\nu \propto \Delta x^H$, then the exponent H is referred to as the Hurst exponent. The RMS slope function, s_{rms}, then has the form $s_{\text{rms}} \propto \Delta x^{H-1}$.

Alternatively, the fractal dimension D can be related to H by

$$D = d + 1 - H \tag{3.22}$$

where d is the number of spatial dimensions. The auto-correlation function, C, is

$$C(\Delta x) = \langle z(x_i)z(x_i + \Delta x)\rangle \tag{3.23}$$

The structure- and auto-correlation functions are easily related by,

$$\nu^2(\Delta x) = 2\sigma^2 - 2C(\Delta x) \tag{3.24}$$

and for a continuous signal, by the Wiener-Khinchine theorem, the correlation function can be related to the power spectrum S by

$$S(f_x) = \mathcal{F}\{C(x)\}, \tag{3.25}$$

where $\mathcal{F}$ is the Fourier transform operation. If the spectrum is a power law of the form $S \propto f_x^{-\beta}$, then a frequently quoted result is that β and H are related by

$$\beta = 2H + 1 \tag{3.26}$$

The analytical linear relationship between β and H is derived for a continuous signal in an infinite domain. For a discretely sampled, finite signal, as H approaches 0 and 1, the approximation degrades.

Acknowledgments

We thank John Goff and Bill Newman for careful reviews and acknowledge helpful discussions with Greg Neumann and Jim Head. It was our pleasure to incorporate comments

by Bill Newman on an early draft of this paper, which helped formulate Appendix A in a more precise manner. This study was supported by the generous Kerr Fellowship, the Mars Global Surveyor Project, and by DOE grant DE FG02-99ER 15004.

Chapter 4

Drainage basins and channel incision

Originally published in:
Aharonson, O., M. T. Zuber, D. H. Rothman, N. Schorghofer, and K. X. Whipple, Drainage basins and channel incision on Mars, *Proc. Nat. Acad. Sci.*, *99*, 1780–1783, 2002

Abstract

Measurements acquired by the Mars Orbiter Laser Altimeter on board Mars Global Surveyor indicate that large drainage systems on Mars have geomorphic characteristics that are inconsistent with prolonged erosion by surface runoff. We find the topography has not evolved to an expected equilibrium terrain form, even in areas where runoff incision has been previously interpreted. By analogy with terrestrial examples, groundwater sapping may have played an important role in the incision. Consequently, requirements for a persistent warm and wet climate based on morphology of drainage features may be unnecessary. Longitudinally flat floor segments may provide a direct indication of lithologic layers in the bedrock, altering the subsurface hydrology. However, it is unlikely that the floor levels are entirely due to inherited structures due to their planar cross cutting relations. These conclusions are based on previously unavailable observations including extensive piece-wise linear longitudinal profiles, frequent knickpoints, hanging valleys and small basin concavity exponents.

4.1 Introduction

Valley networks and channels on Mars were discovered during the Mariner 9 mission [*Masursky*, 1973; *McCauley et al.*, 1972]. Alternatives for their origin have been suggested, but the most widely accepted formation hypothesis is by erosion, and the most likely erosive agent is water [*Baker*, 1982; *Carr*, 1981]. The interpretation of ubiquitous erosion by surface runoff has often been taken to imply a warmer, wetter climate on early Mars than the present cold and tenuous atmosphere can support [e.g. *Craddock and Howard*, submitted, 2002; *Sagan et al.*, 1973]. Recent precise observations of Martian topography [*Smith et al.*, 2001b] afford for the first time the opportunity to carry out the type of watershed analysis that has been traditionally restricted to Earth, developing quantitative measures relevant to erosion style and intensity.

Channel incision can result from both surface runoff and groundwater sapping. The former process results from the shear stresses induced by overland flow, the latter from the removal of material and mass movement as groundwater seeps out to the surface. The relative contributions of surface runoff and groundwater sapping to carving the valley networks and channels on Mars is of primary importance because large amounts of precipitation required for runoff origin imply climatic conditions that are substantially different from the present ones. If channel incision and drainage basin evolution by runoff erosion can be shown to be weak, then requirements for persistent warmer, clement, climatic conditions are weakened. However, lacking rainfall, the problem of recharging the large aquifers necessary for voluminous seepage remains.

Morphometric criteria have been developed to detect incision by groundwater sapping [*Gulick*, 2001; *Gulick and Baker*, 1990; *Kochel and Piper*, 1986; *Laity and Malin*, 1985]. A distinction can be made by the change of valley widths, which increase downstream for runoff features but remains essentially constant for sapping features; by the shape of valley heads, which are tapered in rivers but theater-formed for sapping features; and by dendritic networks that are indicative of surface runoff. Such criteria require only planimetric images. Knowledge of the topography permits extension of such analyses using additional

quantitative criteria. Longitudinal stream profiles, locations of channels relative to surface topography, and transverse cross-sections of valleys [*Goldspiel and Squyres*, 2000; *Williams and Phillips*, 2001] may now be used to constrain the genesis and evolution of Martian valleys.

4.2 Method

Watershed analysis of drainage systems carried out here has been developed and tested extensively in terrestrial landscapes [*Tarboton*, 1997]. The method is used to determine flow direction and local slope at each grid cell, hence providing the integrated contributing area, the locations of streams and basin boundaries for a given region of interest.

The slope magnitudes are computed as

$$S(\vec{r}) = \frac{T(\vec{r}) - T(\vec{r'})}{|\vec{r} - \vec{r'}|}, \tag{4.1}$$

where $\vec{r}$ and $\vec{r'}$ are the locations of two neighboring cells, and $T(r)$ is the elevation field. For each cell the 8 immediate neighbors are considered. Panel a) in Figure 4-1 illustrates a cell draining in the steepest descent direction, that is into its lower-left neighbor.

Cells with undefined flow directions are resolved iteratively, by assigning them the direction of their lowest neighbor with a defined flow direction. The total area draining into each cell is referred to as the contributing area A. Given a region of interest, the outlet is the cell with the highest drainage area. A main stream is determined by tracing the path of largest drainage areas starting from the outlet, until the basin boundary is reached. Smaller "pits" are artificially filled, allowing the computation to proceed through them. The level of the filling is selected such that the flow is uninterrupted in the main channel. As shown in panel b) of Figure 4-1, the local slope, drainage basin, and its area, can be associated with each point in the domain.

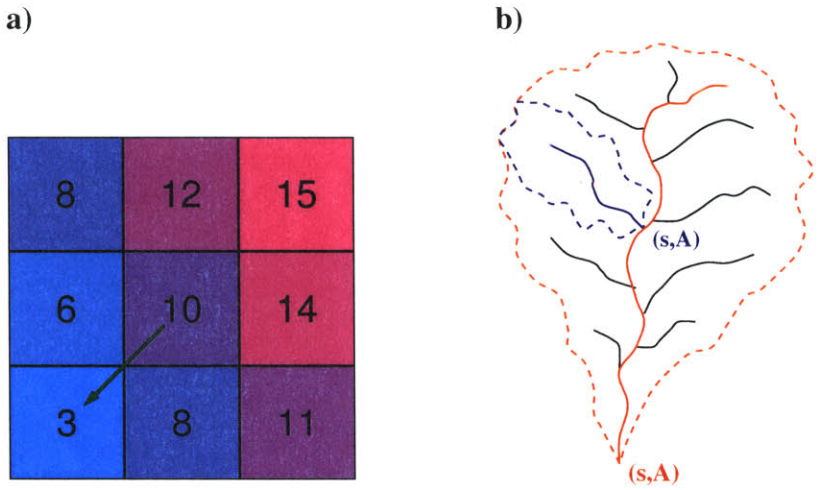

Figure 4-1: Watershed calculation. Panel a) is represents 9 grid cells for which the center cell drains in the steepest gradient direction, that is the lower left cell. Once flow directions are assigned, a local slope, contributing basin, and its area can be associated with each point, as shown in panel b).

4.3 Terrestrial Analog

On Earth, the lower Escalante River, located on the Colorado Plateau, provides a useful analog [*Laity and Malin*, 1985]. While presumably subject to similar climatic conditions, the eastern and western tributary arms of the river have eroded in drastically different styles. Morphological analysis [*Laity and Malin*, 1985] has indicated that tributaries west of the Escalante river evolved primarily by surface runoff erosion. Fifty Mile Creek, shown in Figure 4-2, is an example of such a valley.

East of the river, channel incision appears to have progressed via head-ward erosion of the cliff-face, aided by seepage of groundwater at its base. The topography of runoff channels west of the Escalante river is almost without exception concave upwards. Longitudinal profiles along streams are usually smooth. The basins, incised by dendritic networks, exhibit a strong correlation between local slope and contributing area. The main stream typically tends towards the drainage basin center. In contrast, east of the river the canyon floors are linear or only slightly concave, and individual sections are separated by knickpoints.

For example, in Bown's Canyon (Figure 4-3) the steep knickpoint in the longitudinal profile (panel b), is clearly seen. The lowest floor segment follows an impermeable lithologic layer identified as the Kayenta Formation, although in places the stream incises through the layer. The overland supply channels for the canyons show no systematic profile shape. Terrain concavity is small or non-existent, and hence local slope is largely uncorrelated with drainage area. The canyons at this site often tend towards the drainage basin boundaries.

4.4 Stream Profiles on Mars

Previous models of the Martian topography [*Esposito et al.*, 1992] did not permit a reliable quantitative characterization of fluvial morphologies. Photometric and stereo techniques were used to derive local topography [*Goldspiel and Squyres*, 2000; *Goldspiel et al.*, 1993; *Pieri*, 1980] but lacked precise slope information. However, recent measurements made by the Mars Orbiter Laser Altimeter (MOLA) [*Smith et al.*, 2001b] on board the Mars Global Surveyor (MGS) [*Albee et al.*, 2001] allow construction of a digital elevation model (DEM) from topographic profiles of typical vertical accuracy $\sim$ 1 m, interpolated on a grid with spatial resolution 1 km $\times$ 1 km. The derived DEM is coarser than the data in the latitudinal direction, since along track shot-spacing is $\sim$ 300 m, and is interpolated in the longitudinal direction since track spacing is typically $\sim$ 2 km at the equator and decreases polewards.

Several prominent drainage systems on Mars were analyzed. The first example, Ma'adim Vallis, is situated at the north margins of Terra Cimmeria in the southern highlands. The valley is incised in ancient Noachian terrain, and drains into Gusev crater in the north. Incision by runoff erosion has been inferred [*Carr and Clow*, 1981; *Masursky et al.*, 1977; *Sharp and Malin*, 1975] based on interpretation of features in Viking images, including V-shaped valleys draining into the main channel trunk and their associated tributary networks. A reclassification as a longitudinal valley was later preferred [*Baker*, 1982]. Sapping processes were later suggested [*Cabrol et al.*, 1998] to play a role in carving the valley, with multiple episodes of flow.

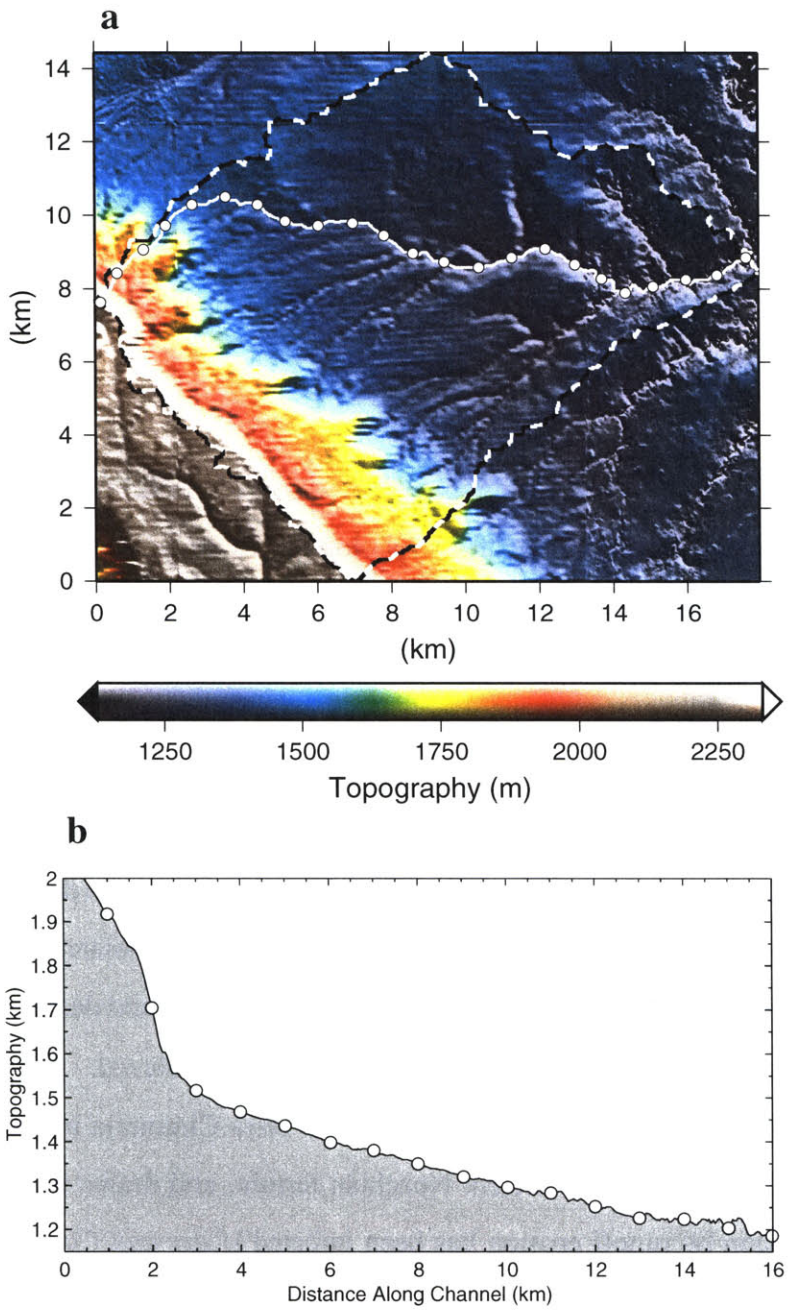

Figure 4-2: Topography of Fifty Mile Creek, Utah (a) map view, and (b) longitudinal profile. In (a), the drainage basin boundary is indicated by a dashed line, and the main stream by a solid white line. In both panels, 1 km intervals along the stream are indicated by circles.

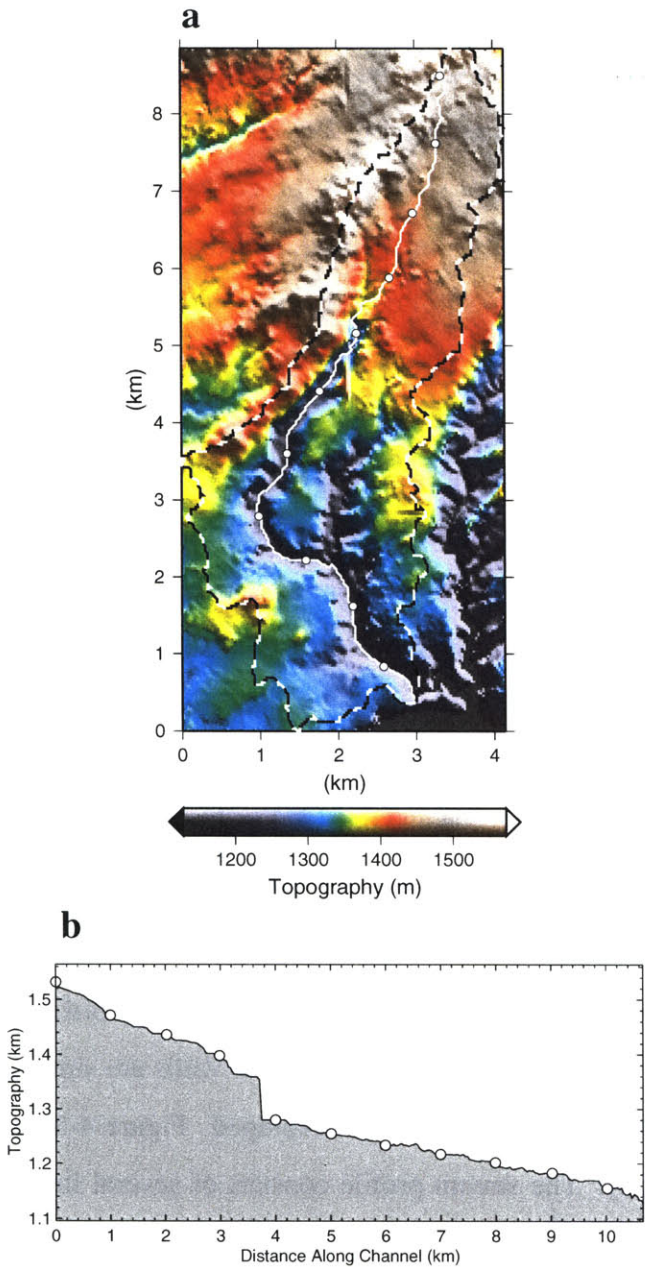

Figure 4-3: Topography of Bown's Canyon, Utah (a) map view, and (b) longitudinal profile. In (a), the drainage basin boundary is indicated by a dashed line, and the main stream by a solid white line. In both panels, 1 km intervals along the stream are indicated by circles.

Drainage basin boundaries and the main stream, as computed by watershed analysis, are shown in a map view of the topography in Figure 4-4a. The outlet (endpoint) of the stream corresponds to one of the craters superimposed on the channel. Figure 4-4b shows the longitudinal topography profile of the main stream as a function of distance along the channel. Downstream from approximately 290 km, where drainage area is high, the channel floor has a relatively constant slope (*i.e.* no concavity is present). A relatively steep knickpoint is present at about 270 km. Uphill, approximately in the first 0-260 km, small upwards concavity is observed. Short convex segments are seen along the profile. Convex segments are particularly prone to erosion and hence attest to the juvenile fluvial character of the system. In addition, in Figure 4-4a the bisection of the drainage basin by the main stream is strongly asymmetrical. This geometry is characteristic of terrestrial sapping canyons, but is atypical in well-developed over-land flow [*Kochel and Piper*, 1986]. Figure 4-4c shows the contributing area map for this region. To obtain a continuous watershed, a large number of local minima must be artificially filled, reflecting the unevolved nature of the surface with respect to runoff erosion [*Banerdt and Vidal*, 2001]. This is also evident in Figure 4-4c by the low density of tributaries and the paucity of high order streams that are not significantly different inside and outside the drainage basin boundaries. Further, the drainage density is low when compared with typical terrestrial runoff environments [*Carr*, 1995; *Carr and Chuang*, 1997].

Although previously considered a runoff channel [e.g. *Baker*, 1982, and references therein], the results from analysis of the Al-Qahira Vallis are similar to those of Ma'adim Vallis in that runoff erosion appears underdeveloped. Figure 4-5 shows the basin (a) and stream (b) topography. The stream profile consists of several linear segments, with little or no concavity. Hanging valleys, or tributary streams elevated with respect to the main trunk, are observed at ~210-360 km and ~360-540 km along channel (also recognized for example in Nirgal Vallis [*Baker*, 1982]). The deep minimum at ~350 km along the channel may be a structure that postdates the channel formation.

Lithological structures and zones of weakness in Mars' bedrock may be evident in the

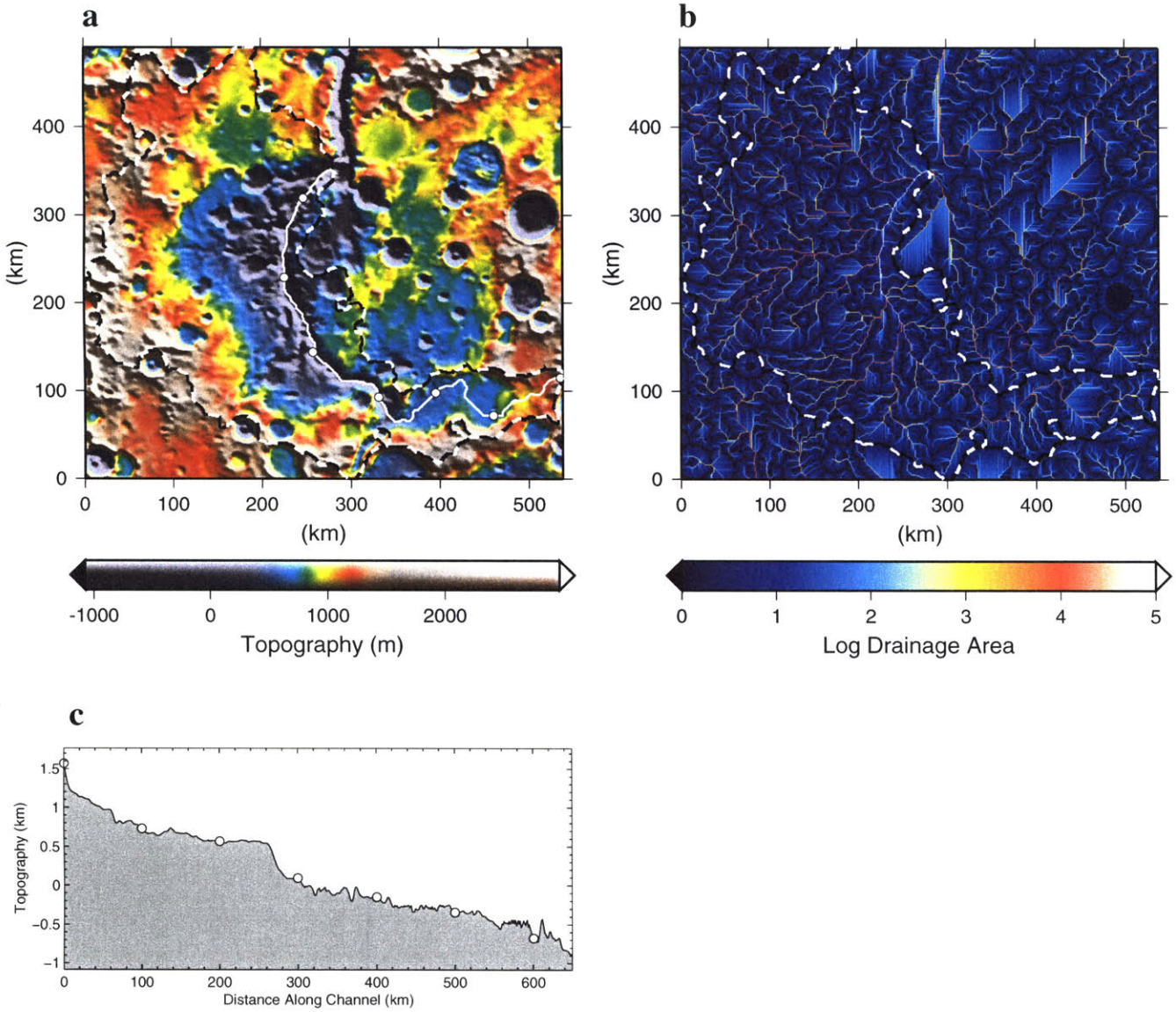

Figure 4-4: Topography of Ma'adim Vallis, Mars (a) map view, and (b) longitudinal profile. Panel (c) shows a drainage area map, computed by the watershed methodology as described. The basin boundary and main stream are indicated as in Figure 4-3. Circles indicate 100 km intervals along the stream. To identify the main channel in the watershed analysis small pits in the topography have been filled. The longitudinal profile shows the unfilled topography.

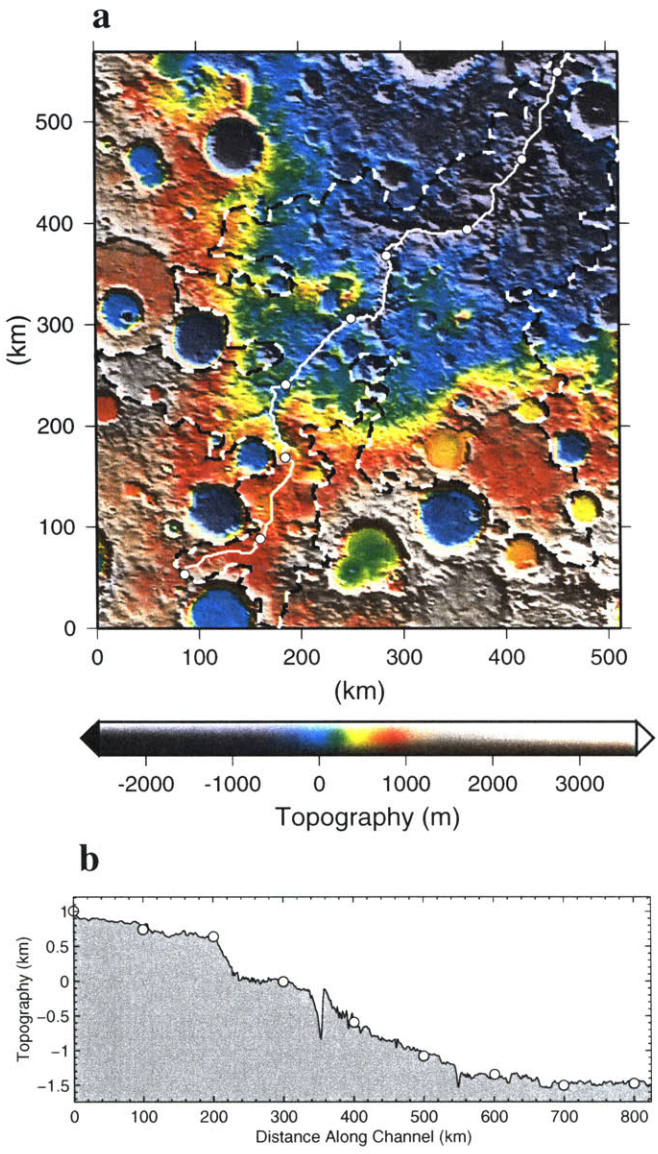

Figure 4-5: Topography of Al-Qahira Vallis, Mars (a) map view, and (b) longitudinal profile. The basin boundary, main stream and 100-km intervals are indicated as in Figure 4-3.

longitudinally flat floor segments, knickpoints and hanging valleys. The indication of layers may be independent of the precise nature of the erosion process, as the interface between two layers of different strength or permeability is a likely site of intensified erosion for a range of mechanisms. On smaller scales, pervasive layering has been observed [*Malin and Edgett*, 2000b; *Malin et al.*, 1998] throughout the upper crust, and the ground water hydrological systems would certainly be controlled by any subsurface structures [*Baker*, 1982; *Baker et al.*, 1991; *Clifford*, 1993]. However, a comparison of strike and dip orientations of planar surfaces fitted to floor profiles reveals that these surfaces are frequently cross cutting even within one valley system. We therefore conclude that while inherited structures may be responsible for individual stream features, they cannot easily account for the overall topography of the valley system (see Appendix A).

4.5 Basin Concavity

Many studies in terrestrial drainage environments [e.g. *Flint*, 1974; *Howard and Kerby*, 1983; *Whipple et al.*, 1999]), laboratory experiments [*Howard and McLane*, 1988], and numerical simulations [*Howard*, 1994; *Willgoose et al.*, 1991] find general drainage characteristics that are seldom violated. Among these characteristics are smooth valley profiles with distinctive upwards-concave shape, that is equivalent to a local slope decrease in the down-valley direction. This observation is often written in terms of a power law relationship between local slope S and contributing area A,

$$S \sim A^{-\theta}, \tag{4.2}$$

where θ is the concavity exponent. For terrestrial fluvial systems, the exponent θ is typically in the range $0.3 - 0.7$ [*Flint*, 1974; *Tarboton et al.*, 1989; *Whipple and Tucker*, 1999].

The concavity absent from longitudinal profiles on Mars is also weak in basin averaged quantities. Figure 4-6 shows average local slope S plotted against contributing area A for each of the two aforementioned Martian drainage basins. The slope data is sorted in

logarithmically spaced bins in A, and the logarithms of the slopes are averaged within each bin. The exponent θ can be inferred from the slope of curves plotted in log-log space. The results for Ma'adim and Al Qahira Valles are consistent: over ~3 orders of magnitude in A, where $A > 30$ km^2, θ is small. The scatter in the slopes introduces variability in θ, and S only weakly depends on A. Also shown for reference are lines corresponding to $\theta = 0.3$, a value that is comparatively low but still appropriate for some terrestrial runoff environments [*Howard et al.*, 1994; *Whipple and Tucker*, 1999]. In the range of high drainage areas, fits to the averaged slope data yield values for θ indistinguishable from those expected for random topography [*Schorghofer and Rothman*, 2001]. Hence, the slope-area relations show no evidence for extensive fluvial sculpting of the terrain in an environment where flow discharge increases steadily downstream, as would be expected for sustained, runoff-driven erosion. At the low drainage area supply region, where $A < 30$ km^2, θ is in the range 0.2-0.3, consistent with expectations for transport-limited erosion of fine-grained material [*Howard et al.*, 1994]. However, even the slightly higher exponent at lower drainage areas is similar to that observed for undissected topography of Mars and Earth, as well as some random surfaces [*Schorghofer and Rothman*, 2001].

4.6 Summary

Similar results are obtained for other fluvial systems on Mars, such as Nanedi Vallis and canyons on the south wall of Valles Marineris [*Kochel and Piper*, 1986]. While several processes and a complex evolutionary history may be required to explain fluvial features on Mars, we find that for the examples considered here, surface runoff appears to have played at most a superficial role in the evolution of the Martian landscape. The relative infrequency of dissection over much of the Martian surface [*Carr*, 1995; *Carr and Chuang*, 1997] down to the scales of highest resolution images [*Malin and Carr*, 1999], has also been used to argue against voluminous runoff, and the required implication of a sustained early warm climate. Morphologic evidence for surface-runoff certainly exists [*Craddock*

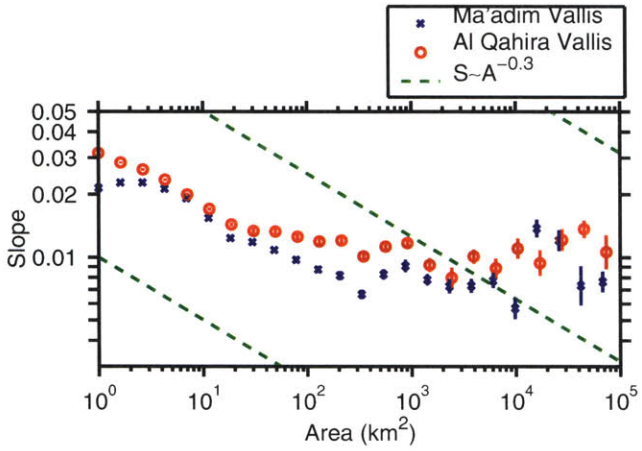

Figure 4-6: Slope-area relations for Ma'adim (crosses) and Al-Qahira (circles) Valles. Vertical bars indicate the standard errors in the mean slope. Also shown are reference lines (dashed) with concavity exponent $\theta = 0.3$. Since local slope falls off with area more slowly than in known fluvially eroded basins, we deduce that erosion by surface runoff was limited in these areas on Mars.

and Howard, submitted, 2002], but the results here indicate that there has not been a significant amount of landscape evolution by fluvial erosion in areas where runoff incision has been previously interpreted. Although other valley incision processes are not ruled out by this analysis, multiple physiographic characteristics support groundwater sapping as an important contributor to the formation of the channels examined.

Taken together, these topographically-derived measurements indicate that the channels and associated drainage basins considered here have not been subject to significant, sustained runoff erosion. Dendritic networks have long been observed near Ma'adim and Al-Qahira Valles, and their topographic properties appear in low drainage area regions. The emerging picture is that the large volumes of incision are relatively unevolved with respect to overland runoff erosion, and runoff networks incise the surface superficially at the uphill source regions. While the topography of an individual segment may be lithologically controlled, extensive layers are inconsistent with the orientations of multiple segments within the drainage systems. Quantitative analysis of fluvial topography in concert with further

study of terrestrial analogs hold the promise of evaluating the extent to which lithologic heterogeneity, intensity of erosion, and erosion process have influenced morphology of river channels and hence the ancient hydrology of Mars.

4.7 Appendix A: A Search for Lithologic Beds

Variations in material properties manifested as lithologic layering is often a controlling factor in terrestrial river bed incision. The extensive piece-wise linear profiles seen on Mars could be indicative of a similar control. In order to test this possibility, we construct planar fits to stream-bed profiles, and consider their self consistency.

As an example, we focus on the Al-Qahira drainage system because it contains large branches that sample a number of different directions, improving the estimates of of strikes of fitted planes. Stream paths were extracted from the DEM by tracing the direction of steepest descent starting from a number of stream heads, and segments were numbered sequentially. The system is shown in map view in Figure 4-7(a).

The topographic profiles along stream segments are plotted in panels (b) and (c) of Figure 4-7. Panel (b) shows that the stream floors at the upper reaches of the system can be fitted well by a single planar surface. The planar fit, evaluated at the stream locations is shown by the dashed lines. The transect does not appear linear due to the curves and turns of the stream. The dip of the plane is $\sim 0.5°$, and the strike is easterly ($\sim 90°$ azimuth, measured clockwise from the north). This same plane fails to fit the linear segments in the lower portion of the system. The lower main branch and its tributaries (segments 4,7, and 8) can be approximated by another plane, dipping at $\sim 0.4°$ in a north-westerly direction ($\sim 305°$ azimuth).

No single plane, nor any number of parallel planes, can simultaneously and adequately fit the set of stream floor segments. While inherited structures may be responsible for individual stream features, we conclude lithology alone cannot account for the overall topography of the valley system. Finer scale structure cannot be ruled out based on this

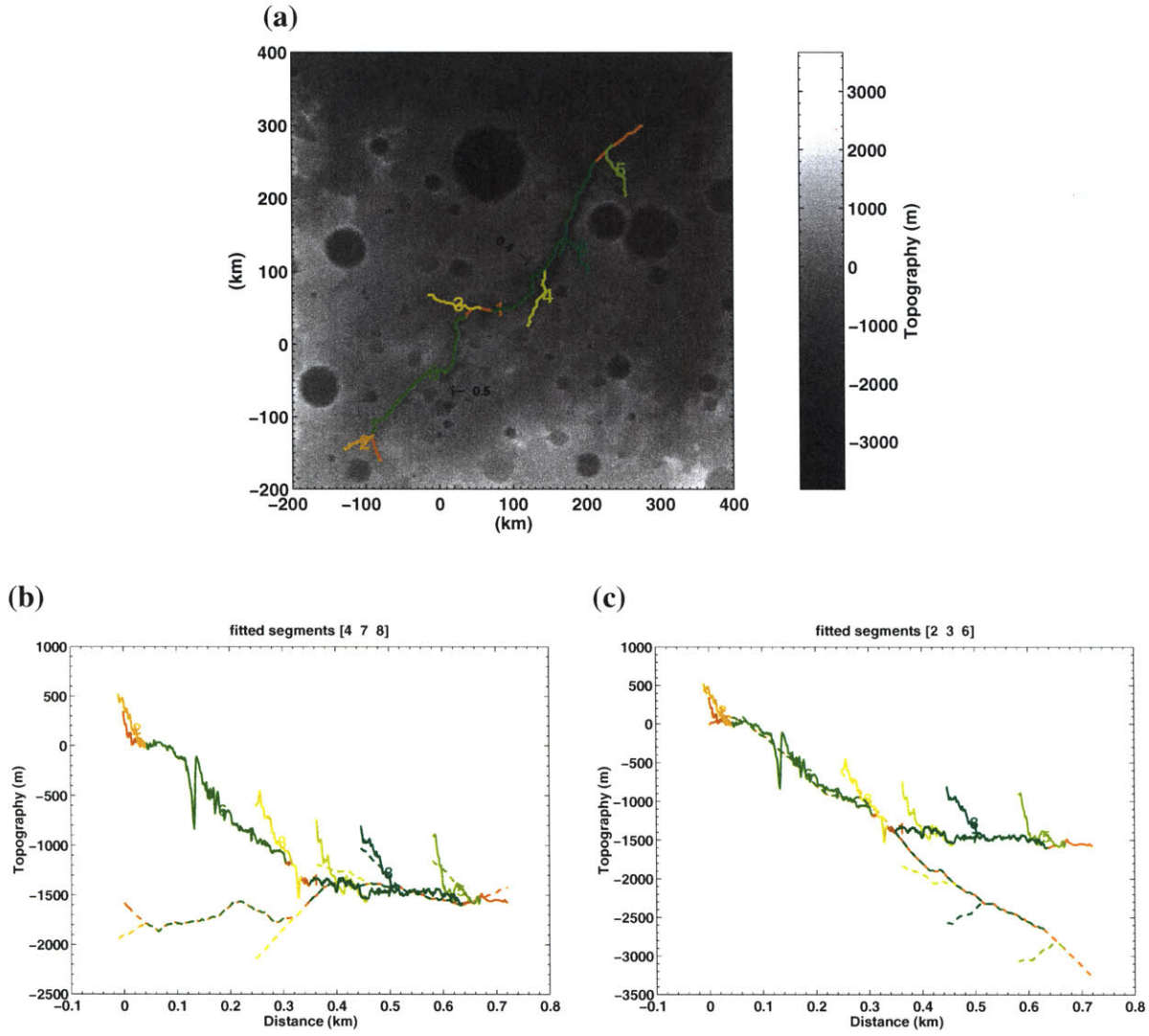

Figure 4-7: Al-Qahira Valles channel beds. (a) Topography in map view. (b) Channel segment topographic profiles (solid curve) and planar fits to segment subsets, evaluated at the channel locations (dashed curve)

analysis.

Another test case, carried out in a canyon system carved in the south wall of Valles Marineris, is shown in Figure 4-8. In this region there are a large number of canyons, traditionally interpreted to result from groundwater seepage and subsequent collapse [e.g. *Baker*, 1982]. The results indicate that a single plane can be fit to some subsets of the canyon floors, but no plane can account for all, or even a majority of the segments. The

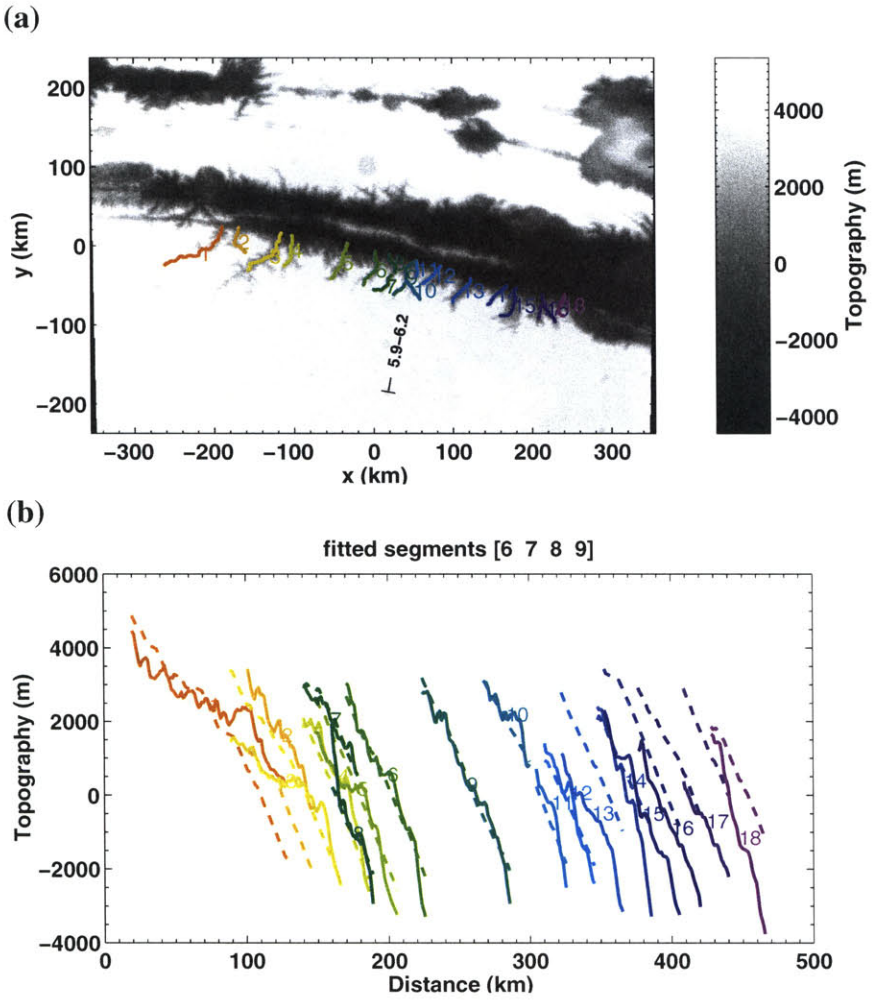

Figure 4-8: Valles Marineris channel beds. (a) Topography in map view. (b) Channel segment topographic profiles (solid curve) and planar fits to segment subsets, evaluated at the channel locations (dashed curve)

canyons on the opposite (north) wall of the valley are similar in morphology, and it is difficult to imagine any subsurface lithology that could be correspondingly deformed. Note that the canyons in this region are substantially shorter than in other examples, and hence any linearity or slope breaks are taken to be much less indicative of subsurface structure.

Acknowledgments

We acknowledge helpful discussions with Roger Phillips, Rebecca Williams, Robert Craddock, and Noah Snyder. This study was supported by the generous Kerr Fellowship, the Mars Global Surveyor Project, and by DOE Grant DE FG02-99ER 15004.

Chapter 5

Evidence for a Phase-Transition of Water on Mars

Abstract

The Mars Orbiter Camera on the Mars Global Surveyor spacecraft has returned images of numerous dark streaks that are the result of down-slope mass movement occurring under present-day Martian climatic conditions. We systematically analyzed over 23,000 high-resolution images and demonstrate that slope streaks occur exclusively in regions of low thermal inertia, steep slopes, and where daily peak temperatures exceed 275 K during the martian year. The northernmost streaks, which form in the coldest environment, form preferentially on warmer south-facing slopes. Repeat images of sites with slope streaks show changes only if surface temperatures exceeded the melting point of water during the time interval between the two images. Although unexpected on theoretical grounds, the simplest and most direct interpretation of these results is that at least small amounts of water are transiently present in low-latitude near-surface regions of Mars and undergo phase transitions at times of high insolation, triggering the observed avalanches.

5.1 Introduction

Preserved in the Martian geologic record are landforms reflecting an ancient wetter and perhaps warmer period. Geomorphic features such as dendritic valley networks and outflow channels have been interpreted as evidence of extensive fluvial activity in the early history of Mars [*Baker*, 2001; *Carr*, 1996]. Subsequent to this early period, the Martian surface may have been continuously very dry [*Baker*, 2001; *Sagan et al.*, 1973; *Squyres*, 1984], and present atmospheric conditions are such that water or ice on the surface is unstable [*Ingersoll*, 1970]. The discovery of small gullies in images obtained by the Mars Orbiter Camera (MOC) on board the Mars Global Surveyor (MGS) spacecraft [*Albee et al.*, 2001] has reopened the possibility of near-surface liquid water in the more recent past [*Malin and Edgett*, 2000a], perhaps in periods of high obliquity [*Costard et al.*, 2002; *Mellon et al.*, 2000]. While some gullies are geologically young, there is no direct evidence for their active formation on present-day Mars. In contrast, slopes streaks presently forming on the surface of Mars [*Malin and Edgett*, 2001; *Sullivan et al.*, 2001] provide insight into processes occurring under current climatic conditions. Here, we report new evidence that indicates a water phase transition is responsible for the generation of dark streaks currently forming between latitudes 18°S-37°N.

Dark slope streaks were first sighted in high-resolution Viking images and observed in greater detail by MGS [*Ferguson and Lucchitta*, 1984; *Morris*, 1982; *Sullivan et al.*, 2001]. They have characteristic morphology and form on slopes associated with features such as escarpments and crater walls (Figure 5-1). They generally extend over distances of 100's of meters to a few kilometers longitudinally, and typically have widths of $<$200 m (Figure 5-1). They are usually darker than their surrounding, but occasionally the albedo contrast is reversed (Figure 5-1c). Streak margins vary from extremely sharp with a boundary $<$ 1 m (limited by the best MOC image resolution), to more diffuse transitions. Some streaks branch or fan in the downhill direction. Slope streaks closely follow the local topography, and are generally considered to result from gravitationally-driven mass movement [*Sullivan et al.*, 2001].

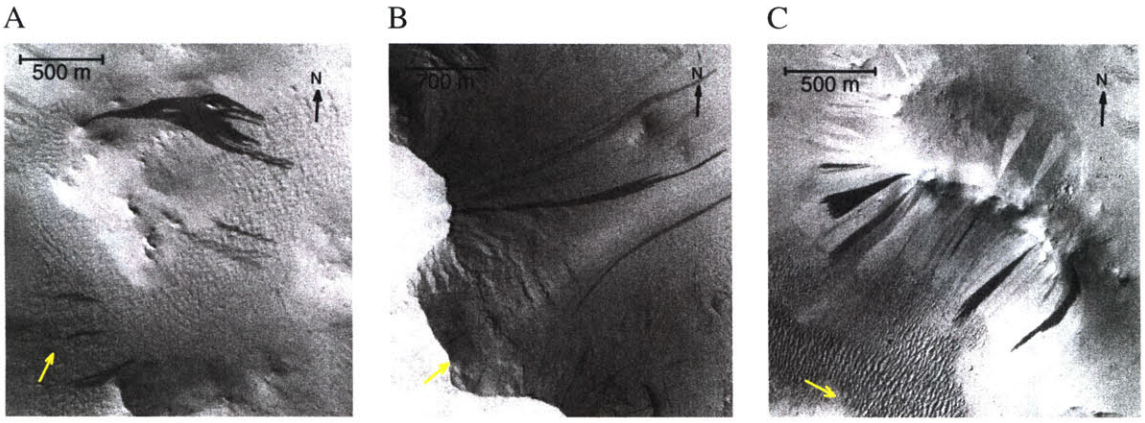

Figure 5-1: Examples of slope streaks in MOC narrow-angle images. Shown are subframes of images (A) M13-00834, (B) M08-06185, and (C) M20-00701. Arrows indicate north (black) and the direction of solar illumination (yellow). Note the strong influence of topography on the placement and orientation of streaks.

5.2 Geographic distribution

In order to study their properties and geographic distribution, we have systematically examined MOC images. Images were surveyed as follows. First, in a sample of 13000 MOC narrow-angle images (uniformly distributed over all latitudes) we identified 194 images with slope streaks, all in low-latitude regions. Having established that slope streaks occur exclusively in low-latitude regions, we then focused on all remaining narrow-angle images between 30°S–60°N obtained during the primary MGS mission. In total, approximately 23000 images were examined, of which 761 were unambiguously identified as containing slope streaks. The geographic distribution of images containing slope streaks, as well as the null-sample, are shown in Figure 5-2.

Streaks are grouped in three clusters, a feature best explained [*Ferguson and Lucchitta*, 1984; *Sullivan et al.*, 2001] by comparison to the distribution of thermal inertia shown in Figure 5-3. Thermal inertia, I, is defined as $\sqrt{k\rho c}$, where k is thermal conductivity, ρ the mass density, and c the specific heat capacity of the material. The typical thermal inertia where streaks occur is 80 J $\mathrm{m}^{-2}\mathrm{K}^{-1}\mathrm{s}^{-1/2}$and $\sim 95\%$ of slope streak images are from areas where I <130 J $\mathrm{m}^{-2}\mathrm{K}^{-1}\mathrm{s}^{-1/2}$. Thermal inertia is influenced by thermal conductivity,

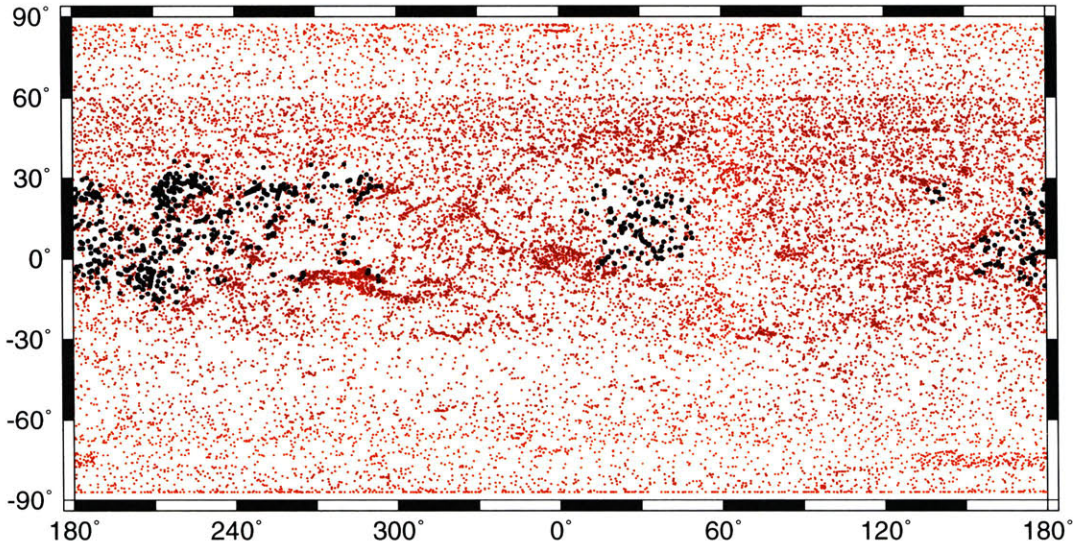

Figure 5-2: Geographic distribution of 761 images with slope streaks (black points) compared with the distribution of all 23000 images surveyed (red points).

which in turn depends on the particle size. Hence, low thermal inertia is characteristic of dust [*Christensen*, 1986; *Jakosky and Christensen*, 1986; *Zimbelman and Kieffer*, 1979] supporting the interpretation of slope streaks as dust avalanches.

The statistics of slope streaks we have compiled allow investigation of additional correlations. While no streaks are found in areas of high thermal inertial, Figure 5-3 shows that some areas of low I have no streaks. Notable examples are Amazonis Planitia (16°N 202°E) and plains surrounding the Tharsis Montes (5°N 250°E), where streaks are absent. An examination of the topography reveals that those areas are particularly smooth [*Aharonson et al.*, 2001]. Figure 5-4 shows the root-mean-square topographic slope (θ_r) computed from data collected by the Mars Orbiter Laser Altimeter (MOLA) [*Aharonson et al.*, 2001; *Smith et al.*, 2001b] on board MGS. The spacing of altimeter points along-track is about 300 m, comparable to the length the streaks, and RMS of point-to-point slopes was computed in a 35 km sliding window to obtain a map of surface roughness. The map shows that formation of streaks is restricted to rough terrain where root-mean-square slope values are greater than 0.9° . Smooth plains, typically associated with volcanic resurfacing, lack steep slopes and therefore slope streaks. The actual slopes on which streaks occur can be

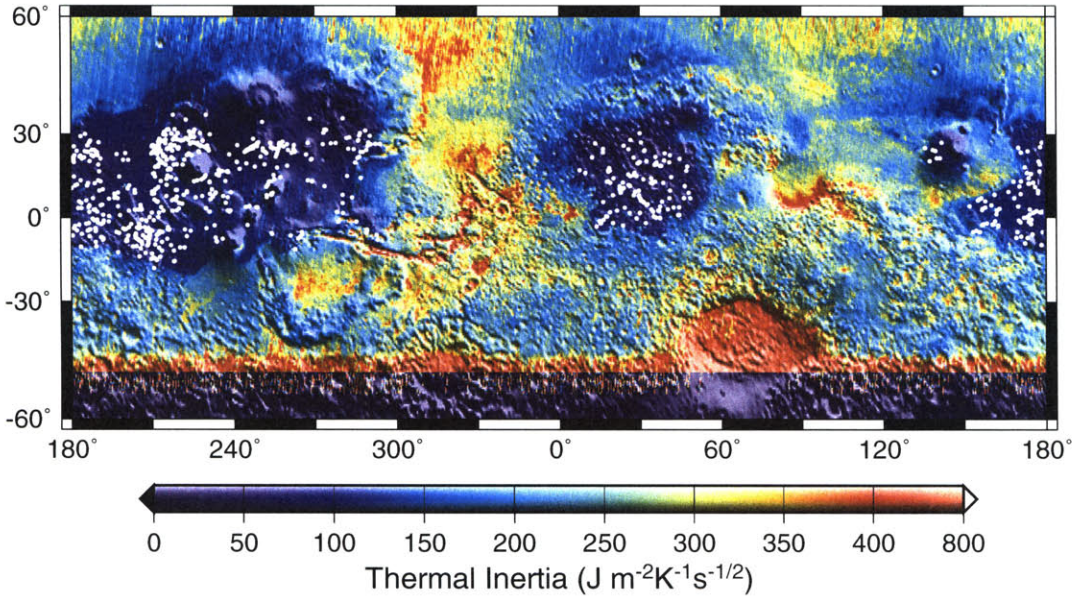

Figure 5-3: Thermal inertia map [*Mellon et al.*, 2000] superimposed on shaded relief. Locations of slope streaks are indicated by white dots. Streaks occur without exception in regions of low thermal inertia, thought to be covered by dust.

constrained by analysis of altimetric profiles. Gradients obtained from MOLA elevations for 16 sites where ground tracks intersect slopes with streaks are in the range of 16-38°, with a median of 22° (after correcting for the direction of the feature with respect to the ground track). Two examples are shown in Figure 5-5. While the slopes are not sufficient to distinguish among formation mechanisms, we note that dry avalanches are expected at the angle of maximum stability, while flows involving water can occur on more widely varying slopes. The cumulative distribution functions of the RMS slope and thermal inertia at slope streaks image locations are shown in Figure 5-6.

In Figure 5-7 we have combined the dual criteria of low thermal inertia (I<130 J $\mathrm{m}^{-2}\mathrm{K}^{-1}\mathrm{s}^{-1/2}$) and frequent steep slopes (θ_r <0.9°) into a mask. These values correspond to $\sim$ 95 percentile point of the distributions in Figure 5-6 , but the results are similar for other cutoffs, as demonstrated in Table 5.1. Within regions where both conditions are satisfied slope streams occur in roughly one of every five images, and are hence common, although they are rare on a global average. However, several large areas in the

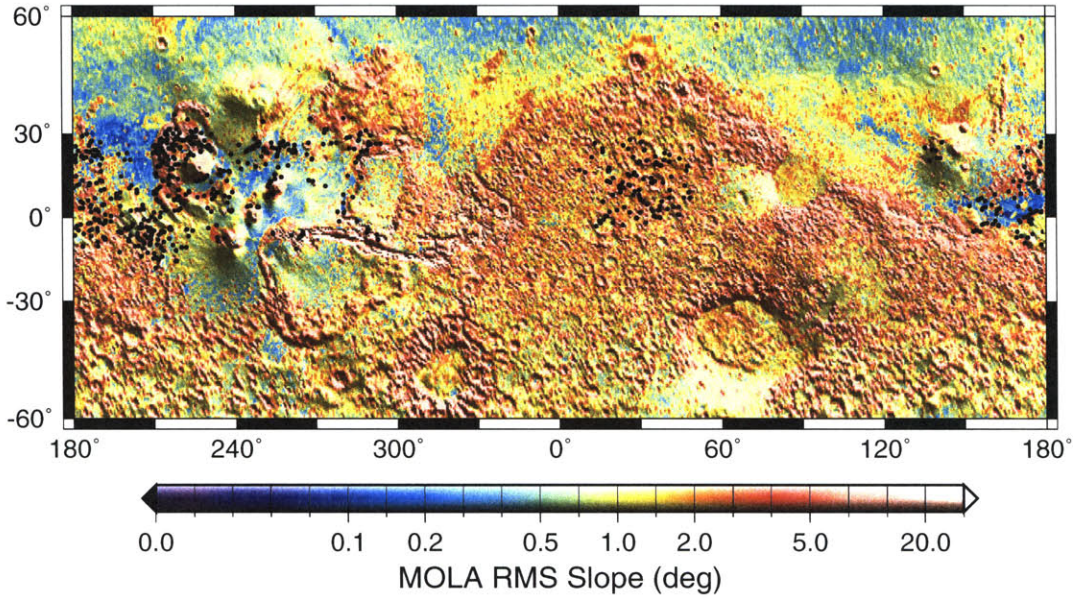

Figure 5-4: Map of root-mean-square (RMS) surface slope [*Aharonson et al.*, 2001] derived from MOLA elevations, superimposed on shaded relief. Slope streaks (black dots) are absent in particularly smooth terrain (RMS slope $<1^\circ$).

northern hemisphere are sufficiently high in dust abundance and rough terrains, but are devoid of streaks (within blue boxes on Figure 5-7). An additional control on the occurrence of slope streaks is therefore necessary.

Global coverage of temperature is available from the Thermal Emission Spectrometer

Condition	Percentile	Global Fraction	
		$> 275K$	$< 275K$
$I < 115$	90%	20%	<1%
$I < 130$	95%	19%	<1%
$I < 150$	97%	18%	<1%
$I < 165$	98%	18%	<1%
$I < 130$ & $\theta_r > 0.9^\circ$	90%	22%	<1%
$I < 150$ & $\theta_r > 0.6^\circ$	95%	19%	<1%

Table 5.1: Sensitivity to parameter thresholds. Fraction of images among those surveyed, that contain slope streaks. The percentiles are with respect to the 761 images containing slope streaks. The global fractions are with respect to all images within the masked region.

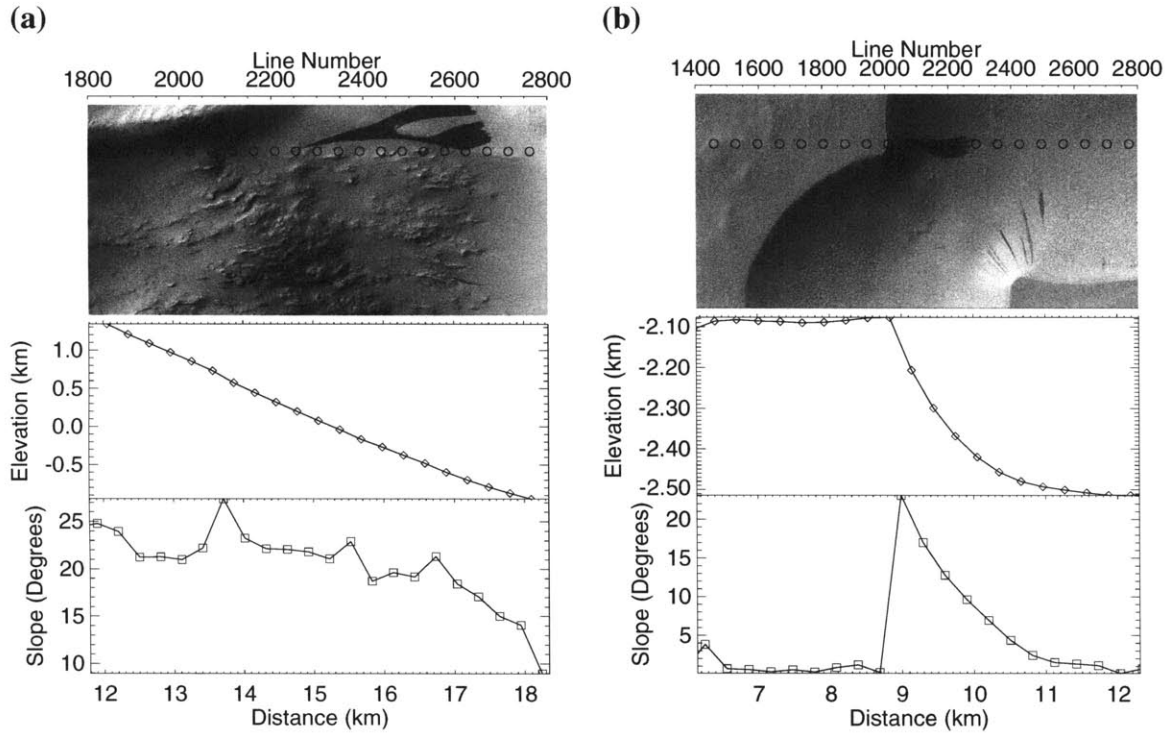

Figure 5-5: MOLA Profiles crossing slopes with dark streaks. The images shown are (a) M10-00662 and (b) M10-00967. Shown are the image data with MOLA shot locations superimposed, as well as the elevation and slope profiles.

(TES) on board MGS. Measurements by the Pathfinder lander [*Schofield et al.*, 1997] and model calculations [*Mellon et al.*, 2000] show that maximum temperatures occur in the early afternoon. Thus TES-based temperatures collected at local times between 12:50 pm to 3:00 pm provide a good estimate of the peak surface temperature. Figure 5-7 also shows contours of peak temperature derived from TES data collected between February 28, 1999 and April 1, 2001, spanning more than one Martian year. Surface temperatures measurements were obtained in single- and double- scan mode at a wavelength of 7 μm, away form the main atmospheric CO_2 absorption bands. After sorting afternoon temperatures into spatial and temporal bins, the 85th percentile temperature in each bin was computed, and the yearly maximum retained (The 75 percentile temperatures are systematically lower by about 0.5 K, but otherwise lead to the same results). Due to the eccentricity of the orbit, the southern hemisphere experiences higher peak temperatures in southern summer than

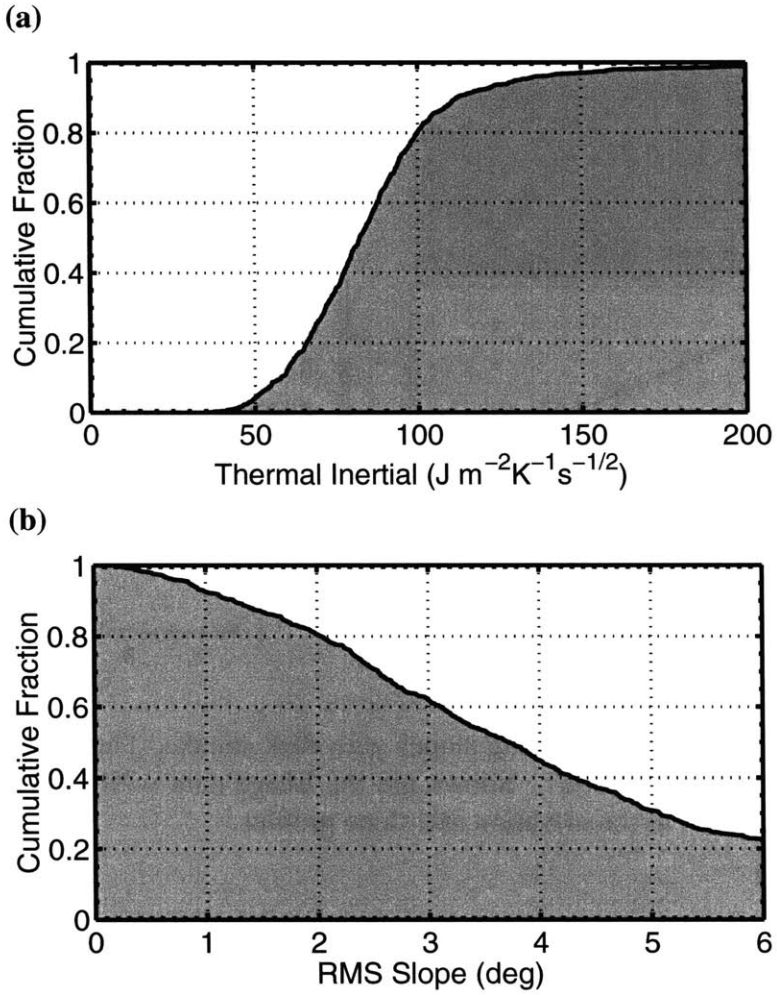

Figure 5-6: Cumulative histograms showing the fraction of images with slopes streaks occurring in areas of a given maximum thermal inertia (a), or minimum slope (b).

the northern hemisphere in northern summer [*Haberle et al.*, 2001]. Peak temperatures are sufficiently high to melt or sublimate water at all locations where slope streaks occur.

The areas highlighted in Figure 5-7 where streaks are conspicuously missing, are separated from the areas where streaks are found by the 275 K temperature contour. It is unlikely that this temperature contour near the melting point of water would coincide with the geographical streak boundary purely by chance. Combining the previous two criteria with a third in which maximum temperature $T_{\max} < 275$ K, eliminates the otherwise

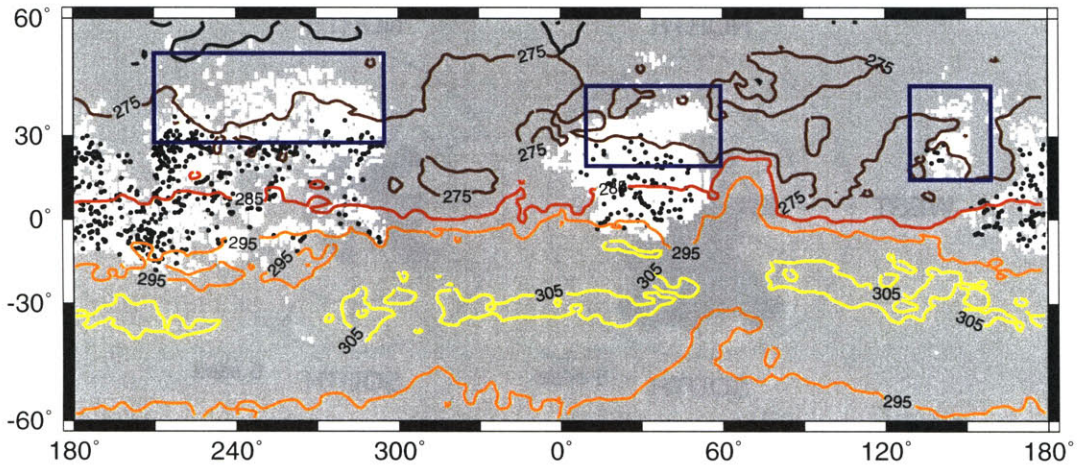

Figure 5-7: Map depicting conditions favorable to the formation of slope streaks. In the mask, white indicates terrain with thermal inertia I <130 J $\mathrm{m}^{-2}\mathrm{K}^{-1}\mathrm{s}^{-1/2}$ and terrain roughness θ_r >1° . Regions where either condition is violated are shown in gray. Contour lines show peak temperatures, and the location of slope streaks is indicated by black dots. As seen within the areas highlighted by blue boxes, an additional control of minimum peak temperature explains the lack of slope streaks.

unexplained streak-free regions in the north, and produces an excellent spatial correspondence between the combined mask and the actual locations of slope streaks (Figure 5-7). Table 5.1 shows that the temperature correlations are not sensitive to the precise choice of thresholds for thermal inertia and RMS slope.

An additional line of evidence indicating that streak formation is controlled by temperature is available. Assuming that streak azimuths reflect the direction of steepest downhill gradient, a histogram of azimuths in the regions of lowest peak temperatures (latitudes north of 30°N) reveals that streaks form preferentially on equator (south) facing slopes (Figure 5-8A). A sample of streaks near the equator, where peak temperatures are higher and more symmetric, shows no such bias (Figure 5-8B).

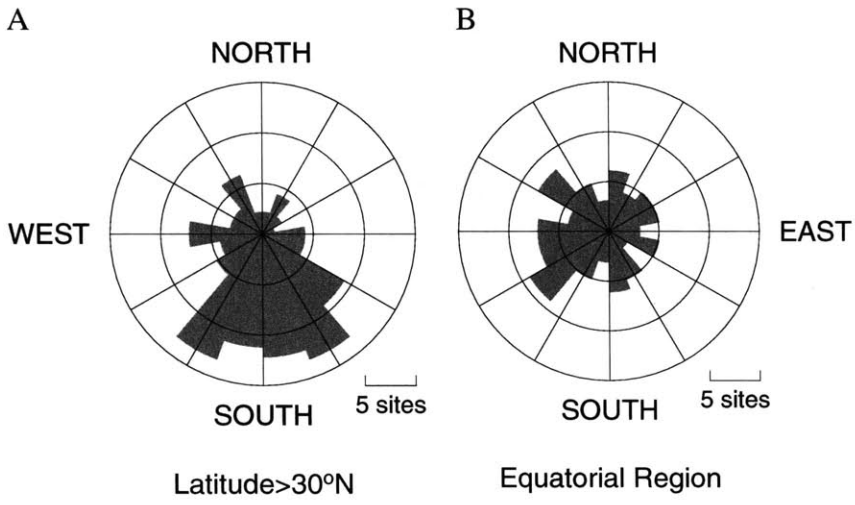

Figure 5-8: Histograms of streak orientations plotted as a rose diagram. Slope streaks north of 30°N (A) occur preferentially on south-facing slopes, a bias not seen in equatorial sites (B)

5.3 Formation Times

Several sites with slope streaks were imaged more than once, allowing the investigation of the timing of streak formation. We have found 39 such pairs of images. Most show no clear changes in the streaks. However, in addition to two previously reported image pairs with new slope streaks [*Palermo et al.*, 2001; *Sullivan et al.*, 2001], we have identified five new image pairs where changes are unambiguous. Of these seven pairs, three are approximately one Martian year apart and hence provide no constraints on the season during which the changes occurred. The remaining four are presented in Figure 5-9. Each panel shows TES surface temperatures at the location of the images as a function of the areocentric solar longitude, L_s (defined such that $L_s = 0°$ at vernal equinox, and $L_s = 90°$ at northern summer solstice). To smooth the scatter in the temperature data, a line is drawn along the 85th percentile points in L_s bins of 30° . In all cases, the time interval during which new streaks formed includes periods warmer than 273 K. This temporal correlation further supports the hypothesis that a water phase transition is responsible for triggering the formation of streaks. The 39 reimaged pairs show roughly 450 slope streaks in the overlap region of first and second images. About 20 streaks are newly-formed. Hence, in this sample, on

the order of 5% of streaks formed within a year. Comparison of streaks in Viking images with Mars Global Surveyor images suggests that streaks fade on a decadal time scale, in agreement with the inverse formation rate. If fading and formation balance, the population of slope streaks is in a statistical steady state with the current Martian environment.

5.4 Water phase transitions

The geographic (Figure 5-7), azimuthal (Figure 5-8) and temporal (Figure 5-9) correlations, provide evidence for a connection between slope streaks and a surface temperature near the triple point of of water, suggesting the formation of streaks involves a water phase transition. For example, liquid water would be most efficient in the lubrication of avalanches. Alternatively, mass movement may be triggered by sublimation at the solid-gas transition, or conversely, by dessication of an initially moist, cohesive surface. We now explore the viability of these mechanisms in the Martian environment.

The amplitude of diurnal surface temperature oscillations decays exponentially with the skin depth $\delta = (I/\rho c)\sqrt{P/\pi}$, where P is the oscillation period, ρ the density, and c the heat capacity. For typical Martian regolith (ρ=1500 $\mathrm{kg/m^3}$ and c=630 $\mathrm{JK^{-1}kg^{-1}}$, ref. [*Mellon et al.*, 2000]) in regions of low thermal inertia (I=80 $\mathrm{J\ m^{-2}K^{-1}s^{-1/2}}$), the diurnal skin depth is about 1 cm. Model calculations [*Haberle and Jakosky*, 1991] show that temperatures above melting can occur typically in the upper 0.5 cm of the regolith. Streaks do not appear to penetrate deeply, since pre-existing surface textures are often preserved beneath the feature (e.g. Figure 5-1A) and no accumulated debris is visible at the termination of slope streaks [*Sullivan et al.*, 2001]. The small penetration depth of melting temperatures is consistent with the interpretation that the mass flow is restricted to a thin layer.

Surface pressures on Mars are close to the triple point of water (6.1 mbar), with substantial variations due to elevation. Diurnal and seasonal fluctuations are roughly 1-3 mbar [*Smith and Zuber*, 1998]. Figure 5-10 shows the phase diagram of water (solid line) [*Weast*,

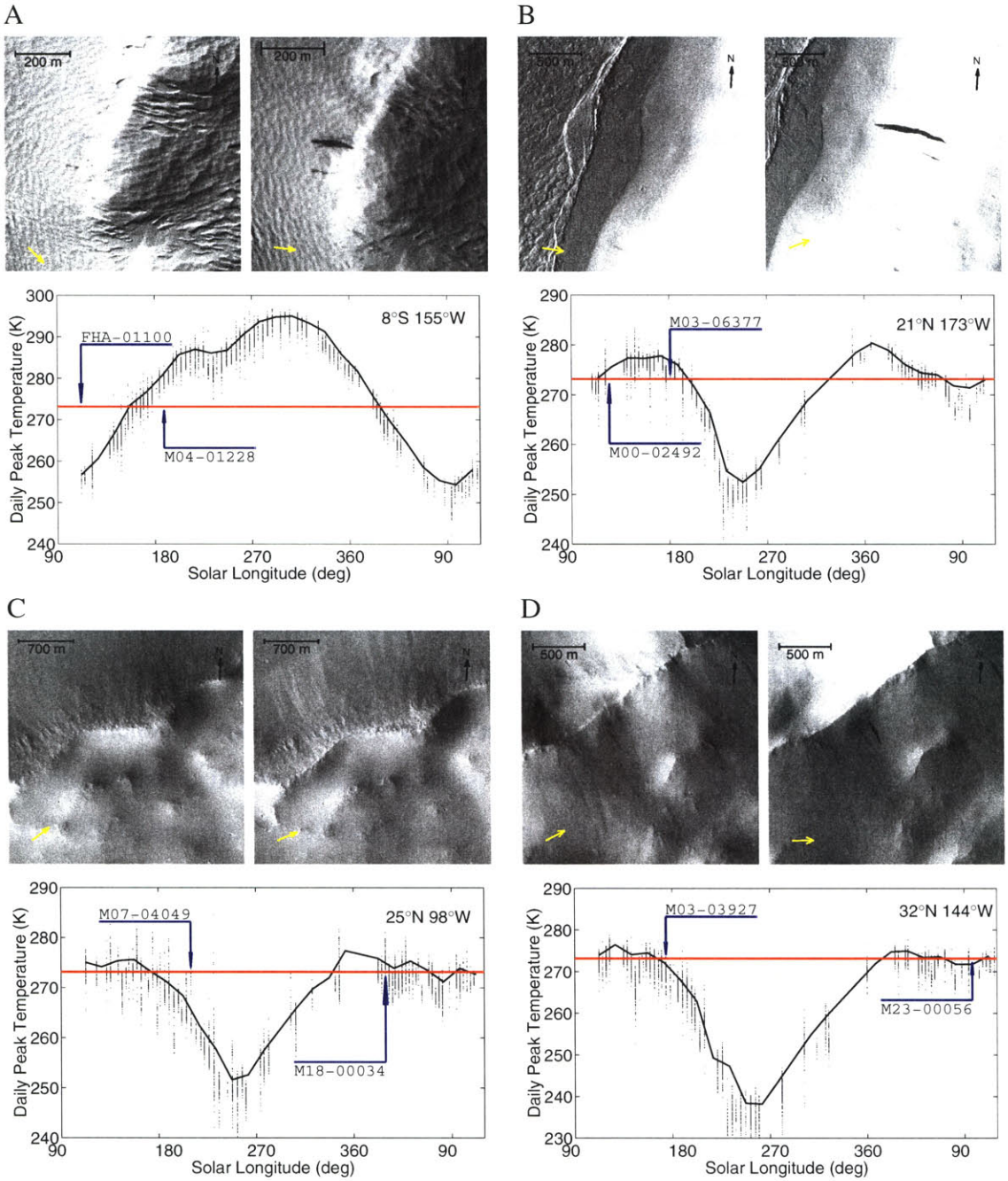

Figure 5-9: Daily peak temperatures from TES (small dots) as a function of solar longitude L_s for four slope streak sites that have been imaged twice and show newly-formed streaks in the later image. The black line indicates the 85th percentile temperatures. Blue arrows indicate the L_s at which the images were taken. In all four cases, streak formation occurred during a period in which surface temperatures exceed 273 K (red line). Arrows in the images indicate north (black) and the direction of solar illumination (yellow). Pair (c) shows the creation of bright rather than dark streaks.

1981], as well as the average pressure and peak temperature at the locations of the streaks (black points). Local pressures were estimated using an exponentially decaying atmosphere, with a pressure of 6 mbar at the geoid, and a scale height of 10 km. The primary atmospheric constituent is CO_2, and in a well mixed atmosphere the vanishingly small partial pressure of H_2O would imply that any water ice accumulated during the cold nights should sublimate rapidly as temperatures increase. In addition, evaporative cooling slows the warming of ice [*Ingersoll*, 1970]. However, in a static atmosphere, sublimation rates are controlled by diffusion of water molecules out of a saturated vapor layer in contact with the ice. If the diffusion rate is sufficiently slow, the partial pressure of H_2O can build up to the level of the surrounding total pressure [*Hecht*, 2001]. While the points in Figure 5-10 mostly lie in the vapor region at peak seasonal temperature, it is important to note that in situ temperatures will cross the phase boundaries over diurnal cycles. Also plotted are conditions at those locations that are favorable for streak formation based on thermal inertia and roughness criteria alone (white points in Figure 5-10, corresponding to the white areas in Figure 5-7). The success of the mask in predicting streak locations is again seen, as is the importance of temperature as an additional control.

The population of streaks extends up to 11 km elevation ($\sim$1 scale-height above the geoid) and hence to low atmospheric pressures of $\sim$2-3 mbar. If the phase transition responsible for triggering slope streaks is the sublimation of ice, and if it was sensitive to ambient atmospheric conditions, then the streak population should extend down to the sublimation curve ($\sim$263 K at the lowest pressures). As plotted, it is evident that not all points will encounter the solid-liquid boundary. However, we suggest a number of factors that may impact that.

Dissolved salts would shift the triple point to a lower pressure (and temperature), expanding the region of stability of the liquid phase (represented by arrow 1 in Figure 5-10). Per percent (by weight) of dissolved salt, the freezing point depression is approximately 0.6°C for NaCl, 0.2°C for K_2SO_4, and 0.3°C for $MgSO_4$ [*Weast*, 1981]. Roughly 15% of NaCl would be required to lower the triple point pressure such that ice at all elevations

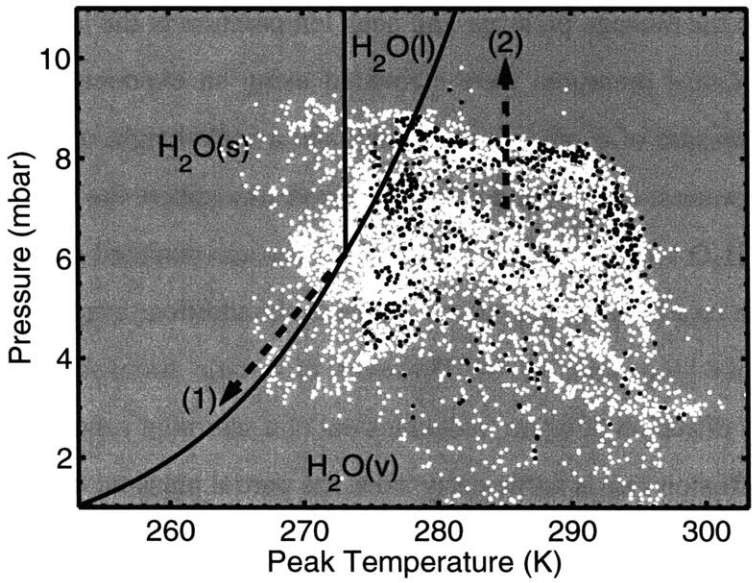

Figure 5-10: Phase diagram of pure water. Black points represent locations of slope streaks, using peak temperature estimates from TES, and elevations converted to to local atmospheric pressures. The phase boundaries are crossed during diurnal cycles. White points are sampled from the white areas in Figure 5-7, where $I < 130$ J m^{-2}K^{-1}s$^{-1/2}$, and $\theta_r > 0.9$. The dashed arrows represent two scenarios discussed in the text.

where slope streaks occur would undergo a phase transition to liquid water during a diurnal cycle. The reduced melting point temperature in comparison with the peak temperature can be accounted for if melting is required to take place in a thicker layer. Salinity also reduces evaporative cooling [*Ingersoll*, 1970], allowing ice to warm more rapidly.

Alternatively, it is possible that the relevant pressure for the phase transition is not the ambient atmospheric pressure, but the elevated pressure within grains, pores or at grain boundaries (represented by arrow 2 in Figure 5-10). The latter can be significantly enhanced due to a phenomenon known as premelting [*Dash et al.*, 1995]. It is well known that ice is covered by a thin quasi-liquid layer well below the freezing point. The surface tension of this liquid layer can increase the internal pressure relative to ambient atmospheric pressures on Mars. Estimates for dust particle sizes range up to 40 μm [*Christensen*, 1986], which could lead to sufficient curvature effects to substantially elevate local pressures.

The suggestion that surficial H_2O may be present at low-latitudes is a surprise in light

of well accepted theoretical calculations demonstrating the residence time of any pure H_2O on the surface is short, and its long term stability doubtful [*Farmer and Doms*, 1979; *Ingersoll*, 1970]. However, H_2O can exist temporarily, over time spans that strongly depend on local conditions. For example, burial by overlying dust (perhaps catastrophically, after a dust storm) was suggested by *Jakosky* [1985] to prolong the stability of near-surface ice. *Paige* [1992] suggests ground ice can accumulate seasonally through exchange with the atmosphere, especially in regions of low thermal inertia, and if underlain with a deeper reservoir of ice. Factors such as salinity, burial, local pressure and atmospheric mixing effects, prolong ice stability [*Carr*, 1996; *Haberle et al.*, 2001; *Hecht*, 2001; *Ingersoll*, 1970; *Paige*, 1992], and may protect the reservoir until the slope streak event. Finally, since the correlations presented indicate a water phase transition, but do not prefer a direction for that transition, it is conceivable that indeed water is present for only short times. In this scenario dust particles stick to moist, cohesive slopes, on which they would otherwise be gravitationally unstable. Dust could thus collect over diurnal temperature cycles, until at some critical thickness, when the mixture loses its water and hence its cohesive strength, the collapse is triggered.

5.5 Summary

A systematic analysis of various data sets yields significant spatial and temporal correlations of slope streaks with peak temperatures above the triple point of water. This geologic evidence of a phase transition implies the presence of near-surface water at low latitudes on present-day Mars. The observational evidence does not require the total volume of water undergoing melting or sublimation to be large, or the time over which the liquid phase exists to be long. Indeed, since areas with slope streaks typically have a thermal inertia of only 80 J $\mathrm{m}^{-2}\mathrm{K}^{-1}\mathrm{s}^{-1/2}$ while water ice has a high thermal conductivity and, hence, in bulk form, a high thermal inertia of $\sim$2000 J $\mathrm{m}^{-2}\mathrm{K}^{-1}\mathrm{s}^{-1/2}$, it is unlikely that large fractions of ice are permanently present in the top few centimeters of the surface. If that were the case,

large seasonal changes in the volume fraction of near-surface ice would be detectable in thermal inertia variations. Direct detection of any ice in the upper decimeters of the surface is a primary objective of the ongoing Gamma Ray Spectrometer experiment on board the Mars Odyssey spacecraft.

Acknowledgments

This chapter is being prepared for publication in collaboration with Norbert Schorghofer and Samar Khatiwala.

We thank Michael Allison, Ingrid Kohl, Thomas Lörting, Mark Richardson, Daniel Rothman, Wesley Watters-Farfan, Kelin Whipple, and Maria Zuber for valuable discussions, and Michael Mellon for supplying the thermal inertia data in digital form. The authors acknowledge the use of Mars Orbiter Camera images processed by Malin Space Science Systems that are available at http://www.msss.com/moc_gallery/. SK was supported by a William Z. Leavitt Post-Doctoral Fellowship. This research was supported by DOE grant DE FG02-99ER 15004 to D. Rothman and a Mars Global Surveyor Project grant to M. Zuber.

Chapter 6

Time-Dependent Topography and Seasonal Cycles

Abstract

Observations by the Mars Orbiter Laser Altimeter have been used to detect subtle changes of the polar surface height during the course of seasonal cycles that correlate with the expected pattern of CO_2 deposition and sublimation. Using altimetric crossover residuals from the Mars Orbiter Laser Altimeter, we show that while zonally averaged data captures the global behavior of CO_2 exchange, there is a strong dependence of the pattern on longitude. At the highest latitudes the surface height change is 1.5–2 m peak-to-peak, and decreases equatorward. Decomposition of the signal into harmonics in time shows that the annual component is strongly correlated with the residual south polar cap deposits, and weakly with the north polar cap. In the north, the second harmonic (semi-annual) component correlates with the location of the ice deposits. The phases of the annual cycles are in agreement with thermal observations of the timing of the annual disappearance of CO_2 frost from the surface at the high latitudes. At lower latitudes, frost sublimation predates the mean depositional minima. These results represent the first global-scale measurements on the distribution of condensed surficial CO_2 mass as a function of latitude and longitude, that can be used to constrain models of the Martian climate system and volatile cycles.

6.1 Introduction

The dynamic role of volatiles on the surface of Mars has been a subject of longstanding interest. In the pre-Viking era, much of the debate was necessarily addressed by theoretical considerations. A particularly influential treatment was put forth by *Leighton and Murray* [1966], in which a simple model relying on solar energy balance was employed, and led to the conclusion that the most prominent volatile exchanging with the atmosphere over seasonal cycles is carbon dioxide. Their model suggested that due to this exchange, atmospheric CO_2 partial pressure is regulated by polar ice. While current thinking attributes a larger role to H_2O ice than the occasional thin polar coating this model predicted [*Jakosky and Haberle*, 1992], the essential CO_2 cycle described by *Leighton and Murray* appears to be largely correct.

There are a number of observations indicating seasonal exchange of surface volatiles with the atmosphere on Mars. The growth and retreat of polar CO_2 frost is visible from Earth-based telescopes [*Martin et al.*, 1992] and from spacecraft in Mars orbit, both at visible wavelengths and in thermal IR properties of the surface [*Briggs et al.*, 1977; *James*, 1979; *Kieffer*, 1979]. Measurements made by Viking's Mars Atmospheric Water Detector (MAWD) experiment were sensitive to atmospheric H_2O vapor abundance [*Farmer et al.*, 1977; *Jakosky and Farmer*, 1982]. The Viking landers detected surface condensates and their transient nature [*Jones et al.*, 1979]. Recent data collected by the Mars Global Surveyor [*Albee et al.*, 2001] affords the opportunity not only to detect the lateral distribution of volatiles [*Kieffer et al.*, 2000; *Titus et al.*, 2001], but also to constrain the variable volumes of the reservoirs. *Smith et al.* [2001a] showed that the zonal pattern of deposition and sublimation of CO_2 can be determined by examining averages of a large number of topographic measurements collected by the Mars Orbiter Laser Altimeter (MOLA) [*Smith et al.*, 1999b, 2001b; *Zuber et al.*, 1992].

The primary constituent of the Martian atmosphere is CO_2 , and up to 30% has been estimated to exchange with the surface during a seasonal cycle [*James et al.*, 1992]. The cycle was first characterized quantitatively in a local sense during the Viking mission by

measuring seasonal variations of atmospheric pressure at both landing sites [*Hess et al.*, 1979, 1980; *Leovy*, 1985; *Zurek et al.*, 1992]. A seasonal pressure change was also observed at the Pathfinder landing site over a small fraction (12%) of a Martian year [*Schofield et al.*, 1997]. No successful landing-site measurements have been made so far in the southern highlands. Radiative balance calculations [*Bachman and Keegan*, 1992; *Paige and Ingersoll*, 1985; *Paige and Wood*, 1992] and general circulation models (GCMs) [*Haberle et al.*, 1993] constrained by Viking lander pressure data estimate the mass of the condensed deposits to be consistent with a maximum amplitude at the poles of about 1 m of solid CO_2 ice.

While both the north and south seasonal frost is composed of CO_2, temperatures during summer seasons indicate that the residual cap in the north is composed of H_2O [*Kieffer et al.*, 1976], while the much smaller residual ice cover in the south is made of CO_2 [*Kieffer*, 1979]. The south pole layered terrain may be underlain with H_2O ice, an idea supported by atmospheric water vapor seen by Viking in some years [*Jakosky and Haberle*, 1990] and further bolstered by recent laboratory measurements on the rheology of CO_2 [*Nye et al.*, 2000], indicating that a CO_2 ice cap would flow away on geologically short timescales. The differences between the northern and southern frost deposition and sublimation (and perhaps ultimately, cap composition) is traditionally attributed to at least two factors [*Thomas et al.*, 1992]. The Viking orbiter result that 75 ± 12 g/cm^2 of CO_2 were deposited in the north, and 110 ± 7 g/cm^2 in the south [*Paige and Ingersoll*, 1985] during one year of observations, is attributed to the longer winter season in the south. The relatively darker albedo of north polar cap may be due to higher dust concentration [*Paige and Ingersoll*, 1985] that also leads to enhanced sublimation rates. Recently, *Richardson and Wilson* [2002] suggested that a topographically forced asymmetry in the Hadley cell circulation controls global transport of H_2O. In their calculation, the topography creates a preference for the active formation of polar layered deposits in the north, independent of the perihelion timing.

While optical and spectral techniques are sensitive to the spatial distribution of surface

frost, they often lack sensitivity in several important aspects. Until the work of *Smith et al.* [2001a] the volumes of condensed surface material have been unconstrained, as were rates of deposition and sublimation. In order to address these questions, and to quantitatively characterize the spatial and temporal pattern of volatile exchange, we elaborate on a technique first employed by *Smith et al.* [2001a]. In their first approach, reference surfaces were fit to all measurements in narrow latitude annuli, and the time dependent variations about those mean surfaces were examined. In their second approach, height measurements from pairs of tracks that cross on the surface were interpolated and differenced, forming a set of crossover residuals. These residuals were then examined as a function of time and latitude. The initial studies averaged over longitude to maximize signal and minimize noise in order to isolate the miniscule expected signal. In this follow-up study we now attempt to extract the elevation change pattern also as a function of longitude, and have focused on the crossover approach.

6.2 Data Quality

The accurate recovery of changes in elevation depends upon the quality of the range measurements from which the residuals are derived. We therefore briefly review the error estimates affecting the crossover measurements. Estimations of surface height are prone to error, introduced both by the range measurement itself, as well as from imperfect knowledge of the position and orientation of the spacecraft.

The range from the spacecraft to surface is obtained from the round-trip time-of-flight of a laser pulse arriving back at the MOLA detector, and hence includes timing errors and errors due to the receiver's response. The precision of the timing measurement is limited by the clock accuracy of $\sim$2.5 ns, corresponding to 37.5 cm, but suffers from systematic drifts in the clock frequency. These daily variations are estimated, and shown to be less than 1 part in 10^8 [*Neumann et al.*, 2001; *Smith et al.*, 2001b]. Modeling of the instrument [*Abshire et al.*, 2000; *Gardner*, 1992] allows a correction to be applied, accounting for

variability in shape and strength of return pulses that affects the instrument's triggering time. This correction, referred to as "range walk", is typically 1–3 m in amplitude, and has an uncertainty of approximately 30 cm [*Neumann et al.*, 2001].

In addition to the range to surface, knowledge of the position and orientation of the spacecraft relative to Mars' center of mass is necessary to obtain planetary radius estimates. This is accomplished by tracking of the radio signal emitted by the spacecraft, and accounting for its maneuvers and accelerations [*Lemoine et al.*, 2001]. The solution of this large inverse problem results in a determination of the planetary gravitational field, as well as a set of "orbits", *i.e.,* the time dependent position and attitude of the spacecraft. The gravity field is expressed in terms of the height of an equipotential surface (the "areoid"), and subtracted from radius measurements, giving the topographic height.

In the final step of the processing the elevation measurements themselves are used to improve the orbital solutions. The elevations of locations where a pair of ground-tracks of measurements intersect (Figure 6-1), are interpolated and differenced to form a set of "crossover residuals". These residuals may include both real surface height changes, as well as systematic errors in the orbital position.

To reduce the effect of systematic error sources the set of raw crossover residuals was adjusted by deriving a correction for each track such that the $\sim$ 9 million residuals equatorward of 57° latitude or occurring within 15 days of each other were minimized, since no change is expected for these measurements. This minimization is carried out by least-squares fitting of orbital adjustment parameters, using three-dimensional, smooth (polynomial), functions of time [*Neumann et al.*, 2001; *Rowlands et al.*, 1999; *Smith et al.*, 2001b]. In the preferred model, the fitting problem is over-constrained, as there are roughly 200 times more measurements than fitted parameters. Applying these adjustments, and recomputing the crossover residuals, reduces their root-mean-squre from the initial value 8.303 m, down to 1.817 m [*Neumann et al.*, 2001]. The correction was then applied to all tracks and the entire set of $\sim$ 66 million residuals recomputed. To minimize random errors, residuals resulting from less reliable measurements were excluded. These include measurements

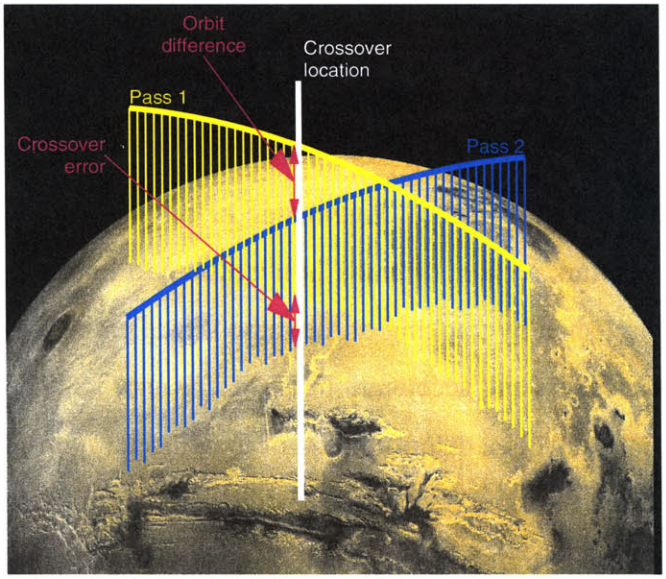

Figure 6-1: Crossover errors are determined by interpolation of crossing ground tracks. Removal of systematic orbit differences results in the change in surface height.

obtained on slopes greater than 10%, off-nadir observations, and residuals > 10 m [*Smith et al.*, 2001a]. This criterion eliminates data collected in latitudes 87° to the poles, as the orbit of Mars Global Surveyor has an inclination of 92.7° and these polar observations are off-nadir and characterized by significant range walk.

6.3 Time-Dependent Topography

The intersections of MOLA ground-tracks (*i.e.* crossovers, as represented in Figure 6-1) provide a useful means of determining changes in the topography occurring during the time interval between the measurements. The amplitude of any seasonal change is expected to be small in comparison to the local topography, and reducing systematic and random errors as described above is crucial. By averaging a large number of observations it is possible to isolate temporal height changes at the $\sim$10 cm level [*Smith et al.*, 2001a]. In order to treat the data uniformly when forming averages, each crossover residual is counted twice: once with the time tag of the later track, and again, with the time tag of the earlier track and an opposite sign.

The global redistribution of CO_2 on the surface can be seen by averaging the crossover residuals δz over all longitudes, as a function of latitude and season. Assuming that the error source is Gaussian, the formal error associated with this mean, σ_m, is given by

$$\sigma_m = \frac{\sigma}{\sqrt{N}} \tag{6.1}$$

where σ is the standard deviation of the data and N is the number of measurements. Figure 6-2 shows the seasonal dependence of deposition for a selected high-latitude $0.5°$ annulus, centered on 86.25°N and 86.25°S, as a function of solar longitude L_s (defined such that $L_s = 0°$ at vernal equinox, and $L_s = 90°$ at northern summer solstice). In close agreement with *Smith et al.* [2001a], the fluctuations are seen to be maximum in both hemispheres during their respective late winters, near $L_s = 335°$ in the north, and $L_s = 155°$ in the south, both with a value of approximately 1.2 m above the average. The phase (and magnitude) of this signal is consistent with global circulation models of Mars' climate (as well as with intuition). The magnitude of σ_m is small, typically less than 1 cm due to the large number of measurements used in forming the means. However, this formal error may be deceptive because in practice, unmodeled systematic errors may not be negligible.

A surprising aspect of the plot is seen in the increased "off-season" accumulation, near $L_s = 225°$ in the north, and approximately after $L_s = 40°$ of the second mapping year in the south. During these times, an unexpected enhancement in deposition occurs at high latitudes, which decays again before the onset of winter. *Smith et al.* [2001a] suggest that in the north the decay may be related to the warming of the atmosphere by regional dust storms observed near $L_s = 240°$. A detailed explanation of these local peaks will depend on an accurate description of the fluctuations. The fact that the signals are robust, namely that they are present in both crossover and profile analyses of the MOLA data [*Smith et al.*, 2001a], suggests that they are a consequence of meteorological phenomena that are not explained by the classical models of CO_2 deposition on Mars. However, we do not dismiss the possibility that some aspects of the signal are spurious and derive from unknown aspects

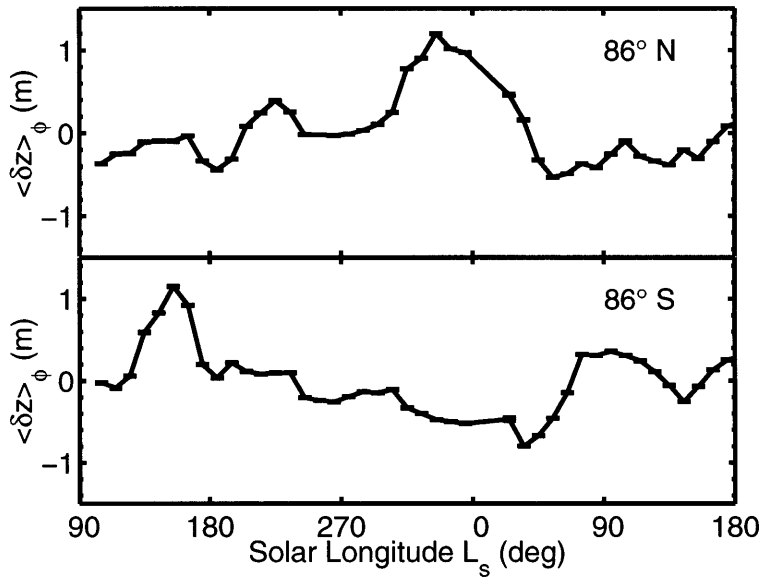

Figure 6-2: Average accumulation as a function of the seasonal parameter L_s, averaged over longitude in the annulus between 86-86.5° latitude.

of the response of the MOLA receiver. Significant analysis of the impulse response of the MOLA receiver has been performed [*Abshire et al.*, 2000; *Neumann et al.*, 2001; *Smith et al.*, 2001b] and the appropriate corrections have been applied to the data included in the present analysis, but efforts to better understand the response of the MOLA receiver, especially to changes in surface reflectivity, are ongoing [*Neumann et al.*, 2002].

Crossover residuals were sorted into spatial bin in latitude-longitude. Since MGS is in an approximately polar orbit (with an inclination of 92.7°), the number of elevation measurements in each bin is approximately uniform. However, since the number of crossovers increases as the square of the number of orbits, regular grids have cells with more crossovers near the pole, improving the statistical quality of high-latitude measurements with respect to low-latitudes.

In each spatial bin, we sorted the data in time (L_s), and apply a nonlinear least-squares fit (using the Levenberg-Marquardt method, implemented by *Press et al.* [1992]), to a func-

tion of the form

$$\delta z(L_s) = \sum_{n=1}^{n_{\max}} -A_n \cos(nL_s - D_n). \tag{6.2}$$

Initially we examine the first two terms, corresponding to the seasonal $n = 1$ and semi-annual $n = 2$ variations. The coefficients A_n are the amplitudes, and D_n are the phases of the variations' minima. If, for example, the accumulation was minimum on the last day of summer, the phase A_1 would be 180° in the north and 0° in the south.

Figures 6-3 and 6-4 show a summary of the north and south polar data. The maps shown in the left column correspond to (a) the annual term amplitude A_1, (b) phase D_1, and (c) the number of crossovers in each cell N. Panel (d) shows a simplified geologic map [*Tanaka and Scott*, 1987] of the region, and (e) is the topography superimposed on shaded relief.

In the north, the amplitude of the first harmonic A_1 is seen to increase with latitude, and while there may be a weak correlation, there is no abrupt change as the polar cap boundary is encountered. Locally, the amplitude can be as high as 1 m (2 m peak-to-peak), but more typically it is 0.4-0.6 m on the cap. In areas on the dune-covered Olympia Planitia (82°N,166°E), where sand and dust transport may be important, the amplitude is ~0.8 m. The phase of the first harmonic D_1 ~135° remains constant on the ice cap, and is only slightly more variable off the cap. This consistency in space is taken as an indication of the robustness of the fit. In the region between 70-80°N and 180-270°E the amplitude is reduced, and as expected, the phase is poorly constrained.

In the south, the amplitude A_1 is strongly correlated with the residual cap (unit Api). Detailed modeling is required in order to determine the cause of this strong correlation, but one likely possibility is that the enhanced accumulation is related to the higher albedo on that unit. The boundary of the layered terrain does not appear to have an obvious signature in the amplitude pattern. The phase of the first harmonic in the high southern latitudes is D_1 ~355°. A relatively static area is again seen in longitudes 180-270°E.

For both the north and south maps, we have more confidence in the amplitude measurement when the phase is consistent for nearby areas. When the phase is "noisy", the

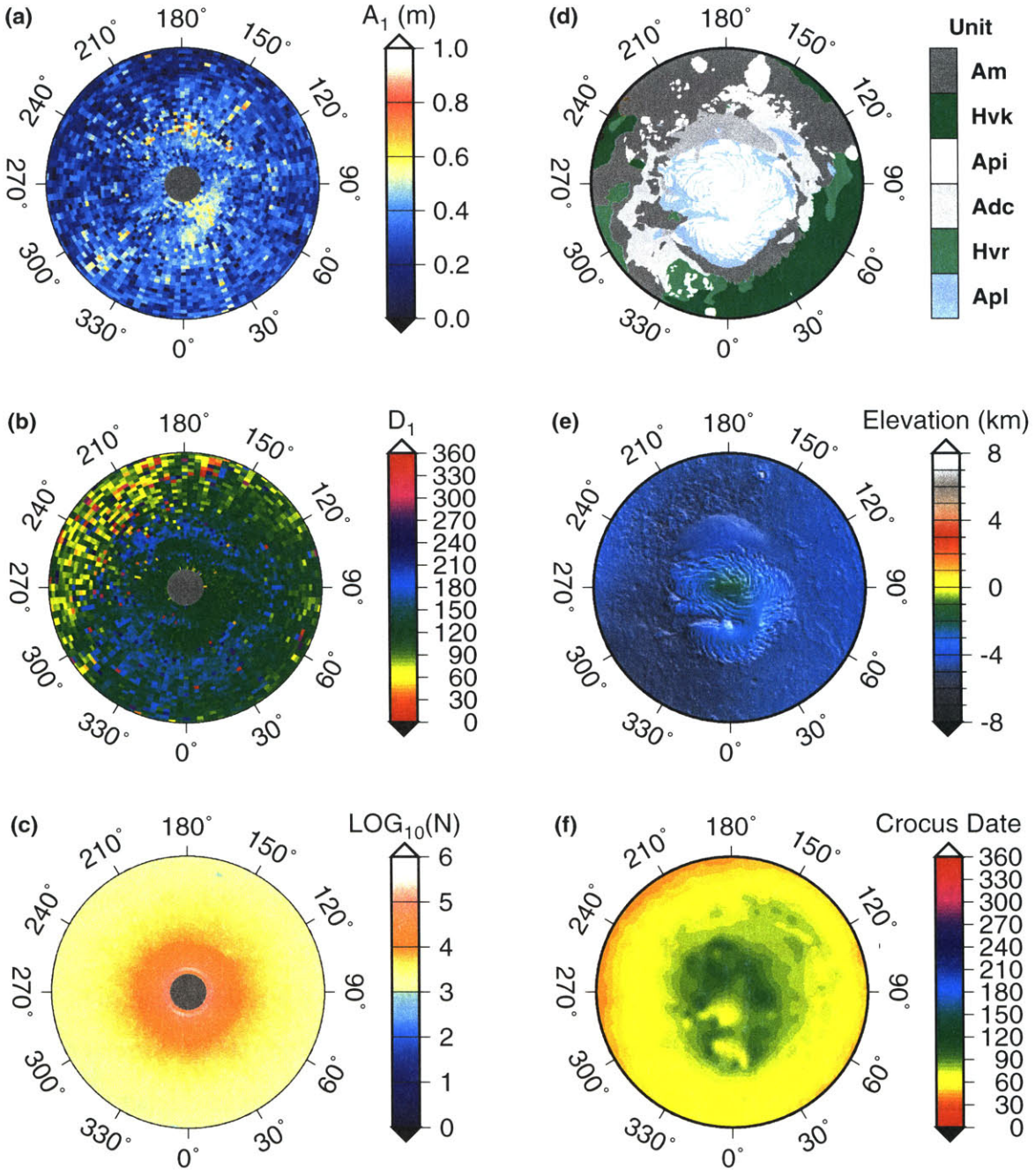

Figure 6-3: North Pole. Panels correspond to maps of (left column) annual sinusoid amplitude, phase, the number of crossovers used, (right column) geology, topography, and crocus date.

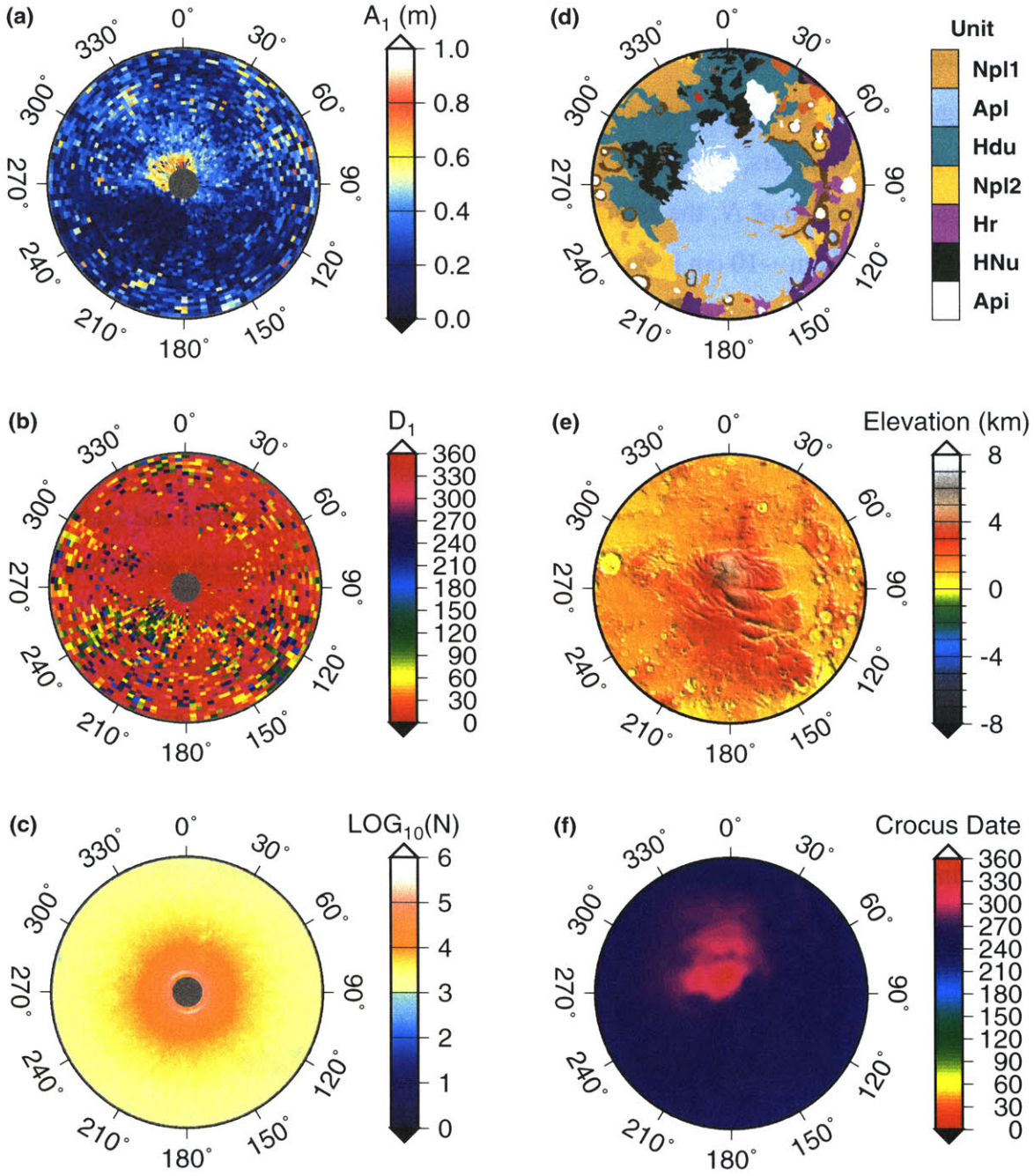

Figure 6-4: South Pole. Panels correspond to maps of (left column) annual sinusoid amplitude, phase, the number of crossovers used, (right column) geology, topography, and crocus date.

amplitude measurement is suspect. Furthermore, as indicated by N, the highest latitude bins have ~ 3 orders of magnitude more crossovers than the ones at 70° , and are therefore statistically better defined.

Figures 6-5, 6-6 and 6-7 show detailed maps for the north, south and equatorial regions of the fitted parameters, as well as their respective formal error estimates. As expected from the distribution of N, the estimates improve near the poles, so that the amplitude of the error drops from $\sim$10 cm in equatorial regions to < 2 cm near the pole, and the phase changes from being unconstrained in latitudes equatorward of 65°, to having an error of $< 3°$ near the poles.

In the north, while the annual term is only weakly correlated with the cap deposits, the semi-annual term (especially the phase D_2) is highly correlated with the topography and geology. The close relationship between this "off-season" component and features on the surface suggests that this dynamical behavior is robust and may be observed from year to year. There are a number of possible causes that could play a role in explaining this relationship, and they include effects of elevation, albedo, and exposure to solar insolation. In the south, the semi-annual term is more variable and the surface geology appears to be less important. The equatorial region shows no consistent phase and a very noisy amplitude distribution. Figure 6-7 shows the transition to greater amplitude and more consistent phase with increasing latitude. Polewards of 65° latitude in both hemispheres, the variability of D_1 drops dramatically.

6.4 Comparison with Thermal Crocus Date

As shown, the redistribution of CO_2 on the surface can be decomposed into harmonics in time, and the phases of these harmonics examined. At present, elevation measurements offer the best observational constraints on the volumes of volatiles involved in the exchange. However, spectral observations can be used as an independent approach to describe the temporal retreat of surficial CO_2, by examination of the surface temperature. Most re-

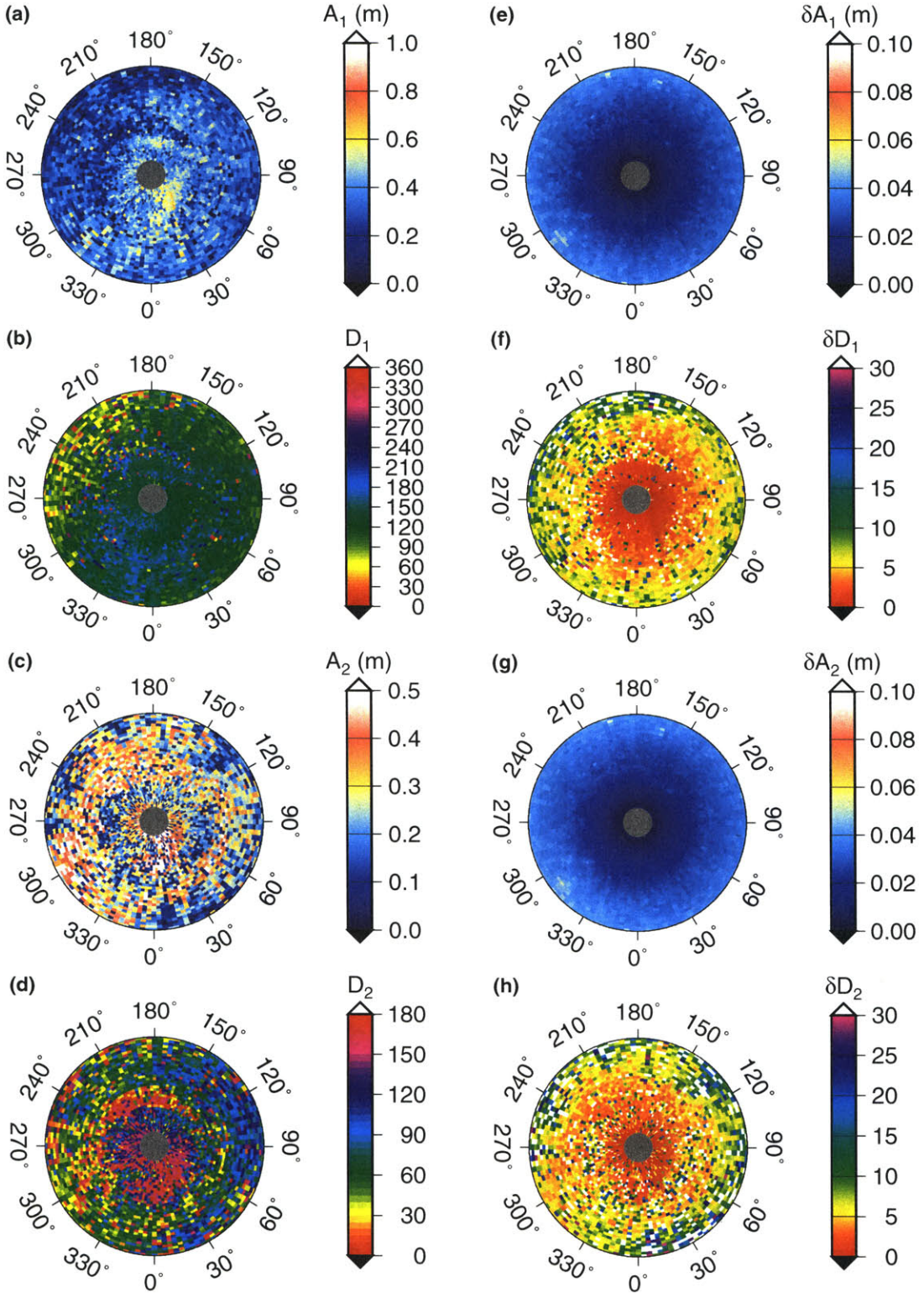

Figure 6-5: North Pole. Panels correspond to maps of (left column) amplitude and phase of the annual, and semi-annual topography change, as well as (right column) the 1-σ error estimate in each quantity.

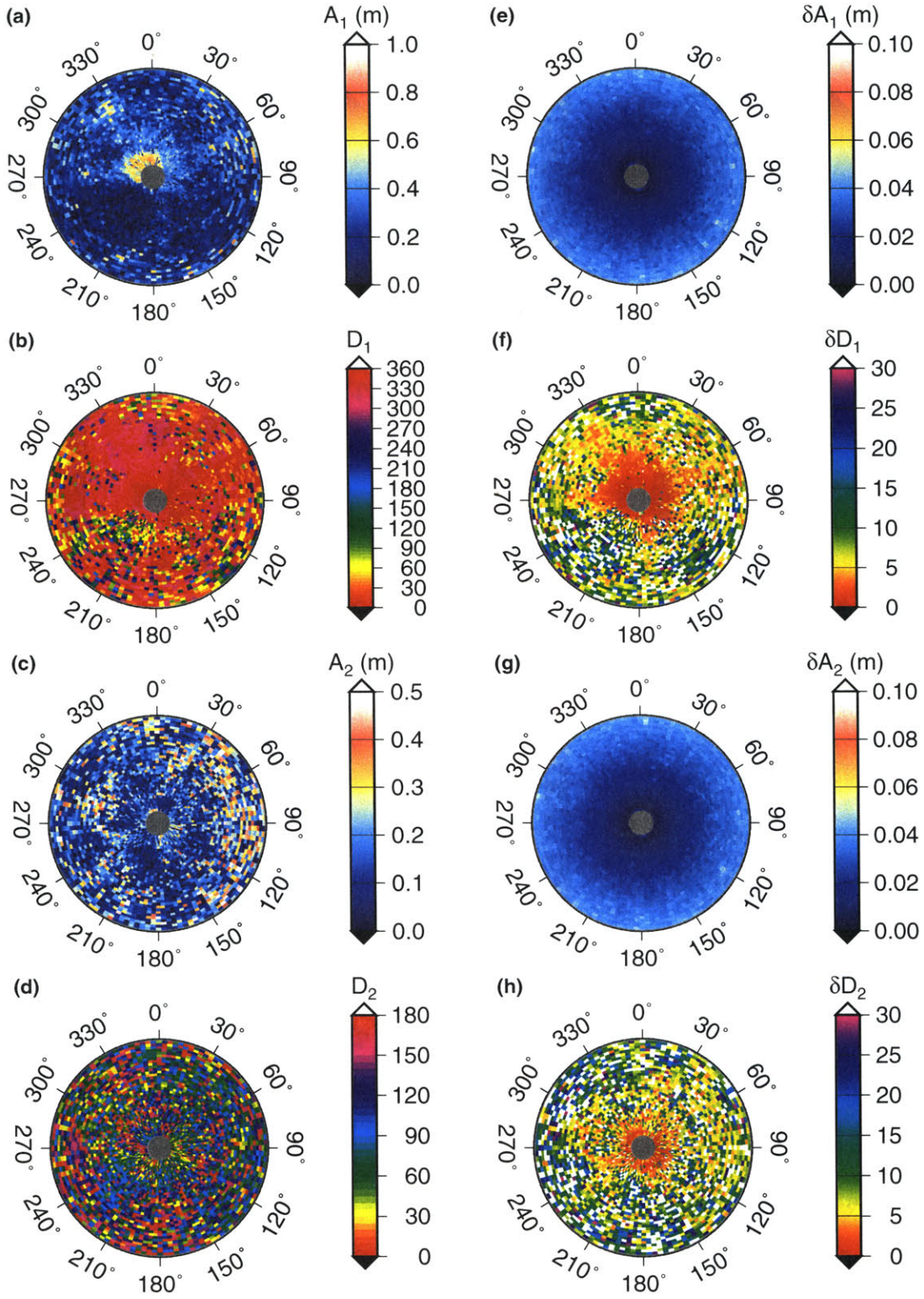

Figure 6-6: South Pole. Panels correspond to maps of (left column) amplitude and phase of the annual, and semi-annual topography change, as well as (right column) the 1-σ error estimate in each quantity.

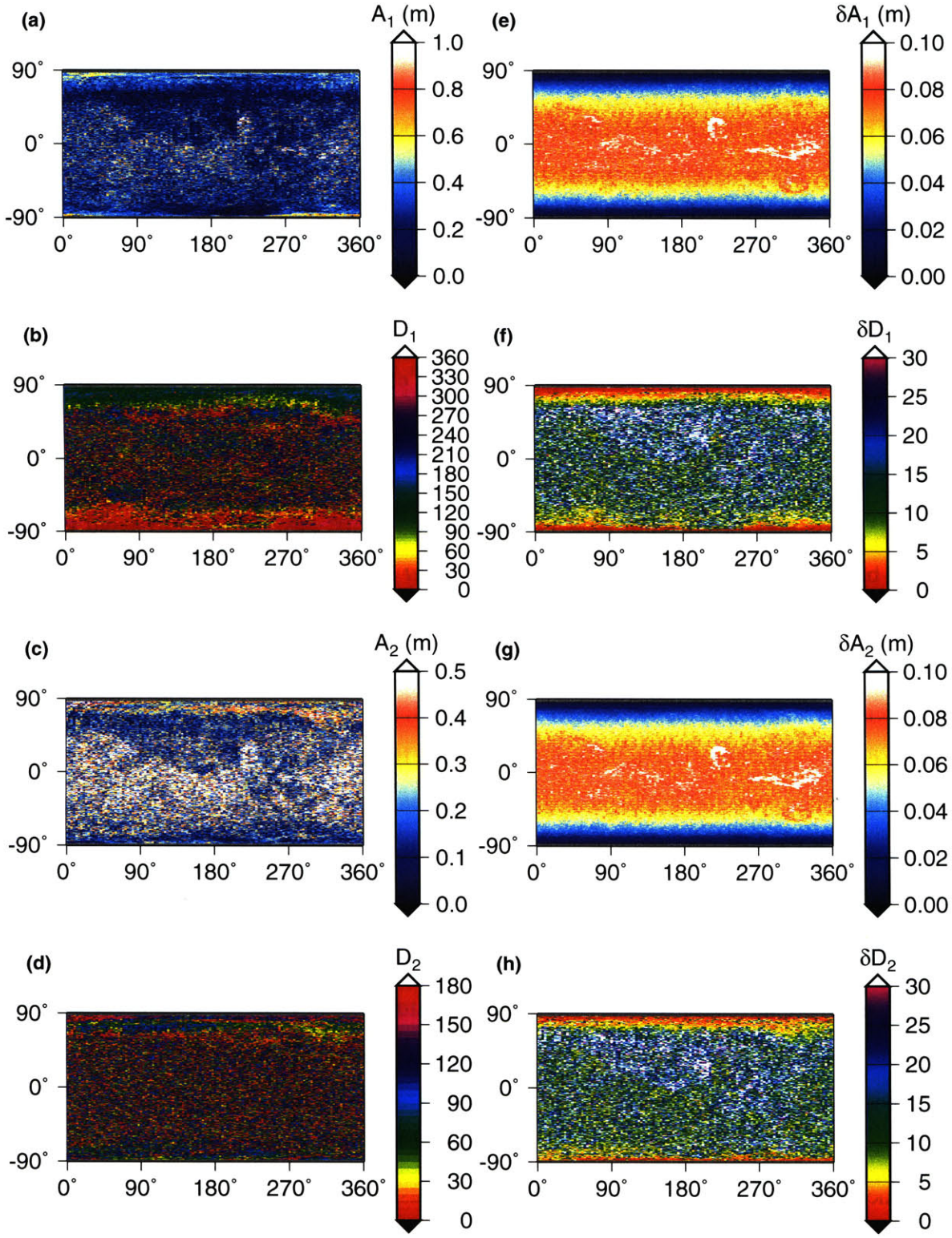

Figure 6-7: Equatorial Region. Panels correspond to maps of (left column) amplitude and phase of the annual, and semi-annual topography change, as well as (right column) the 1-σ error estimate in each quantity.

cently, this has been an important function of the Thermal Emission Spectrometer (TES) on board Mars Global Surveyor.

TES consists of three instruments: a thermal bolometer, a solar reflectance spectrometer, and a Michelson interferometer [*Christensen et al.*, 1992]. During normal operations, the spectrometer collects high resolution spectral radiance data in the wavelength range from 6.25–40 μm. The radiance can be related to the emission temperature T using Planck's black-body formula. As a function of inverse wavelength $\nu = 1/\lambda$,

$$R(\nu) = \frac{2h\nu^3c^2}{e^{h\nu c/kT} - 1}, \tag{6.3}$$

where Boltzman's constant $k = 1.3805 \times 10^{-23}$ J/K, Planck's constant $h = 6.626 \times 10^{-34}$ J·sec, and the speed of light is $c = 2.99793 \times 10^8$ m/s. In order to avoid absorption bands in the atmosphere, we follow *Kieffer et al.* [2000], and use the 30 μm band to define the temperature T_{30}. This temperature is sensitive to the warming of the surface that occurs when CO_2 sublimates away; while CO_2 is present, surface temperatures are buffered at $T_{30} = 148$ K, while after it has completely sublimated the surface warms to a new equilibrium temperature, typically more than 10 degrees higher. We divide the surface into a regular grid, and use an arc-tangent function to fit the temperature increase in each cell, with the form

$$T_{30}(L_s) = T_0 + \frac{\Delta T}{\pi} \arctan\left(\frac{L_s - C}{\varphi}\right) \tag{6.4}$$

where L_s is the season, T_0 is the brightness temperature at the date C (in units of L_s), and ΔT and φ are the characteristic time and temperature increase for the transition from CO_2 frost to soil. As defined in *Kieffer et al.* [2000], C corresponds to the date at which Cap Recession Observations indicate CO_2 has Ultimately Sublimated (CROCUS), and is thus termed the "crocus date". Those authors point out the coincidence that crocuses are some of the first flowers that can be seen just after the last snow-melt in early spring.

Maps of crocus date, as defined above, are shown in Figures 6-3 and 6-4 (panel f). The north polar maps show that the crocus date C occurs at a similar time or earlier than the

first phase D_1. The retreat of the frost covered area is seen to occur relatively uniformly, at a rate of approximately 3-3.5° of L_s per one degree of latitude. The crocus date approaches the value of $\sim$ 95° near the pole, similar to D_1. In contrast, the behavior at the southern polar cap is again seen to be less symmetric in longitude. In areas where CO_2 ice is present throughout the year, the fits often fail to converge and C is meaningless. Off the cap, C changes from $\sim$ 240° to 300°, again earlier than is seen in D_1. The difference between C and D_1 at both poles, is likely a consequence of the fact that the deposition is not truly sinusoidal. The crocus date is sensitive to the precise day that the ice disappeared, while D_1 measures the phase of the cycle as a whole. While the value of C is consistently smaller than D_1, the fluctuations in the two quantities are not independent in space.

6.5 Comparison with Global Circulation Models

The voluminous data collected by MGS has for the first time tilted the balance of Mars climate investigations, making them more similar to Earth's in the sense that our direct observational power exceeds that of our predictive modeling. While global circulation models have low spatial resolution both laterally and vertically, the optical, thermal, and altimetric observations have high precision and resolution. Nonetheless, models are clearly the key to understanding the controlling physics of the observational phenomena. Here, we focus on the Ames General Circulation Model (GCM), described in detail by *Pollack et al.* [1990], and reported on by *Smith et al.* [1999a]. This model features a resolution of 7.5° in latitude, 9° in longitude, and 0.5–5 km vertically. The model employs conservation equations of mass, energy, and momentum, as well as a hydrostatic condition, radiative transport associated with dust loading, and a CO_2 ideal gas law.

The seasonal cycle of CO_2 is simulated by the GCM are summarized in Figure 2 of *Smith et al.* [1999a], repeated here for convenience in Figure 6-8. Surface CO_2 ice is predicted to exchange with the atmosphere in the north and south with an opposite annual phase. The locations of the maxima peaks are better defined than the broader minima, and

they occur near $L_s = 0°$ in the north and $L_s = 150°$ in the south. However, these peaks are shifted with respect to a mean sinusoidal component of the variation, which more closely agree with the observed phase D_1 in both hemispheres.

The amplitudes of the surface exchange in the north and south do not balance, resulting in a net semi-annual oscillation in the total surface mass (balanced by atmospheric storage). In the model, the amplitude of the oscillation in the south is $\sim 65\%$ greater than in the north, owing to the longer cold season.

The amount of material implicated in the exchange will perturb the gravitational field of Mars in a time-dependent manner. This change should then observable by tracking the orbiting spacecraft and modeling its accelerations. Analysis by *Smith et al.* [2001a] suggests that the estimates from the GCM, and the gravitational and topographic perturbations are generally consistent with each other if the density of the material is 910 ± 230 kg/m^3. Since this density is smaller than that of solid CO_2 (ρ=1589 kg/m^3), it indicates void spaces may be prevalent in the CO_2 ice matrix.

The primary driving term in global circulation models (and the one used here) is the solar insolation flux. This term varies with an annual period and hence, the predictions of accumulation rates follow. One, or several of, a number of factors that are either ignored or approximated in models may be responsible for the observed "off-season" accumulation. Local shadowing by topography may allow enhanced accumulation. In polar regions such shadowing can be either nearly permanent, or merely sufficiently long in duration to alter the expected deposition/sublimation balance. Squalls, or local storms, that are not typically modeled in GCM calculations, may also contribute to the signal, but constraining their relative roles awaits further advances in meso-scale modeling [e.g., *Joshi et al.*, 1996; *Toigo and Richardson*, in press]

As was seen in Figure 6-8, during the northern and southern cold seasons ($L_s = 0°$ and $360°$) surface deposition of CO_2 is maximum and atmospheric CO_2 is minimum. During autumn and spring, ($L_s = 90°$ and $270°$) the situation is reversed, and the atmospheric CO_2 partial pressure is highest. Although the temperatures are on average higher, the higher

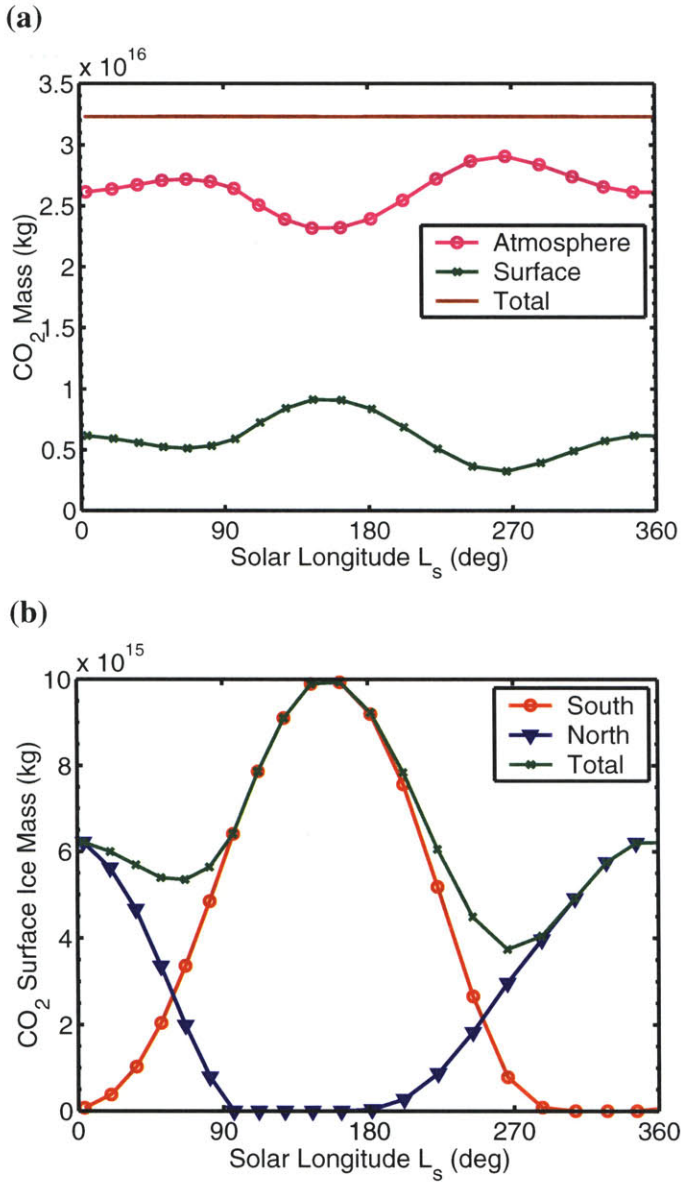

Figure 6-8: GCM predictions of CO_2 variations as reported by *Smith et al.* [1999a]. In Panel (a) the exchange between the surface and atmosphere is shown. In panel (b) the total surface ice mass is divided into the northern and southern components.

partial pressure could facilitate atmospheric condensation, and might account for the "off season" accumulation component. Additionally, variations in abundance of nucleation sites in the form of dust particles, may drive this component.

While the details of atmospheric conditions are not within the scope of this work, the pressure and temperature column are critical in controlling deposition and sublimation styles and rates. Figure 6-9 shows atmospheric pressure and temperature conditions as measured by TES (M. D. Smith, personal communication), as well as vapor pressure curves for CO_2 [*TRCVP*] and H_2O [*Haar et al.*, 1984; *Wagner et al.*, 1994]. The curves correspond to 0° and 60-85° in 5° latitude increments, and are averaged over all longitudes. The atmosphere follows the CO_2 vapor curve in the north during northern winter and in the south during southern winter. This is interpreted to be an equilibrium of the vapor with a condensed phase. Perhaps less obvious is the inversion seen in northern and southern spring, in which temperature is seen to decrease slightly with altitude, and the possibility of low altitude condensation is suggested.

6.6 Summary

Our results demonstrate that the large number of MOLA elevation measurements can be effectively corrected, averaged and fitted, to yield sensitive measurements of the changes in polar surface height as a function of both latitude and longitude over the Martian seasonal cycles. Accumulation is expected and observed to be maximum in late winter, and at high latitudes at both hemispheres. More perplexing deposition/sublimation episodes occur during warmer seasons as well, also visible in the zonally-averaged crossover analysis. In order to resolve the dependence of the pattern on longitude and time, a harmonic decomposition of the signal was carried out locally. The annual component of the signal is strongly correlated with the residual south polar cap deposits, and weakly with the north polar cap. In the north, the second harmonic (semi-annual) component correlates with the location of the ice deposits. The phases of the annual cycles are in agreement with thermal

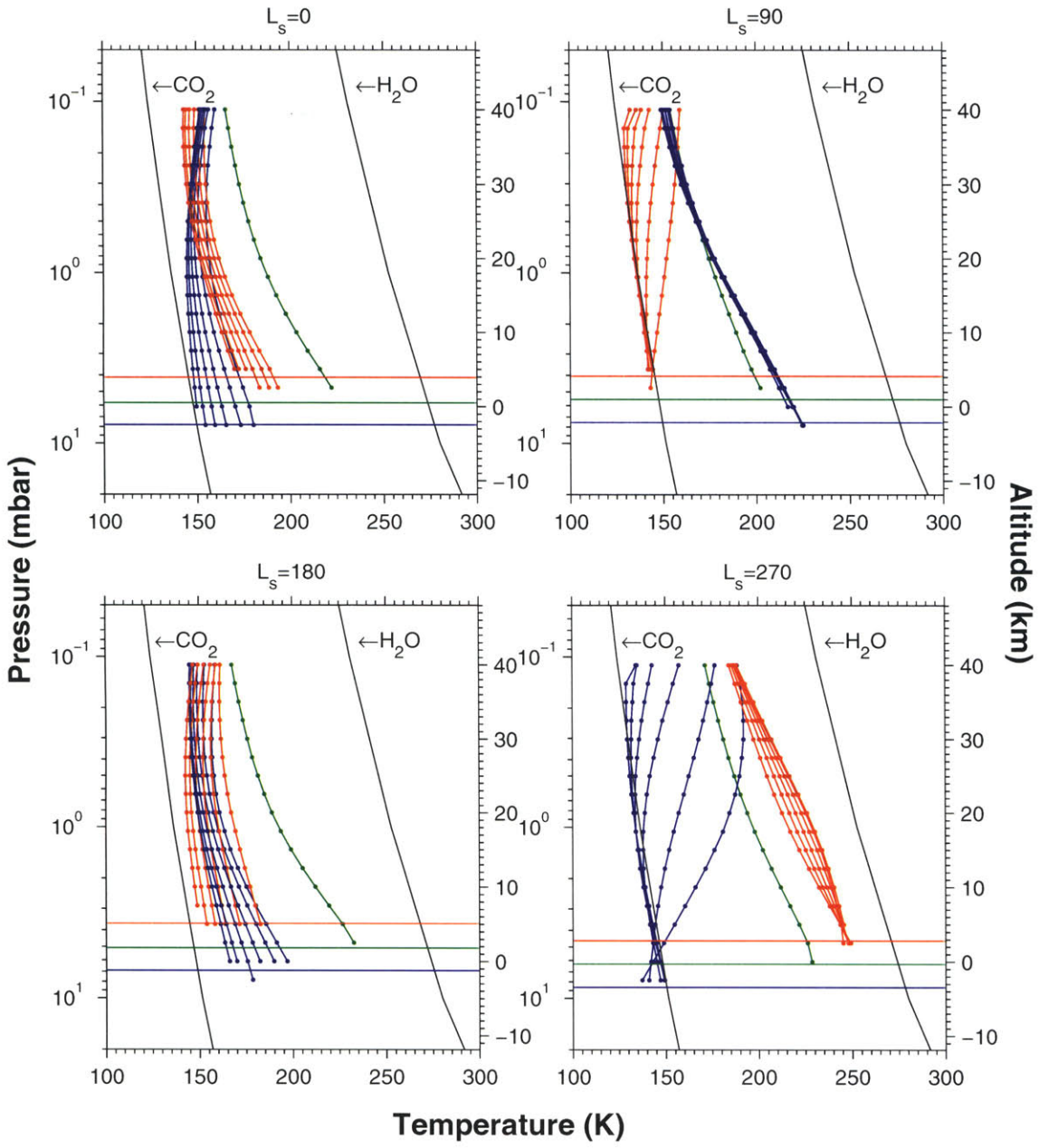

Figure 6-9: Atmospheric pressure and temperatures as measured by TES. The curves show equatorial (green), northern hemisphere (blue) and southern hemisphere (red) conditions, the latter two in 5 degree latitude increments from 60-85° . The horizontal lines are the represent the surface conditions, and the solid black curves indicate the CO_2 and H_2O vapor pressure curves.

observations of the timing of the annual disappearance of CO_2 frost from the surface at the high latitudes, as well as with predictions from global circulation models. At lower latitudes, frost sublimation predates the fitted minima.

It is worth noting that while certainly unexpected from models and simple intuition, the observations of the "off season" component of the accumulation are statistically no different in quality from the annual component. The amplitude is only smaller by a factor of two, and the phase has a similar robustness and correlation with surface features.

These results provide constraints that should be incorporated in future models of the Martian climate system and volatile cycles. In addition, the geographic correlations of the amplitude and phase of the signal with surface features, supports both the interpretation of the data as depositional in origin, and the utility of crossovers for analyses of subtle temporal changes of planetary elevation.

Acknowledgments

We acknowledge essential contributions from Greg Neumann, Dave Smith, and Maria Zuber to this analysis. This work is being prepared for publication in collaboration with these co-authors.

Bibliography

Abshire, J. B., X. Sun, and R. S. Afzal, Mars Orbiter Laser Altimeter: Receiver model and performance analysis, *Appl. Opt.*, *39*, 2440–2460, 2000.

Aharonson, O., M. T. Zuber, G. A. Neumann, D. E. Smith, and J. W. Head, Mars: Northern hemisphere slopes and slope distributions, *Geophys. Res. Lett.*, *25*, 4413–4416, 1998.

Aharonson, O., M. T. Zuber, G. A. Neumann, D. E. Smith, and J. W. Head, Second order statistics of topography of the northern hemisphere of Mars from MOLA, *Lunar and Planet. Sci. Conf.*, *XXX*, 1999.

Aharonson, O., M. T. Zuber, and D. H. Rothman, Statistics of Mars' topography from MOLA: Slopes, correlations and physical models, *J. Geophys. Res.*, *106*, 23,723–23,735, 2001.

Aharonson, O., M. T. Zuber, D. H. Rothman, N. Schorghofer, and K. X. Whipple, Drainage basins and channel incision on Mars, *Proc. Nat. Acad. Sci.*, *99*, 1780–1783, 2002.

Albee, A. L., F. D. Palluconi, and R. E. Arvidson, Mars Global Surveyor Mission: Overview and status, *Science*, *279*, 1671–1672, 1998.

Albee, A. L., R. E. Arvidson, F. Palluconi, and T. Thorpe, Overview of the Mars Global Surveyor mission, *J. Geophys. Res.*, *106*, 23,291–23,316, 2001.

Bachman, D. A. P. J. E., and K. D. Keegan, Thermal and albedo mapping of the polar

regions of Mars using Vikingthermal mapper observations 1. North polar region, *J. Geophys. Res.*, *99*, 25–959–25,991, 1992.

Baker, V. R., *The Channels of Mars*, University of Texas Press, Austin, 1982.

Baker, V. R., Water and the martian landscape, *Nature*, *412*, 228–236, 2001.

Baker, V. R., R. G. Strom, V. C. Gulick, J. S. Kargel, G. Komatsu, and V. S. Kale, Ancient oceans, ice sheets, and the hydrological cycle on Mars, *Nature*, *352*, 589–594, 1991.

Banerdt, W. B., and A. Vidal, Surface drainage on Mars, *Lunar Planet. Sci.*, *XXXII*, #1488, 2001.

Barabási, A.-L., and H. E. Stanley, *Fractal Concepts in Surface Growth*, Cambridge University Press, Cambridge, 1995.

Briggs, G., K. Klaasen, T. Thorpe, J. Wellman, and W. Baum, Martian dynamical phenomena during June-November 1976 - Viking orbiter imaging results, *J. Geophys. Res.*, *82*, 4121–4149, 1977.

Cabrol, N. A., E. A. Grin, and L. R, Ma'adim Vallis evolution: Geometry and models of discharge rate, *Icarus*, *132*, 362–377, 1998.

Carr, M. H., *The Surface of Mars*, Yale University Press, New Haven, 1981.

Carr, M. H., The martian drainage system and the origin of valley networks and fretted channels, *J. Geophys. Res.*, *100*, 7479–7507, 1995.

Carr, M. H., *Water on Mars*, p. 229, Oxford University Press, New York, 1996.

Carr, M. H., and F. C. Chuang, Martian drainage densities, *J. Geophys. Res.*, *102*, 9145–9152, 1997.

Carr, M. H., and G. D. Clow, Martian channels and valleys: Their characteristics, distribution and age, *Icarus*, *48*, 91–117, 1981.

Christensen, P. R., Regional dust deposits on Mars: Physical properties, age, and history, *J. Geophys. Res.*, *91*, 3,533–3,545, 1986.

Christensen, P. R., and H. J. Moore, The Martian surface layer, in *Mars*, edited by H. H. Kieffer, B. M. Jakosky, C. W. Snyder, and M. S. Matthews, pp. 686–729, Univ. of Arizona Press, Tucson, 1992.

Christensen, P. R., R. V. Morris, M. D. Lane, J. L. Bandfield, and M. C. Malin, Global mapping of Martian hematite mineral deposits: Remnants of water-driven processes on early Mars, *J. Geophys. Res.*, *106*, 23,873–23,885, 2001.

Christensen, P. R., et al., Thermal emission spectrometer experiment - Mars Observer mission, *J. Geophys. Res.*, *97*, 7719–7734, 1992.

Christensen, P. R., et al., Detection of crystalline hematite mineralization on Mars by the Thermal Emission Spectrometer: Evidence for near-surface water, *J. Geophys. Res.*, *105*, 9623–9642, 2000.

Clifford, S. M., A model for the hydrologic and climatic behavior of water on Mars, *J. Geophys. Res.*, *98*, 10,973–11,016, 1993.

Costard, F., F. Forget, N. Mangold, and J. P. Peulvast, Formation of recent martian debris flows by melting of near-surface ground ice at high obliquity, *Science*, *295*, 110–113, 2002.

Craddock, R. A., and A. D. Howard, The case for rainfall on a warm, wet early Mars, *J. Geophys. Res.*, submitted, 2002.

Dash, J. G., H. Fu, and J. S. Wettlaufer, The premelting of ice and its environmental consquences, *Rep. Prog. Phys.*, *58*, 115–167, 1995.

Dodds, P. S., and D. H. Rothman, Scaling, universality, and geomorphology, *Annu. Rev. Earth Planet. Sci.*, *28*, 571–610, 2000.

Edwards, S. F., and D. R. Wilkinson, The surface statistics of a granular aggregate, *Proc. R. Soc. London A*, *381*, 17–31, 1982.

Esposito, P. B., W. B. Banerdt, G. F. Lindal, W. L. Sjogren, M. A. Slade, B. G. Bills, D. E. Smith, and G. Balmino, Gravity and topography, in *Mars*, edited by H. H. Kieffer, B. M. Jakosky, C. W. Snyder, and M. S. Matthews, pp. 209–248, Univ. of Arizona Press, Tucson, 1992.

Farmer, C. B., and P. E. Doms, Global and seasonal variation of water vapor on Mars and the implications for permafrost, *J. Geophys. Res.*, *84*, 2881–2888, 1979.

Farmer, C. B., D. W. Davies, A. L. Holland, D. D. Laporte, and P. E. Doms, Mars - Water vapor observations from the Viking orbiters, *J. Geophys. Res.*, *82*, 4225–4248, 1977.

Ferguson, H. M., and B. K. Lucchitta, Dark streaks on talus slopes, Mars, in *Planetary Geology and Geophysics Program Report*, pp. 188–190, 1984.

Flint, J. J., Stream gradient as a function of order, magnitude, and discharge, *Wat. Resour. Res.*, *10*, 969–973, 1974.

Ford, P. G., and G. H. Pettengill, Venus topography and kilometer-scale slopes, *J. Geophys. Res.*, *97*, 13,103–13,114, 1992.

Fox, C. G., and D. E. Hayes, Quantitative methods for analyzing the roughness of the seafloor, *Rev. Geophys.*, *23*, 1–48, 1985.

Frey, H., S. E. Sakimoto, and J. H. Roark, The MOLA topographic signature of the crustal dichotomy boundary zone on Mars, *Geophys. Res. Lett.*, *25*, 4409–4412, 1998.

Frey, H., L. Hutchinson, S. E. H. Sakimoto, and J. H. Roark, A large population of possible buried impact basins on Mars revealed by MOLA topographic data, *Lunar Planet. Sci. Conf.*, *XXXI*, 2000.

Gardiner, C. W., *Handbook of Stochastic Methods for Physics, Chemistry and the Natural Sciences*, 2nd ed., Springer-Verlag, New York, 1985.

Gardner, C. S., Ranging performance of satellite laser altimeters, *IEEE Trans. Geosci. Rem. Sens.*, *30*, 1061–1072, 1992.

Garvin, J. B., and J. J. Frawley, Global vertical roughness of Mars from Mars Orbiter Laser Altimeter pulse-width measurements, in *Lunar Planet. Sci. Conf., XXXI*, 2000.

Garvin, J. B., J. L. Bufton, J. B. Blair, S. B. Luthcke, J. J. Frawley, and J. A. Marshall, Observations of the Earth's topography from the Shuttle Laser Altimeter (SLA): Laser pulse echo recovery measurements of terrestrial surfaces, in *Proc. European Geophys. Soc. Mtg.*, Vienna, 1997.

Garvin, J. B., J. J. Frawley, and J. B. Abshire, Vertical roughness of Mars from the Mars Orbiter Laser Altimeter, *Geophys. Res. Lett.*, *26*, 381–384, 1999.

Garvin, J. B., J. J. Frawley, S. E. H. Sakimoto, and C. Schnetzler, Global Geometric Properties of Martian Impact Craters: An Assessment from Mars Orbiter Laser Altimeter (MOLA) Digital Elevation Models, in *Lunar and Planetary Institute Conference*, vol. 31, p. 1619, 2000.

Gesch, D. B., and K. S. Larson, Techniques for development of global 1-kilometer digital elevation models, in *Pecora Thirteen, Human Interactions with the Environment - Perspectives from Space*, Sioux Falls, South Dakota, August 20-22, 1996.

Goff, J. A., and T. H. Jordan, Stochastic modeling of seafloor morphology: Inversion of sea beam data for second-order statistics, *J. Geophys. Res.*, *16*, 13,589–13,608, 1988.

Goldspiel, J. M., and S. W. Squyres, Groundwater sapping and valley formation on Mars, *Icarus*, *148*, 176–192, 2000.

Goldspiel, J. M., S. W. Squyres, and D. G. Jankowski, Topography of small martian valleys, *Icarus*, *105*, 479–500, 1993.

Golombek, M. P., et al., Overview of the Mars Pathfinder mission and assessment of landing site predictions, *Science*, *278*, 1743–1748, 1997.

Gulick, V. C., Origin of the valley networks on Mars: a hydrological perspective, *Geomorphology*, *37*, 241–268, 2001.

Gulick, V. C., and V. R. Baker, Origin and evolution of valleys on martian volcanoes, *J. Geophys. Res.*, *95*, 14,325–14,344, 1990.

Haar, L., J. Gallagher, and G. Kell, *NBS/NRC Steam Tables*, Hemisphere Publishing Corp., New York, 1984.

Haberle, R. M., and B. M. Jakosky, Atmospheric effects on the remote determination of thermal inertia on Mars, *Icarus*, *90*, 187–204, 1991.

Haberle, R. M., J. B. Pollack, J. R. Barnes, R. W. Zurek, C. B. Leovy, J. R. M. nd H. Lee, and J. Schaeffer, Mars atmosphere dynamics as simulated by the NASA Ames General Circulation Model 1. The zonal mean circulation, *J. Geophys. Res.*, *98*, 3093–3123, 1993.

Haberle, R. M., C. P. McKay, J. Schaeffer, N. A. Cabrol, E. A. Grin, A. P. Zent, and R. Quinn, On the possibility of liquid water on present-day Mars, *J. Geophys. Res.*, *106*, 23,317–23,331, 2001.

Harmon, J. K., A radar study of the Chryse region, Mars, *J. Geophys. Res.*, *102*, 4081–4095, 1997.

Harmon, J. K., R. E. Arvidson, E. A. Guinness, B. A. Campbell, and M. A. Slade, Mars mapping with delay-Doppler radar, *J. Geophys. Res.*, *104*, 14,065–14,090, 1999.

Head, J. W., M. Kreslavsky, H. Hiesinger, M. Ivanov, S. Pratt, N. Seibert, D. E. Smith, and M. T. Zuber, Oceans in the past history of Mars: Tests for their presence using Mars Orbiter Laser Altimeter (MOLA) data, *Geophys. Res. Lett.*, *25*, 4401–4404, 1998.

Head, J. W., H. Hiesinger, M. A. Ivanov, M. A. Kreslavsky, S. Pratt, and B. J. Thomson, Possible oceans on Mars: Evidence from Mars Orbiter Laser Altimeter data, *Science*, *286*, 2134–2137, 1999.

Hecht, M. H., Metastability of Liquid Water on Mars, in *Lunar and Planetary Science Conference*, vol. 32, p. 1364, 2001.

Hess, S. L., R. M. Henry, and J. E. Tillman, The seasonal variation of atmospheric pressure on Mars as affected by the south polar cap, *J. Geophys. Res.*, *84*, 2923–2927, 1979.

Hess, S. L., J. A. Ryan, J. E. tillman, R. M. Henry, and C. B. Leovy, The annual cycle of pressure on Mars measured by Viking landers 1 and 2, *Geophys. Res. Lett.*, *7*, 197–200, 1980.

Howard, A. D., A detachment-limited model of drainage basin evolution, *Wat. Resour. Res.*, *30*, 2261–2285, 1994.

Howard, A. D., and C. Kerby, Channel changes in badlands, *Geol. Soc. Am. Bull.*, *94*, 739–752, 1983.

Howard, A. D., and C. F. McLane, Erosion of cohesionless sediment by groundwater seepage, *Water Resour. Res.*, *24*, 1659–1674, 1988.

Howard, A. D., W. E. Dietrich, and M. A. Seidl, Modeling fluvial erosion on regional to continental scales, *J. Geophys. Res.*, *99*, 13,971–13,986, 1994.

Ingersoll, A. P., Mars: Occurrence of liquid water, *Science*, *168*, 972–973, 1970.

Jakosky, B. M., The seasonal cycle of water on Mars, *Space Sci. Rev.*, *41*, 131–200, 1985.

Jakosky, B. M., and P. R. Christensen, Global duricrust on Mars: Analysis of remote-sensing data, *J. Geophys. Res.*, *91*, 3547, 1986.

Jakosky, B. M., and C. B. Farmer, The seasonal and global behavior of water vapor in the Mars atmosphere - Complete global results of the Viking atmospheric water detector experiment, *J. Geophys. Res.*, *87*, 2999–3019, 1982.

Jakosky, B. M., and R. M. Haberle, Year-to-year instability of the Mars south polar cap, *J. Geophys. Res.*, *95*, 1359–1365, 1990.

Jakosky, B. M., and R. M. Haberle, The seasonal behavior of water on Mars, in *Mars*, edited by H. H. Kieffer, B. M. Jakosky, C. W. Snyder, and M. S. Matthews, pp. 969–1016, Univ. of Arizona Press, Tucson, 1992.

Jakosky, B. M., and D. O. Muhlemann, A comparison of the thermal and radar characteristics of Mars, *Icarus*, *45*, 25–38, 1981.

James, P. B., Recession of Martian north polar cap - 1977-1978 Viking observations, *J. Geophys. Res.*, *84*, 8332–8334, 1979.

James, P. B., H. H. Kieffer, and D. A. Paige, The seasonal cycle of carbon dioxide on Mars, in *Mars*, edited by H. H. Kieffer, B. M. Jakosky, C. W. Snyder, and M. S. Matthews, pp. 934–968, Univ. of Arizona Press, Tucson, 1992.

Jones, K. L., R. E. Arvidson, E. A. Guinness, S. L. Bragg, S. D. Wall, C. E. Carlston, and D. G. Pidek, One Mars year - Viking lander imaging observations, *Science*, *204*, 799–806, 1979.

Joshi, M. M., B. N. Lawrence, and S. R. Lewis, The effect of spatial variations in unresolved topography on gravity wave drag in the Martian atmosphere, *Geophys. Res. Lett.*, *23*, 2927–2930, 1996.

Kargel, J., and R. Strom, Ancient glaciation on Mars, *Geology*, *20*, 3–7, 1992.

Kieffer, H. H., Mars south polar spring and summer temperatures - A residual CO_2 frost, *J. Geophys. Res.*, *84*, 8263–8288, 1979.

Kieffer, H. H., T. Z. Martin, S. C. Chase, E. D. Miner, and F. D. Palluconi, Martian north pole summer temperatures - Dirty water ice, *Science*, *194*, 1341–1344, 1976.

Kieffer, H. H., T. N. Titus, K. F. Mullins, and P. R. Christensen, Mars south polar spring and summer behavior observed by TES: Seasonal cap evolution controlled by frost grain size, *J. Geophys. Res.*, *105*, 9653–9699, 2000.

Kirk, R. L., E. Howington-Kraus, and B. A. Archinal, High resolution digital elevation models of Mars from MOC narrow angle stereoimages, *International Society for Photogrammetry and Remote Sensing, Extraterrestrial Mapping Workshop*, 2001.

Kirk, R. L., et al., Digital photogrammetric analysis of the IMP camera images: Mapping the Mars Pathfinder landing site in three dimensions, *J. Geophys. Res.*, *104*, 8869, 1999.

Kochel, R. C., and J. F. Piper, Morphology of large valleys on Hawaii: Evidence for groundwater sapping and comparisons with Martian valleys, *J. Geophys. Res.*, *91*, E175–E192, 1986.

Kreslavsky, M. A., and J. W. Head, Kilometer-scale slopes on Mars and their correlation with geologic units: Initial results from Mars Orbiter Laser Altimeter (MOLA) data, *J. Geophys. Res.*, *104*, 21,911–21,924, 1999.

Kreslavsky, M. A., and J. W. Head, Kilometer-scale roughness of Mars: Results from MOLA data analysis, *J. Geophys. Res.*, *105*, 26,695–26,711, 2000.

Laity, J. E., and M. C. Malin, Sapping processes and the development of theater-headed valley networks on the colorado plateau, *Geol. Soc. Am. Bull.*, *96*, 203–217, 1985.

Leighton, R. R., and B. C. Murray, Behavior of carbon dioxide and other volatiles on Mars, *Science*, *153*, 136–144, 1966.

Lemoine, F. G., D. E. Smith, D. D. Rowlands, M. T. Zuber, G. A. Neumann, D. S. Chinn, and D. E. Pavlis, An improved solution of the gravity field of Mars (GMM-2B) from Mars Global Surveyor, *J. Geophys. Res.*, *106*, 23,359–23,376, 2001.

Leovy, C. B., The general circulation of Mars: Models and observations, *Adv. Geophys.*, *28a*, 327–346, 1985.

Lucchitta, B. K., A. S. McEwen, G. D. Clow, P. E. Geissler, R. B. Singer, R. A. Schultz, and S. W. Squyres, The canyon systems of Mars, in *Mars*, edited by H. H. Kieffer, B. M. Jakosky, C. W. Snyder, and M. S. Matthews, pp. 453–492, Univ. of Arizona Press, Tucson, 1992.

Malin, M. C., and M. H. Carr, Groundwater formation of martian valleys, *Nature*, *397*, 589–591, 1999.

Malin, M. C., and K. S. Edgett, Evidence for recent groundwater seepage and surface runoff on Mars, *Science*, *288*, 2330–2335, 2000a.

Malin, M. C., and K. S. Edgett, Sedimentary rocks of early Mars, *Science*, *290*, 1927–1937, 2000b.

Malin, M. C., and K. S. Edgett, Mars Global Surveyor Mars Orbiter Camera: Interplanetary cruise through primary mission, *J. Geophys. Res.*, *106*, 23,429, 2001.

Malin, M. C., et al., Early views of the Martian surface from the Mars Orbiter Camera of Mars Global Surveyor, *Science*, *279*, 1681–1685, 1998.

Martin, L. J., P. B. James, A. Dollfus, K. Iwasaki, and J. D. Beish, Telescopic observations: Visual, photographic, polarimetric, in *Mars*, edited by H. H. Kieffer, B. M. Jakosky, C. W. Snyder, and M. S. Matthews, pp. 34–70, Univ. of Ariz. Press, Tucson, 1992.

Masursky, H., An overview of geologic results from Mariner 9, *J. Geophys. Res.*, *78*, 4009–4030, 1973.

Masursky, H., J. V. Boyce, A. L. Dial, G. G. Schabert, and M. E. Strobell, Classification and time of formation of Martian channels based on Viking data, *J. Geophys. Res.*, *82*, 4016–4037, 1977.

McCauley, J. F., M. H. Carr, J. A. Cutts, W. K. Hartmann, H. Masursky, D. J. Milton, R. P. Sharp, and D. E. Wilhelms, Preliminary Mariner 9 report on the geology of Mars, *Icarus*, *17*, 289–327, 1972.

McEwen, A. S., Mobility of large rock avalanches: Evidence from Valles Marineris, Mars, *Geology*, *17*, 1111–1114, 1989.

McGill, G. E., The Utopia Basin revisited: Regional slope and shorelines from MOLA profiles, *Geophys. Res. Lett.*, *28*, 411, 2001.

McGill, G. E., and A. M. Dimitriou, Origin of the Martian global dichotomy by crustal thinning in the late Noachian or early Hesperian, *J. Geophys. Res.*, *95*, 12,595–12,605, 1990.

Mellon, M. T., B. M. Jakosky, H. H. Kieffer, and P. R. Christensen, High-Resolution Thermal Inertia Mapping from the Mars Global Surveyor Thermal Emission Spectrometer, *Icarus*, *148*, 437–455, 2000.

Morris, E., Aureole deposits of the Martian volcano Olympus Mons, *J. Geophys. Res.*, *87*, 1164, 1982.

Mouginis-Mark, P. J., S. H. Zisk, and G. S. Downs, Ancient and modern slopes in the Tharsis region of Mars, *Nature*, *297*, 546–550, 1982.

Mutch, T. A., R. E. Arvidson, J. W. Head, K. L. Jones, and R. S. Saunders, *The Geology of Mars*, Princeton University Press, Princeton, 1976.

Nattermann, T., and L.-H. Tang, Kinetic surface roughening: I. the kardar-parisi-zhang equation in the weak coupling regime, *Phys. Rev. A*, *45*, 7156–7161, 1992.

Neumann, G. A., and D. W. Forsyth, High resolution statistical estimation of seafloor morphology: Oblique and orthogonal fabric on the Mid-Atlantic ridge, *Marine Geophys. Res.*, *17*, 221–250, 1995.

Neumann, G. A., P. J. Michael, and B. B. Hanan, Temporal variation of crustal emplacement, 33° s Mid-Atlantic ridge, *J. Conf. Abs.*, *1*, 836–837, 1996.

Neumann, G. A., D. D. Rowlands, F. G. Lemoine, D. E. Smith, and M. T. Zuber, Crossover analysis of Mars Orbiter Laser Altimeter data, *J. Geophys. Res.*, *106*, 23,753–23,768, 2001.

Neumann, G. A., J. B. Abshire, D. E. Smith, X. Sun, and M. T. Zuber, MOLA 1064nm Radiometry Measurements: Status and Prospects in Extended Mission, in *Lunar and Planetary Institute Conference*, vol. 33, pp. 1889+, 2002.

NGDC, *Data Announcement 88-MGG-02, Digital relief of the Surface of the Earth*, NOAA, National Geophysical Data Center, Boulder, Colorado, 1988.

Nye, J. F., H. H. Wills, W. B. Durham, P. M. Schenk, and J. M. Moore, The instability of a south polar cap on Mars composed of carbon dioxide, *Icarus*, *144*, 449–455, 2000.

Paige, D. A., The thermal stability of near-surface ground ice on Mars, *Nature*, pp. 43–45, 1992.

Paige, D. A., and A. P. Ingersoll, Annual heat balance of Martian polar caps - Viking observations, *Science*, *228*, 1160–1168, 1985.

Paige, D. A., and S. E. Wood, Modeling the martian seasonal CO_2 cycle. 2. Interannual variability, *Icarus*, *99*, 15–27, 1992.

Palermo, E., J. England, and H. Moore, 2001, Mars Society Convention, Palo Alto, California.

Phillips, R. J., et al., Ancient geodynamics and global-scale hydrology on Mars, *Science*, *291*, 2587–2591, 2001.

Pieri, D. C., Martian valleys: Morphology, distribution, age and origin, *Science*, *210*, 895–897, 1980.

Pollack, J. B., R. M. Haberle, and J. Schaeffer, Simulations of the general circulation of the Martian atmosphere 1. Polar processes, *J. Geophys. Res.*, *95*, 1447–1473, 1990.

Press, W. H., S. A. Teukolsky, W. T. Vetterling, and B. P. Flannery, *Numerical recipes in C. The art of scientific computing, 2nd ed.*, Cambridge: University Press, 1992.

Richardson, M. I., and R. J. Wilson, A topographically forced asymmetry in the martian circulation and climate, *Nature*, *416*, 298–301, 2002.

Rodríguez-Iturbe, I., and A. Rinaldo, *Fractal River Basins: Chance and Self-Organization*, Cambridge University Press, Cambridge, 1997.

Rowlands, D. D., D. E. Pavlis, F. G. Lemoine, G. A. Neumann, and S. B. Lutchke, The use of crossover constraint equations derived from laser altimetry in the orbit determination of Mars Global Surveyor, *Geophys. Res. Lett.*, *26*, 1191–1194, 1999.

Sagan, C., O. B. Toon, and P. J. Gierasch, Climate change on Mars, *Science*, *181*, 1045–1049, 1973.

Scheiddeger, A. E., *Theoretical Geomorphology, 3rd edition*, Springer-Verlag, New York, 1991.

Schofield, J. T., J. R. Barnes, D. Crisp, R. M. Haberle, S. Larsen, J. A. Magalhaes, J. R. Murphy, A. Seiff, and G. Wilson, The Mars Pathfinder Atmospheric Structure Investigation/Meteorology, *Science*, *278*, 1752+, 1997.

Schorghofer, N., and D. H. Rothman, Basins of attraction on random topography, *Phys. Rev. E*, *63*, 026,112, 2001.

Scott, D. H., and K. L. Tanaka, Geologic map of the western equatorial region of Mars, Scale 1:15,000,000, *U.S. Geol. Survey Map I-1802-A*, 1986.

Sharp, R. P., and M. C. Malin, Channels on Mars, *Geol. Soc. Am. Bull.*, *86*, 593–609, 1975.

Sharpton, V. L., and J. W. Head, Analysis of regional slope characteristics on Venus and Earth, *J. Geophys. Res.*, *90*, 3733–3740, 1985.

Sharpton, V. L., and J. W. Head, A comparison of the regional slope characteristics of Venus and Earth: Implications for geologic processes on Venus, *J. Geophys. Res.*, *91*, 7545–7554, 1986.

Smith, D. E., and M. T. Zuber, The shape of Mars and the topographic signature of the hemispheric dichotomy, *Science*, *271*, 184–188, 1996.

Smith, D. E., and M. T. Zuber, The relationship between MOLA northern hemisphere topography and the 6.1-mbar atmospheric pressure surface of Mars, *Geophys. Res. Lett.*, *25*, 4297–4400, 1998.

Smith, D. E., M. T. Zuber, G. A. Neumann, and F. G. Lemoine, Topography of the Moon from the Clementine lidar, *J. Geophys. Res.*, *102*, 1591–1611, 1997.

Smith, D. E., F. G. L. Lemoine, M. T. Zuber, and P. R. Tracadas, Gravity field analysis and orbit determination from the Mars Global Surveyor Radio Science experiment, in *Lunar and Planetary Science Conference*, vol. 29, pp. 1837–1838, 1998a.

Smith, D. E., M. T. Zuber, R. M. Haberle, D. D. Rowlands, and J. R. Murphy, The Mars seasonal CO_2 cycle and the time variation of the gravity field: A General Circulation Model simulation, *J. Geophys. Res.*, *104*, 1885–1896, 1999a.

Smith, D. E., M. T. Zuber, and G. A. Neumann, Seasonal variation of snow depth on Mars, *Science*, *294*, 2141–2146, 2001a.

Smith, D. E., et al., Topography of the northern hemisphere of Mars from the Mars Orbiter Laser Altimeter (MOLA), *Science*, *279*, 1686–1692, 1998b.

Smith, D. E., et al., The global topography of Mars and implications for surface evolution, *Science*, *284*, 1495–1503, 1999b.

Smith, D. E., et al., Mars Orbiter Laser Altimeter: Experiment summary after the first year of global mapping of Mars, *J. Geophys. Res.*, *106*, 23,689–23,722, 2001b.

Smith, D. K., and T. H. Jordan, Seamount statistics in the Pacific-ocean, *J. Geophys. Res.*, *93*, 2899–2918, 1988.

Smith, P. H., et al., Results from the Mars Pathfinder Camera, *Science*, *278*, 1758+, 1997.

Squyres, S. W., The history of water on Mars, *Ann. Rev. Earth Planet. Sci.*, *12*, 83–106, 1984.

Squyres, S. W., and M. H. Carr, Geomorphic evidence for the distribution of ground ice on Mars, *Science*, *231*, 249–252, 1986.

Sullivan, R., P. Thomas, J. Veverka, M. Malin, and K. S. Edgett, Mass movement slope streaks imaged by the Mars Orbiter Camera, *J. Geophys. Res.*, *106*, 23,607, 2001.

Tanaka, K., and G. Leonard, Geology and landscape evolution of the Hellas region of Mars, *J. Geophys. Res.*, *100*, 5407–5432, 1995.

Tanaka, K. L., and D. H. Scott, Geologic map of the polar regions of Mars, u.s. geological survey miscellaneous investigations map i-1802c, 1987.

Tarboton, D. G., A new method for the determination of flow directions and upslope areas in grid digital elevation models, *Water Resour. Res.*, *33*, 309–319, 1997.

Tarboton, D. G., R. L. Bras, and I. Rodríguez-Iturbe, Scaling and elevation in river networks, *Water Resour. Res.*, *25*, 2037–2051, 1989.

Thomas, P., S. Squyres, K. Herkenhoff, A. Howard, and B. Murray, Polar deposits of Mars, in *Mars*, edited by H. H. Kieffer, B. M. Jakosky, C. W. Snyder, and M. S. Matthews, pp. 767–795, Univ. of Arizona Press, Tucson, 1992.

Titus, T. N., H. H. Kieffer, K. F. Mullins, and P. R. Christensen, Tes premapping data: Slab ice and snow flurries in the Martian north polar night, *J. Geophys. Res.*, *106*, 23,181, 2001.

Toigo, A. D., and M. I. Richardson, A mesoscale model for the Martian atmosphere, *J. Geophys. Res.*, in press.

TRCVP, *Vapor Pressure Database, Version 2.2P*, Thermodynamic Research Center, Texas A&M University, College Station, TX.

Turcotte, D. L., *Fractals and Chaos in Geology and Geophysics*, Cambridge Univ. Press, New York, 1997.

Tyler, G. L., G. Balmino, D. P. Hinson, W. L. Sjogren, D. E. Smith, R. A. Simpson, S. W. Asmar, P. Priest, and J. D. Twicken, Radio science observations with Mars Global Surveyor: Orbit insertion through one year in mapping orbit, *J. Geophys. Res.*, *106*, 23,327–23,348, 2001.

Tyler, G. L., et al., Radio science investigations with Mars Observer, *J. Geophys. Res.*, *97*, 7759–7779, 1992.

Voss, R. F., Random fractals: characterization and measurement, in *Dynamics of Fractal Surfaces*, edited by F. Family and T. Vicsek, World Scientific, Singapore, 1991.

Wagner, W., A. Saul, and A. J. Pruss, International equations for the pressure along the melting and along the sublimation curve of ordinary water substance, *J. Phys. Chem. Ref. Data*, *23*, 515, 1994.

Weast, R. C. (Ed.), *Handbook of Chemistry and Physics, 61st ed.*, CRC Press, Boca Raton, FL, 1981.

Whipple, K. X., and G. E. Tucker, Dynamics of the stream-power river incision model: Implications for height limits of mountain ranges, landscape response timescales, and research needs, *J. Geophys. Res.*, *104*, 17,661–17,674, 1999.

Whipple, K. X., E. Kirby, and S. H. Brocklehurst, Geopmorphic limits to climate-induced increases in topographic relief, *Nature*, *401*, 39–43, 1999.

Wichman, R. W., and P. H. Schultz, Sequence and mechanisms of deformation around the Hellas and Isidis impact basins on Mars, *J. Geophys. Res.*, *94*, 17,333–17,357, 1989.

Wilhelms, D. E., and S. W. Squyres, The Martian hemispheric dichotomy may be due to a giant impact, *Nature*, *309*, 138–140, 1984.

Willgoose, G., R. L. Bras, and I. Rodriguez-Iturbe, A physical explanation of an observed link area-slope relationship, *Wat. Resour. Res.*, *27*, 1697–1702, 1991.

Williams, R. M. E., and R. J. Phillips, Morphometric measurements of martian valley networks from Mars Orbiter Laser Altimeter (MOLA) data, *J. Geophys. Res.*, *106*, 23,737–23,751, 2001.

Wu, S. S. C., Topographic maps of the polar, western, and eastern regions of Mars, scale 1:15,000,000, *U.S. Geol. Survey Map I-2160*, 1991.

Zimbelman, J. R., and H. H. Kieffer, Thermal mapping of the northern equatorial latitudes of mars, *J. Geophys. Res.*, *84*, 8239, 1979.

Zuber, M. T., The crust and mantle of Mars, *Nature*, *412*, 220 – 227, 2001.

Zuber, M. T., D. E. Smith, S. C. Solomon, D. O. Muhleman, J. W. Head, J. B. Garvin, J. B. Abshire, and J. L. Bufton, The Mars Observer Laser Altimeter investigation, *J. Geophys. Res.*, *97*, 7781–7797, 1992.

Zuber, M. T., L. Lim, and H. J. Zwally, The role of viscous deformation onthe morphology of the Martian north polar cap, in *First Int. Conf. on Mars Polar Science and Exploration*, edited by S. Clifford, D. Fisher, and J. Rice, pp. 45–46, Lunar Planet. Inst., Houston, 1998a.

Zuber, M. T., D. E. Smith, R. J. Phillips, S. C. Solomon, W. B. Banerdt, G. A. Neumann, and O. Aharonson, Shape of the northern hemisphere of Mars from the Mars Orbiter Laser Altimeter (MOLA), *Geophys. Res. Lett.*, *25*, 4393–4396, 1998b.

Zuber, M. T., et al., Observations of the north polar region of Mars from the Mars Orbiter Laser Altimeter, *Science*, *282*, 2053–2060, 1998c.

Zuber, M. T., et al., Internal structure and early thermal evolution of Mars from Mars Global Surveyor topography and gravity, *Science*, *287*, 1788–1793, 2000.

Zurek, R. W., J. R. Barnes, R. M. Haberle, J. B. Pollack, J. E. Tillman, and C. B. Leovy, Dynamics of the atmosphere of Mars, in *Mars*, edited by H. H. Kieffer, B. M. Jakosky, C. W. Snyder, and M. S. Matthews, pp. 835–933, Univ. of Arizona Press, Tucson, 1992.

Zwally, H. J., A. Fountain, J. Kargel, L. Kouvaris, K. Lewis, D. MacAyeal, T. Pfeffer, and J. L. Saba, Morophology of Mars North Polar Cap, in *Second Int. Conf. on Mars Polar Science and Exploration*, edited by S. Clifford, D. Fisher, and J. Rice, Lunar Planet. Inst., Houston, 2000.